



POLITECNICO
MILANO 1863



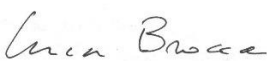
Anthropogenic Water Use (CCI-AWU)

Deliverable 4: Product Validation and Algorithm Assessment Report (PVASR)

Date	Issue	Section	Page	Comment
09/12/2024	1.0			

Control Document

Process	Name	Date
Written by:	Luca Brocca, Christian Massari, Sara Modanesi, Jacopo Dari, Carla Saltalippi, Renato Morbideli, Gabrielle De Lannoy, Michel Bechtold, Louise Busschaert, Zdenko Heyvaert, Wouter Dorigo, Pierre Laulet, Pia Langhans, Maria Cristina Rulli, Davide Danilo Chiarelli, Nikolas Galli	
Checked by	Luca Brocca	09/12/2024

	Signature	Date
For CCI AWU team		09/12/2024
For ESA		

[This page is left intentionally blank]

List of content

1.	Introduction.....	6
1.1.	The CCI-AWU project.....	6
1.2.	Scope of this report	6
1.3.	Applicable Documents.....	6
2.	Validation of the SM-based inversion approach	8
2.1.	Murray-Darling basin (Australia)	8
2.2.	Contiguous United States (CONUS)	16
2.3.	India	19
2.4.	Ebro basin (Spain).....	23
3.	Validation of the SM-based delta approach.....	27
3.1.	Introduction.....	27
3.2.	CONUS	27
3.3.	Ebro basin	30
3.4.	Murray-Darling basin.....	33
3.5.	India	37
3.6.	Summary and conclusion.....	39
3.7.	Appendix.....	40
4.	Validation of the Flux-based approach.....	41
4.1.	Introduction.....	41
4.2.	IFLUX-BASED analysis across the five selected regions	42
4.2.1.	California Valley	42
4.2.2.	Snake River Plain.....	43
4.2.3.	Great Plains.....	45
4.2.4.	Mississippi floodplain	46
4.2.5.	Rainfed region	48
4.3.	Discussion	49
4.4.	Recommendations and conclusion.....	50
5.	Validation of the model-observation integration approach	52
5.1.	Introduction.....	52
5.2.	Irrigation detection.....	52
5.2.1.	Approach 1: relative bias.....	53

5.2.2.	Approach 2: multiresolution analysis to detect irrigation and comparison with bias approach	
	55	
5.3.	Irrigation quantification.....	58
5.3.1.	Deterministic runs	58
5.3.2.	Ensemble runs	68
References	71

1. Introduction

1.1. The CCI-AWU project

The closure of the Earth's water cycle (as well as the energy balance and the carbon cycles) through satellite Earth Observation (EO) represents one of the outstanding scientific challenges highlighted by the Global Climate Observing System (GCOS). Required standards of accuracy are fixed to 5% and annual timescale. To this end, a suite of essential climate variables (ECVs) has been defined to understand the evolution of climate and to assess the potential derived risks. However, if targets at annual timescale can generally be reached, larger uncertainties are observed for sub-annual and sub-continental time and spatial scales, respectively (Dorigo et al., 2021; Rodell et al., 2015). In this context, the development of an ECV that includes the information on anthropogenic water use (AWU) can help in advancing the proper closure of the water cycle at higher spatial and temporal scales. In the ESA Climate Change Initiative Anthropogenic Water Use (CCI-AWU) precursor project, AWU is more specifically intended as agricultural water allocated for irrigation, which represents the largest anthropogenic water use, thus making irrigation being the most impactful human activity on the hydrological cycle. FAO (2016) estimated that irrigation, worldwide, accounts for more than 70% of water withdrawn from surface (i.e., rivers, lakes) and subsurface (i.e., groundwater) water sources and these estimates are expected to increase in the near future due to an increase in population and in food production, especially over arid and semi-arid regions (McDermid et al., 2023). In this context, the main data source identified by GCOS for tracking AWU is from FAO's AQUASTAT. However, AQUASTAT provides survey-based irrigation estimates which do not meet the GCOS requirements, i.e., data are provided on a 5-years interval instead of yearly and are available every 2-3 years.

The overarching objective of Climate Change Initiative – Anthropogenic Water Use (CCI-AWU) precursor project is to derive long-term (i.e., at least twenty years) AWU time series for selected regions using several approaches exploiting remote sensing observations, as a proof-of-concept of the feasibility towards a proper AWU ECV product.

The CCI-AWU project involves a consortium led by CNR-IRPI and comprises the following organisations:

1. Vienna University of Technology (TU Wien), hereinafter TUWIEN;
2. KULeuven, Department of Earth and Environmental Sciences, Division Soil and Water Management (KATHOLIEKE UNIVERSITEIT LEUVEN), hereinafter KULeuven;
3. University of Perugia (UNIVERSITY OF PERUGIA), hereinafter UNIPG
4. Politecnico di Milano (POLITECNICO DI MILANO), department of Civil and Environmental Engineering, hereinafter POLIMI

1.2. Scope of this report

The Product Validation and Algorithm Selection Report (PVASR) provides a complete report of the results of the algorithm round-robin intercomparison as the basis for further algorithms development during the project. The PVASR is not intended to be a public document.

1.3. Applicable Documents

- Proposal.
- Deliverable D2. Report explaining the criteria for selecting the test regions.

-
- Deliverable D3. Algorithm Theoretical Baseline Document

2. Validation of the SM-based inversion approach

The SM-based inversion approach has been implemented over the four selected study areas to produce irrigation water use (IWU) estimates during different periods depending on the temporal coverage of the specific soil moisture data set used as an input. Figure 2.1 provides an overview of the temporal coverage of the different experiments carried out; it is noteworthy that the first half of the period with available information has been used to calibrate the method parameters, as specified in the Deliverable 3. The retrieved IWU estimates are available since January 2007 for ASCAT, June 2010 for SMOS L2, April 2015 for SMAP L2, and January 2003 for the CCI products; the ending date is December 2022, common to all the data sets. The minimization of the root mean square difference between estimated and observed rainfall has been adopted as optimization strategy; during this step, non-irrigated seasons have been considered in their entirety, while days with rainfall rates lower than 1 mm during the irrigated seasons (i.e., potentially irrigation days) have been masked out. The irrigation estimates have been then produced over the whole period of data availability, but considering irrigation seasons only. To refine the spatial domain, only areas equipped for irrigation have been considered. To do this, the data set provided by Mehta et al. (2022) has been used. Only pixels with percentage of area equipped for irrigation higher than 5% have been considered.

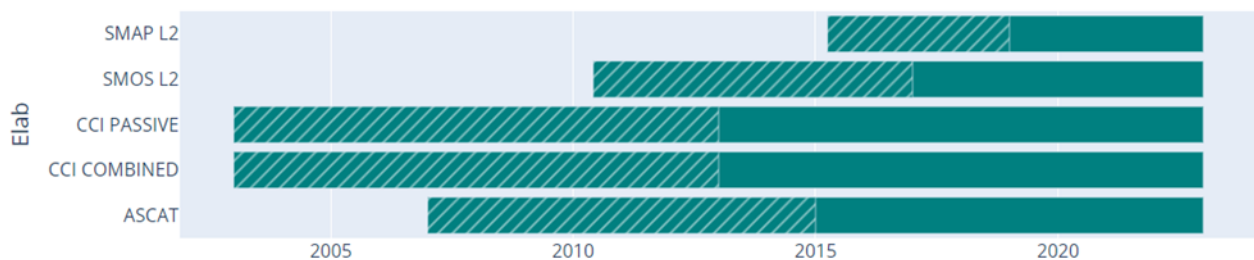


Figure 2.1. Length of irrigation time series available for the different soil moisture products considered. The fielded portion of the bar represents the calibration period.

2.1. Murray-Darling basin (Australia)

An irrigation season spanning from September to April has been considered for the Murray-Darling basin (Portmann et al., 2008; Dari et al., 2023). The average seasonal cumulated IWU amounts estimated through the different input soil moisture data sets are provided in Figure 2.2. Although different in magnitude, IWU patterns retrieved through the various soil moisture products in the Murray-Darling basin generally decrease from North to South.

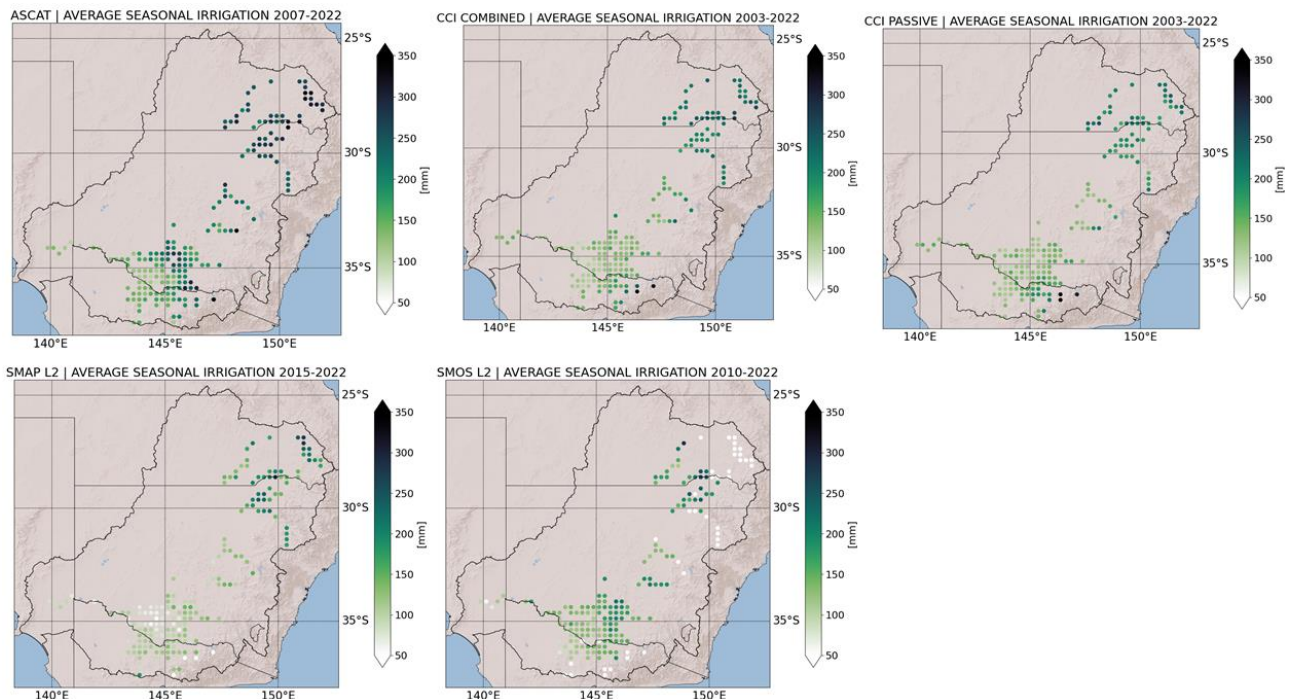


Figure 2.2. Seasonal cumulated IWU amounts in the Murray-Darling basin averaged during the period adopted in each experiment.

The long-term time series of reference irrigation available for the Murray-Darling basin allow for a robust assessment of the retrieved IWU. The comparison in terms of monthly rates is provided in panel a) of Figures 2.3-2.6; benchmark irrigation rates are represented by the light grey shaded area, while retrieved IWU are indicated by the lines in different colours depending on the soil moisture data sets used (red for ASCAT, black for CCI COMBINED, green for CCI PASSIVE, aquamarine for SMAP L2, and light purple for SMOS L2). The same correspondence of colours is adopted for all the analyses based on the SM-based inversion approach presented in this report. Performances in terms of Pearson correlation, r , $RMSE$ and $BIAS$ are reported on top of panels. Since the temporal coverage of SMAP L2 is considerably lower than those of the other products, the metrics calculated during the same time span in which SMAP L2 is available, when applicable, are reported in the tables of panel b) for a fair comparison. Note that the validation has been carried out over all the pilot districts except for Western Murray (see Deliverable 2 for details on the study area), discarded because of its small size (less than 50 km²) with respect to the resolution targeted in the project. Over the Murray-Wakool district (see Figure 2.3) the best results in terms of $RMSE$ and $BIAS$ are obtained with ASCAT soil moisture ($RMSE = 14.51$ mm/month and $BIAS = -0.72$ mm/month). The highest r values are obtained by leveraging ASCAT and SMOS L2 products, but their low entity in absolute terms highlights a difficulty in properly reproducing irrigation timing that is common to all the experiments carried out over the Murray-Darling basin. By looking at results during the shorter time window in which SMAP L2 data is available, the highest r values (equal to 0.50) are found for the CCI soil moisture products, but SMAP L2 overperforms the other data sets in terms of $RMSE$ (equal to 10.14 mm/month) and $BIAS$ (equal to 4.82 mm/month). Figure 2.4 summarises results over Muray-Mulwala district, where ASCAT results as the best performing product according to all the three metrics considered. By looking at the period 2015-2019, SMAP L2 provides the lowest $RMSE$ and $BIAS$, equal to 12.54 mm/month and to 0.14 mm/month, respectively. ASCAT provides the best result in terms of r .

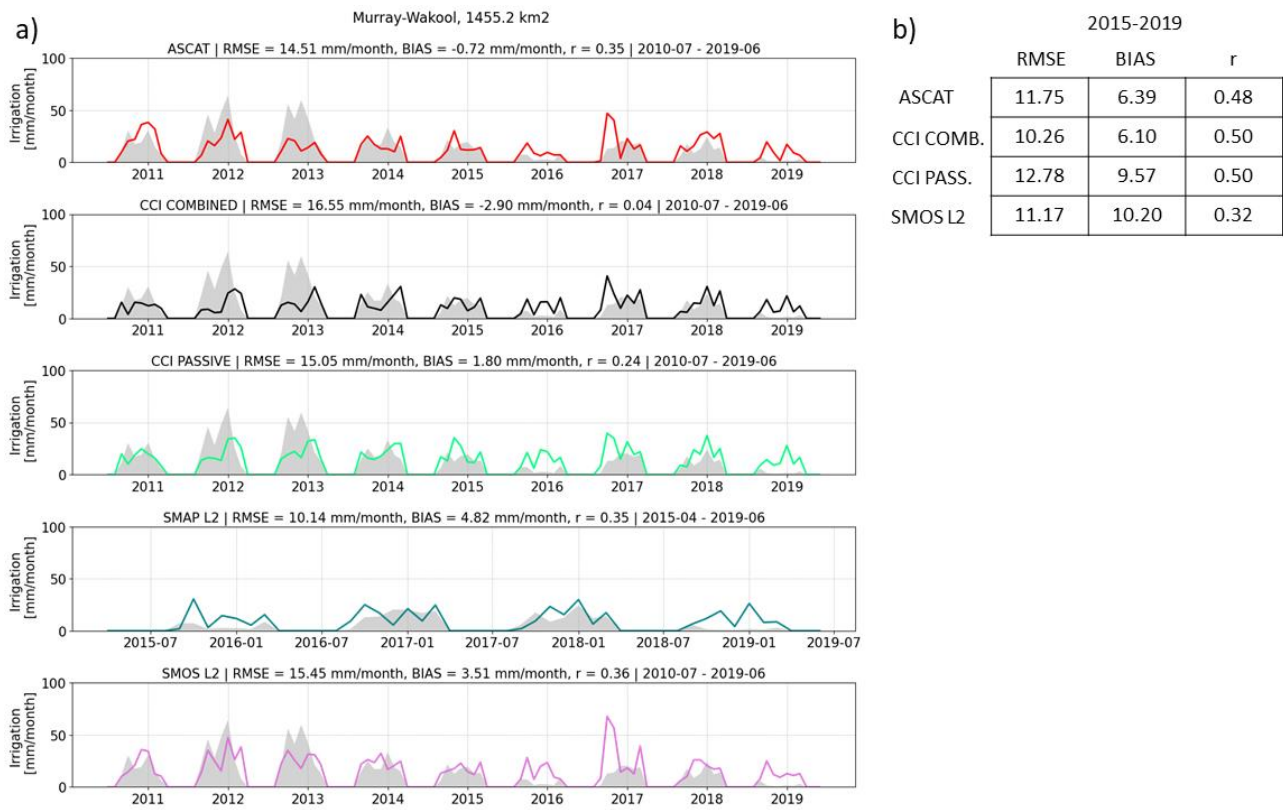


Figure 2.3. Panel a): monthly time series of estimated IWU against reference values over the Murray-Wakool district. *RMSE*, *BIAS*, and Pearson correlation, *r*, values are reported above the panels. Panel b) reports the same metrics but calculated considering the shorter period matching with SMAP L2 availability.

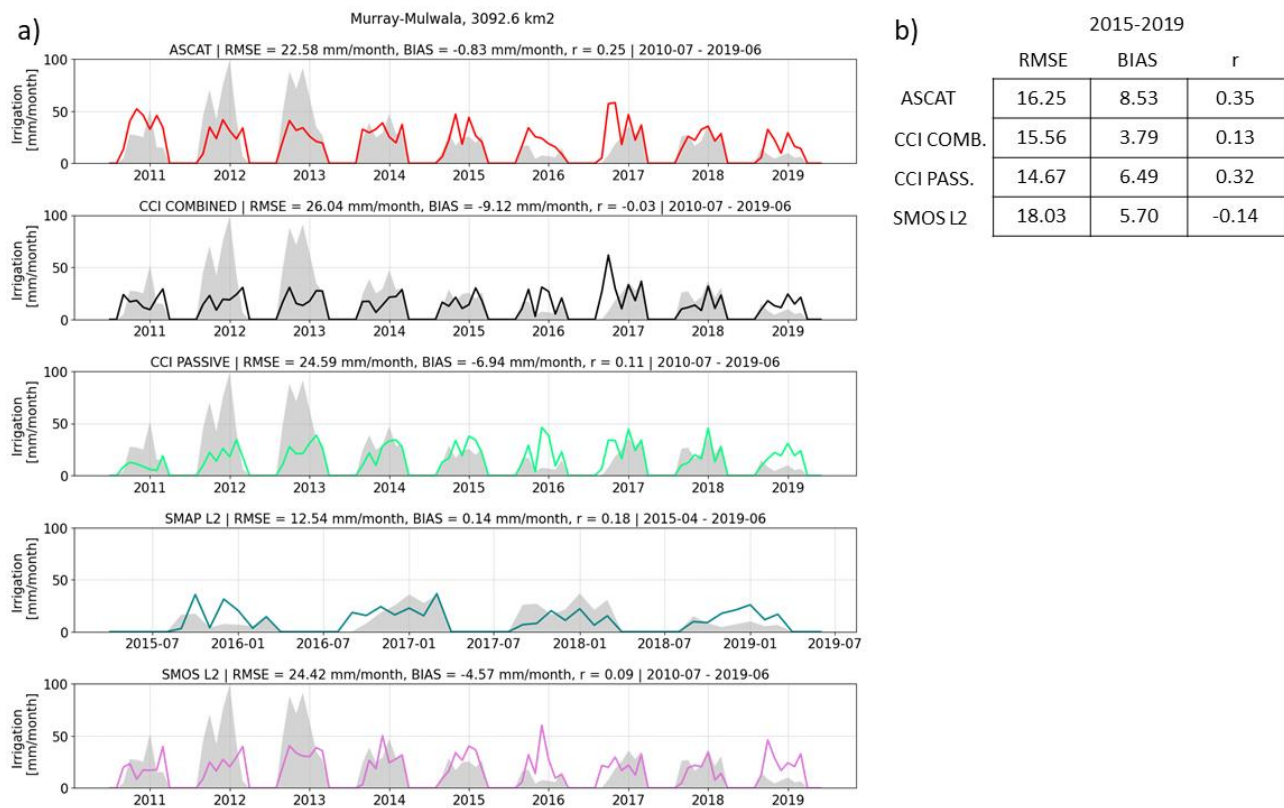


Figure 2.4. Panel a): monthly time series of estimated IWU against reference values over the Murray-Mulwala district. *RMSE*, *BIAS*, and Pearson correlation, *r*, values are reported above the panels. Panel b) reports the same metrics but calculated considering the shorter period matching with SMAP L2 availability.

Coleambally is the district where the highest errors are found. Panel a) of Figure 2.5 shows that SMOS L2 provides the best results in terms of *RMSE*, equal to 35.76 mm/month, and of *r*, equal to 0.17. ASCAT-derived IWU estimates are characterised by the lowest *BIAS* (-7.14 mm/month). It is noteworthy that the validation for the experiments based on ASCAT and on the two CCI soil moisture data sets covers the period 2010-2019, while SMOS L2 time series starts one year after, thus making results not fully comparable. However, considering that only one season is missed in the SMOS L2 experiment, we decided to not consider 2011-2019 as a separate sub-period of this analysis. Referring to the time span 2015-2019, SMAP L2 provides the lowest *RMSE* (24.29 mm/month) and the highest *r* (0.12) values, while the lowest *BIAS*, equal to 0.26 mm/month, is found by leveraging the CCI PASSIVE data set. Finally, Figure 2.6 summarises the outcomes over the Murrumbidgee district. The reference irrigation data is available from 2014 onwards; hence, we have not considered a separated sub-period based on the SMAP L2 availability, as the mismatch is represented by a single water season. The lowest *RMSE* value, equal to 19.70 mm/month, is obtained through SMOS L2 soil moisture, which also provides best results in terms of *BIAS* together with a close value by ASCAT (-8.16 mm/month and -8.64 mm/month, respectively). CCI PASSIVE provides the highest *r* value of 0.44.

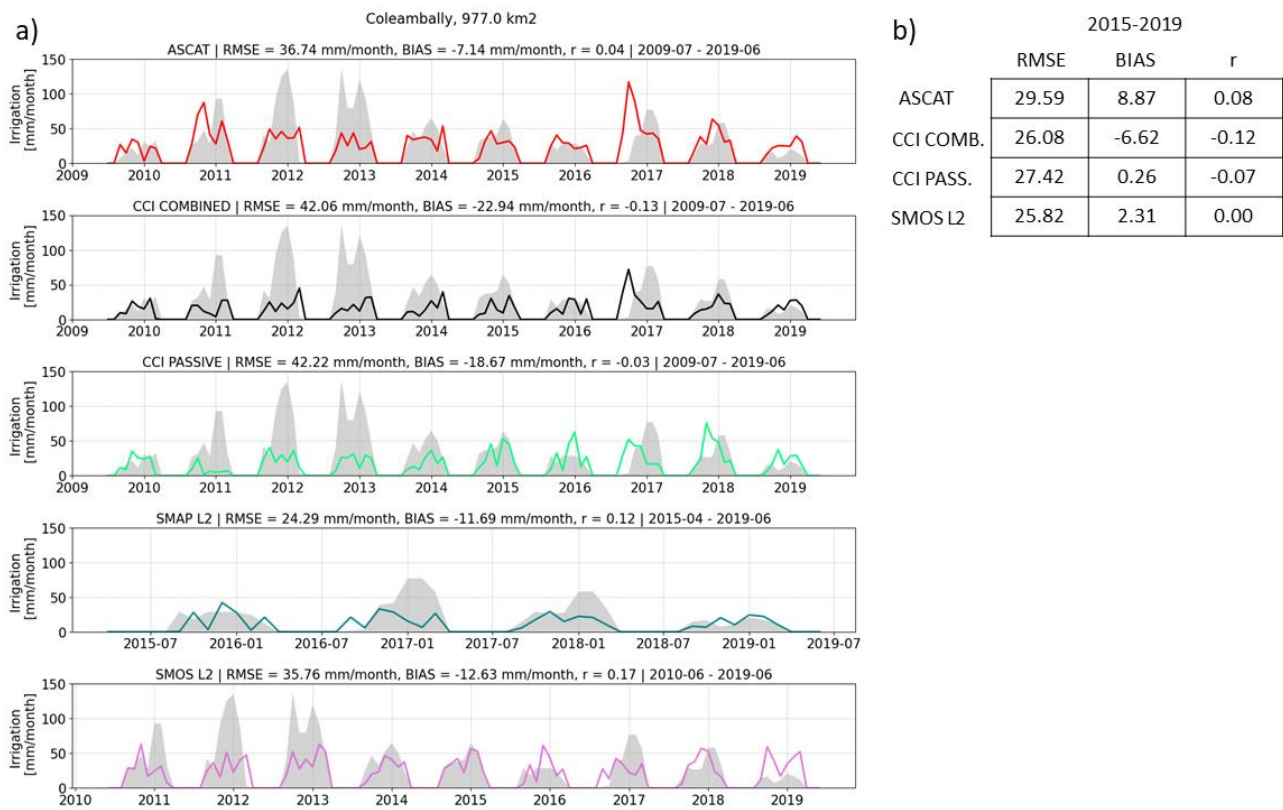


Figure 2.5. Panel a): monthly time series of estimated IWU against reference values over the Coleambally district. *RMSE*, *BIAS*, and Pearson correlation, *r*, values are reported above the panels. Panel b) reports the same metrics but calculated considering the shorter period matching with SMAP L2 availability.

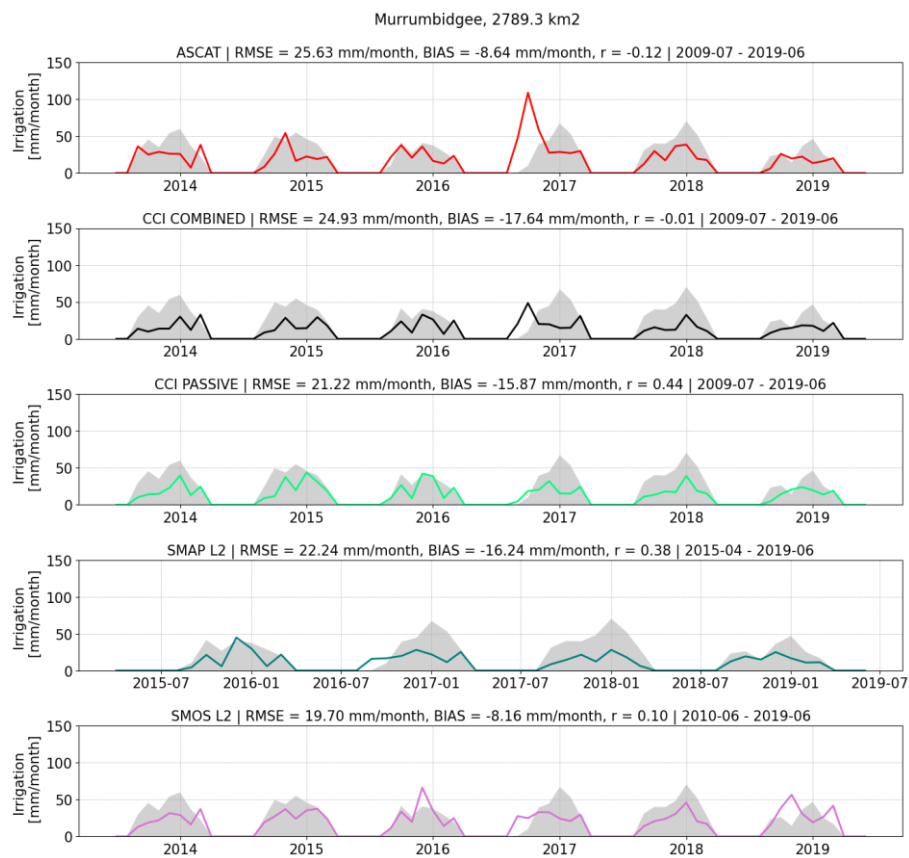


Figure 2.6. Monthly time series of estimated IWU against reference values over the Murrumbidgee district. *RMSE*, *BIAS*, and Pearson correlation, *r*, values are reported above the panels.

In summary, ASCAT provides the most satisfactory performances overall, even though the irrigation timing is not properly reproduced. Low *r* values are actually a common issue to all the experiments carried out. Among the considered soil moisture products, SMOS L2 also provides appreciable performances. It is noteworthy that the evaluation of SMAP L2 performances is limited due to the lower temporal coverage, but during overlapping periods it often outperforms other data sets.

Results obtained within this project have been compared with outcomes from Dari et al. (2023), who produced a regional data set of IWU at 6 km spatial resolution over the Murray-Darling area. Such estimates rely on the SM-based inversion approach forced with CYGNSS (Cyclone Global Navigation Satellite System) soil moisture, ERA5-Land precipitation and GLEAM v3.5b potential evaporation. The comparison summarised in Table 2.1 is carried out considering the common period covering the irrigation seasons of 2017/2018 and 2018/2019. Results obtained in this project are highlighted in green if they outperform the reference ones reported in Dari et al. (2023) or in red in the opposite case. Over the Murray-Wakool district, results obtained in this project outperforms those found with high-resolution data in terms of *RMSE* and *BIAS*. Conversely, *r* remains systematically lower. Over the other pilot districts, despite sporadic exceptions, results of Dari et al. (2023) remain more satisfactory than those obtained in this project through coarse resolution soil moisture data sets. However, a thorough comparison with existing IWU data sets is foreseen in WP530.

Table 2.1. Comparison between results obtained in the CCI-AWU project and in Dari et al. (2023). Results obtained in this project are highlighted in green if they outperform the reference ones reported in Dari et al. (2023) or in red in the opposite case.

	r [-]	RMSE [mm/month]	BIAS [mm/month]
Murray-Wakool			
Dari et al. (2023)	0.84	15.22	13.67
ASCAT	0.65	10.03	7.49
CCI COMB.	0.50	9.29	5.56
CCI PASS.	0.52	11.90	8.97
SMAP L2	0.36	10.32	5.48
SMOS L2	0.32	10.83	7.34
Murray-Mulwala			
Dari et al. (2023)	0.66	8.65	3.18
ASCAT	0.42	11.55	5.29
CCI COMB.	0.26	10.60	-0.95
CCI PASS.	0.25	12.35	3.54
SMAP L2	-0.16	12.83	-2.47
SMOS L2	-0.29	17.43	4.80
Coleambally			
Dari et al. (2023)	0.77	10.54	-3.07
ASCAT	0.50	16.20	7.23
CCI COMB.	0.55	14.11	-5.68
CCI PASS.	0.27	21.01	4.05
SMAP L2	0.38	16.82	-8.78
SMOS L2	0.08	24.25	9.97
Murrumbidgee			
Dari et al. (2023)	0.84	9.64	-7.26
ASCAT	0.57	18.87	-14.44

CCI COMB.	0.57	23.66	-20.17
CCI PASS.	0.62	21.33	-17.83
SMAP L2	0.58	23.35	-19.87
SMOS L2	-0.11	21.33	-6.89

Finally, the capability of the retrieved IWU products in capturing drought events has been assessed. As an example, Figure 2.7 shows the time series of seasonal IWU retrieved leveraging ASCAT soil moisture over the Murray-Wakool and Murray-Mulwala districts in panel a) and the surface water use reported by the 2021 Annual water Take Report (<https://www.mdba.gov.au/sites/default/files/publications/annual-water-take-report-2019-2020.pdf>) produced by the Basin Authority in panel b). It can be observed that there is a correspondence between minimum IWU estimated in 2016, 2019, and 2020 and scarcity of water allocated for irrigation over New South Wales (where the districts are located, indicated by the light blue line) during the same years. Bretreger et al. (2020) also report that the season 2016 was characterised by limited water allocation over the pilot irrigation districts.

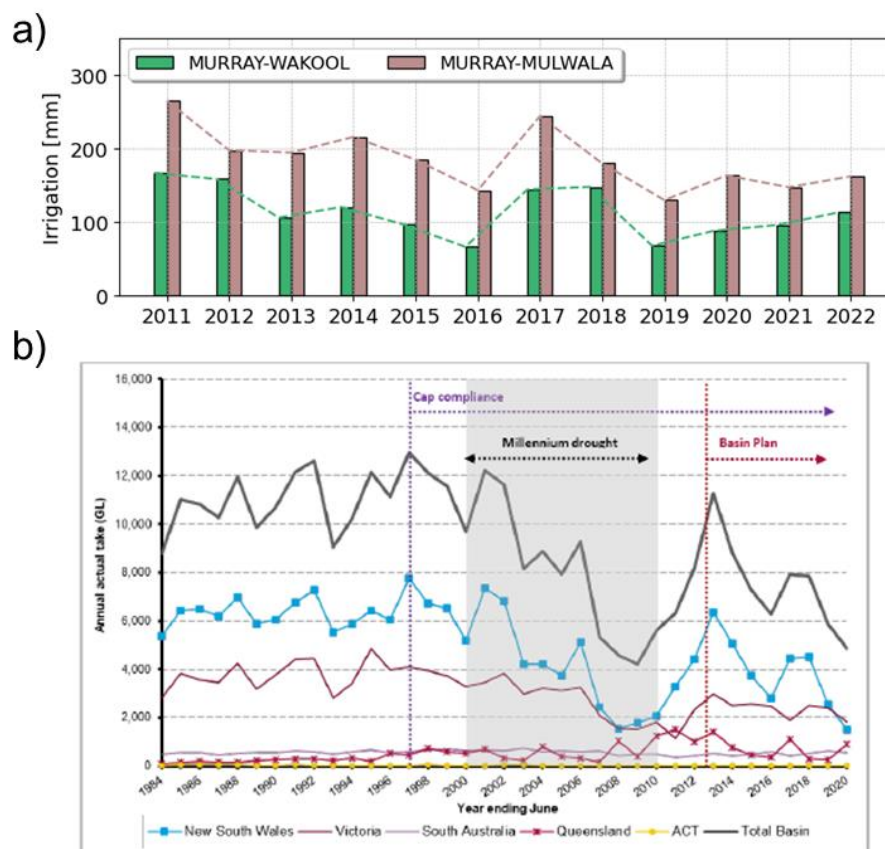


Figure 2.7. Panel a): seasonal IWU estimated in the Murray-Wakool and the Murray-Mulwala districts leveraging ASCAT soil moisture. Panel b): surface water use reported by the 2021 Annual water Take Report produced by the Basin Authority; New South Wales, the state where the considered districts are located, is indicated by the light blue line.

2.2. Contiguous United States (CONUS)

The period ranging from May to September has been considered as the reference season for producing IWU estimates over the CONUS. The average seasonal amounts estimated leveraging the different soil moisture products are shown in Figure 2.8. The ASCAT-based map shows the highest IWU rates over the Nebraska Plains and the Mississippi Floodplain, over which IWU higher than other irrigated areas are found according to the CCI COMBINED and the SMAP L2 products also. More evenly distributed IWU patterns are retrieved leveraging CCI PASSIVE and SMOS L2 soil moisture, which are the only ones providing not-negligible IWU amounts over the California Central Valley.

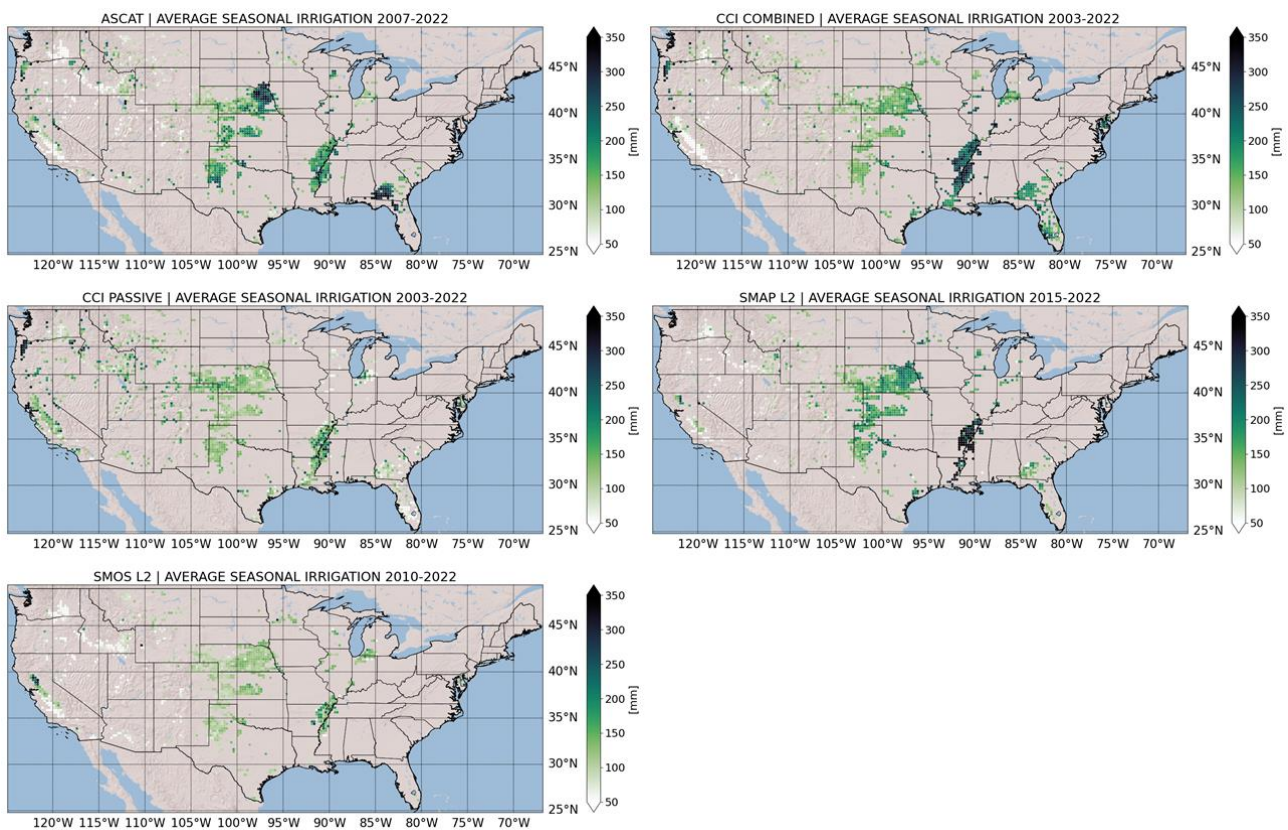


Figure 2.8. Seasonal cumulated IWU amounts over the CONUS averaged during the period adopted in each experiment.

The retrieved IWU amounts have been validated against the Farm and Ranch Irrigation Survey (FRIS) produced by the National Agricultural Statistics Service (NASS) of the United States Department of Agriculture (USDA) (see Deliverable 2 for further details). Country-aggregated FRIS data is available for 2013 and 2018. The comparison between reported and retrieved IWU volumes for 2013 and 2018 is provided in Figures 2.9 and 2.10, respectively. States with reported volumes lower than 0.1 km^3 are not considered in the comparison; because of the range of the data, the logarithmic scale is adopted to properly visualise results. ASCAT and CCI PASSIVE soil moisture products provide similar satisfactory results in terms of *BIAS*, equal to 0.68 km^3 and to 0.87 km^3 , respectively. A notable result in terms of *BIAS* is obtained by leveraging SMOS L2

as well; the value, equal to -0.75 km^3 , highlights a tendency in underestimating reference volumes reported in the FRIS. The *RMSE* values range from 4.23 km^3 to 5.79 km^3 , with the lowest value referring to results relying on the CCI PASSIVE data set. The comparison for the year 2018 involves estimates obtained by SMAP L2 also (see Figure 2.10). The best result in terms of *BIAS* is obtained exploiting the CCI COMBINED data set (*BIAS* equal to 0.18 km^3). Satisfactory *BIAS* values are also found for experiments based on SMAP L2 (0.36 km^3) and CCI PASSIVE (-0.22 km^3) soil moisture. Referring to the *RMSE*, the lowest value of 3.88 km^3 is found for IWU estimates relying on CCI PASSIVE soil moisture; for the other experiments the *RMSE* values are considerably higher, ranging from 5.09 km^3 for SMOS L2 to 6.40 km^3 for ASCAT.

Zaussinger et al. (2019) carried out IWU estimates over CONUS by forcing the SM-Delta approach with coarse resolution soil moisture from SMAP_V5, AMSR2, and ASCAT. On the basis of comparison against reference values from FRIS 2013, they report *BIAS* values ranging from -2.29 km^3 to -2.47 km^3 , systematically higher than those obtained through the experiments carried out with the SM-based inversion approach in this project. Zaussinger et al. (2019) also report *RMSE* spanning between 5.21 km^3 and 5.32 km^3 , thus with a magnitude comparable to results shown in Figures 2.9 and 2.10. Nevertheless, outcomes from the SM-based inversion approach forced with the CCI PASSIVE soil moisture product provide a lower *RMSE*.

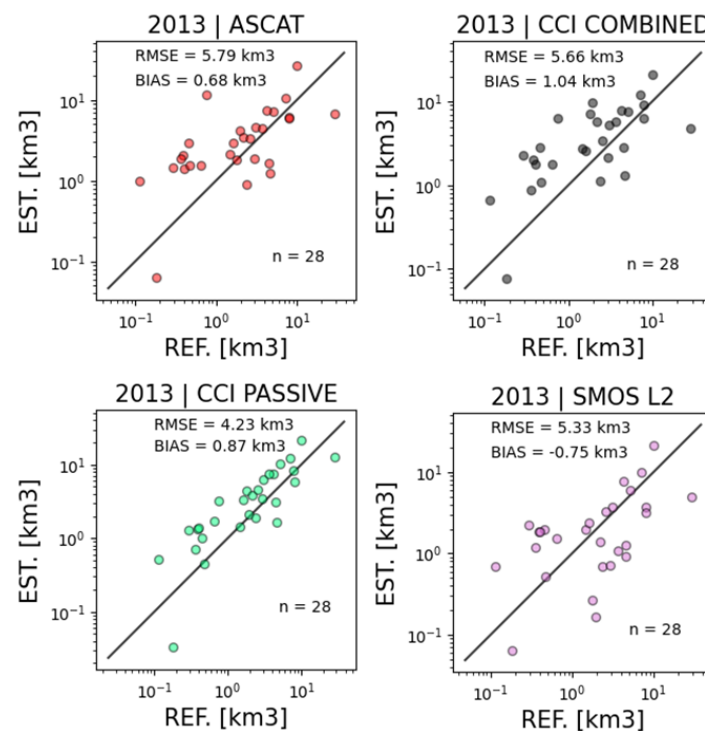


Figure 2.9. Comparison between seasonal reference and estimated IWU volumes in 2013. Note that the logarithmic scale is adopted to properly visualise results.

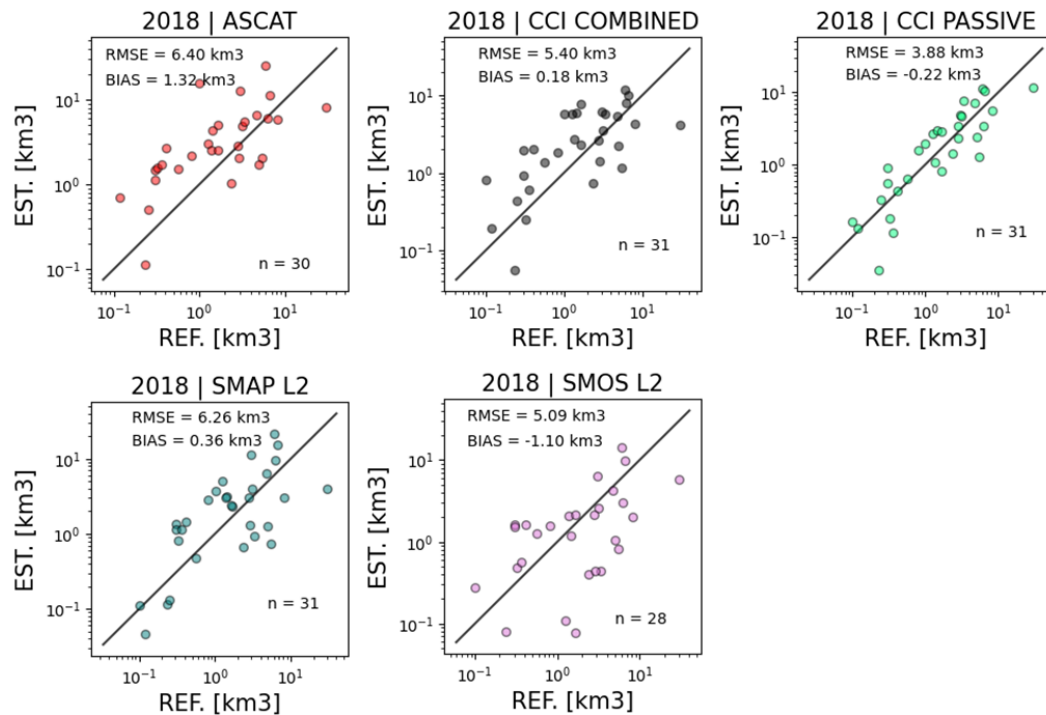


Figure 2.10. Comparison between seasonal reference and estimated IWU volumes in 2018. Note that the logarithmic scale is adopted to properly visualise results.

On the basis of the validation against FRIS data, the best performing soil moisture product per each state is shown in Figure 2.11. CCI PASSIVE results as the best performing data set for retrieving IWU estimates over the majority of states. It outperforms the other data sets in 15 out of the total 28 and 31 states considered in 2013 and in 2018, respectively. It is noteworthy that, referring to 2013, SMOS L2 results as the most suitable data set to retrieve IWU over 8 out of 28 states; for 2018, it outperforms the other products in 6 out of the 31 considered states.

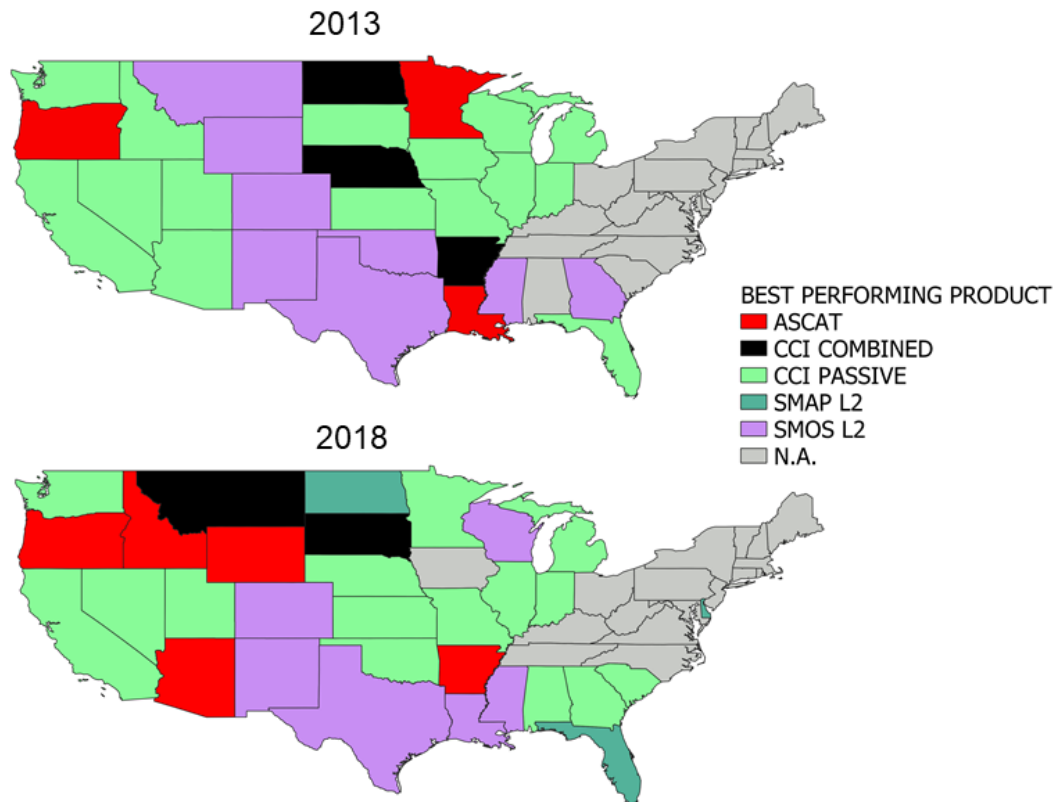


Figure 2.11. Best performing product per each state according to the validation based on FRIS (Farm and Ranch Irrigation Survey) data.

2.3. India

Two irrigation seasons have been considered for retrieving IWU over India: the Rabi (November-March) and the Zaid (April-June) seasons. The average seasonal amounts estimated leveraging the different soil moisture products during the Rabi and Zaid seasons are provided in Figures 2.12 and 2.13, respectively. The highest IWU amounts are generally detected over the Northeastern portion of the country, with estimates relying on the CCI COMBINED soil moisture being considerably lower than the others. A similar behaviour is observed during the Zaid season as well, when IWU retrieved through SMOS L2 data is lower than estimates based on ASCAT, SMAP L2, and CCI PASSIVE soil moisture. It is noteworthy that during the Zaid season less irrigation than during the Rabi season is retrieved (note the different range of values in Figures 2.12 and 2.13). Further insights on the temporal dynamics of the satellite-based IWU can be deduced by the time series of the spatially averaged amounts shown in Figure 2.14; a double peak clearly reflecting the two irrigation seasons can be observed for all the experiments carried out. For ASCAT-based IWU estimates, the magnitude reached during the Zaid season is close to the one referring to the Rabi season, while for the other experiments irrigation retrieved during Zaid is much lower than during Rabi. The slope of the interpolating line reported above each panel reveals increasing IWU trends for outcomes based on ASCAT (+0.15 mm/month during 2007-2022), SMAP L2 (+0.18 mm/month during 2015-2022), and SMOS L2 (+0.05 mm/month during 2010-2022) soil moisture. A weakly decreasing trend can be observed for the CCI products; however, it should be noted that, in line with outcomes from other experiments, seasons 2019/20, 2020/21, and 2021/22 are characterised by higher IWU estimates with respect to previous recent seasons. Nevertheless, the CCI products are those with the longest temporal coverage among those examined and during the period 2003-

2010 the amounts of estimated IWU are similar to those referring to the time span 2019-2022. Despite the well-known uncertainties associated to the interpretation of trend analyses referring to short temporal windows, increasing IWU over India is an expected result considering the phenomena of irrigation expansion (Mehta et al., 2024) and of rapid groundwater depletion (Dangar et al., 2021) affecting the country.

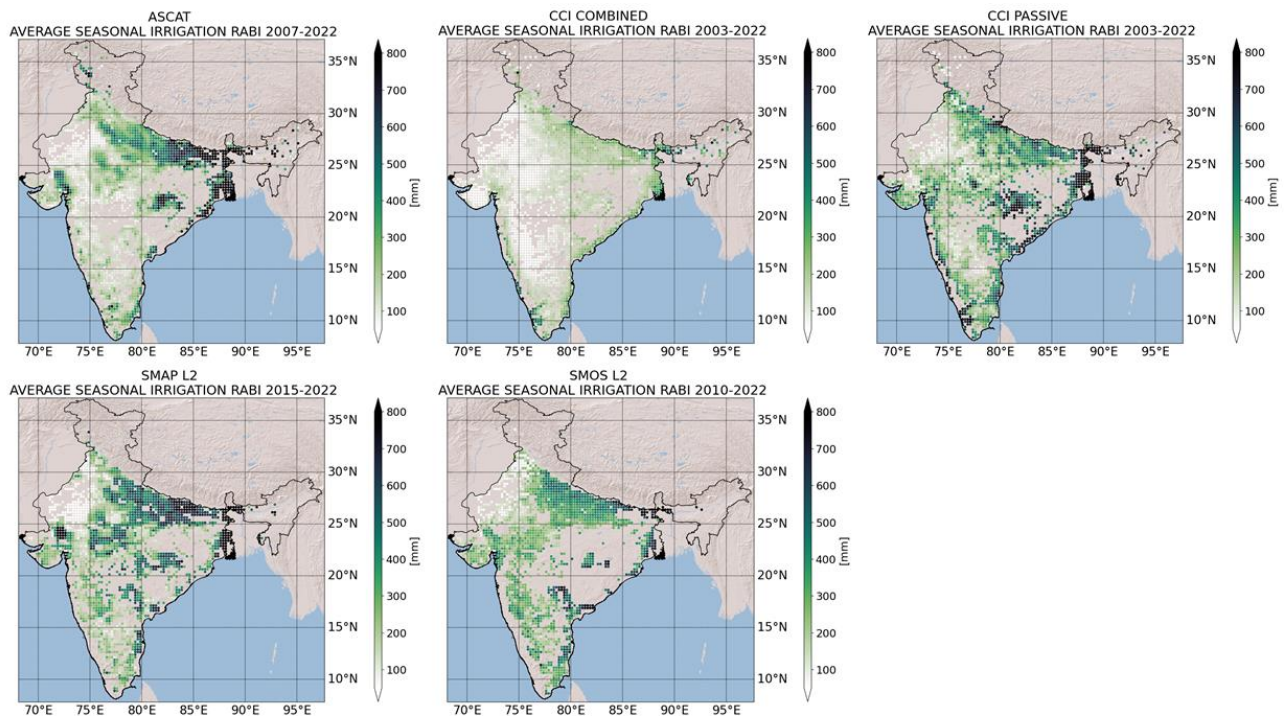


Figure 2.12. Average IWU amounts retrieved over India during the Rabi season.

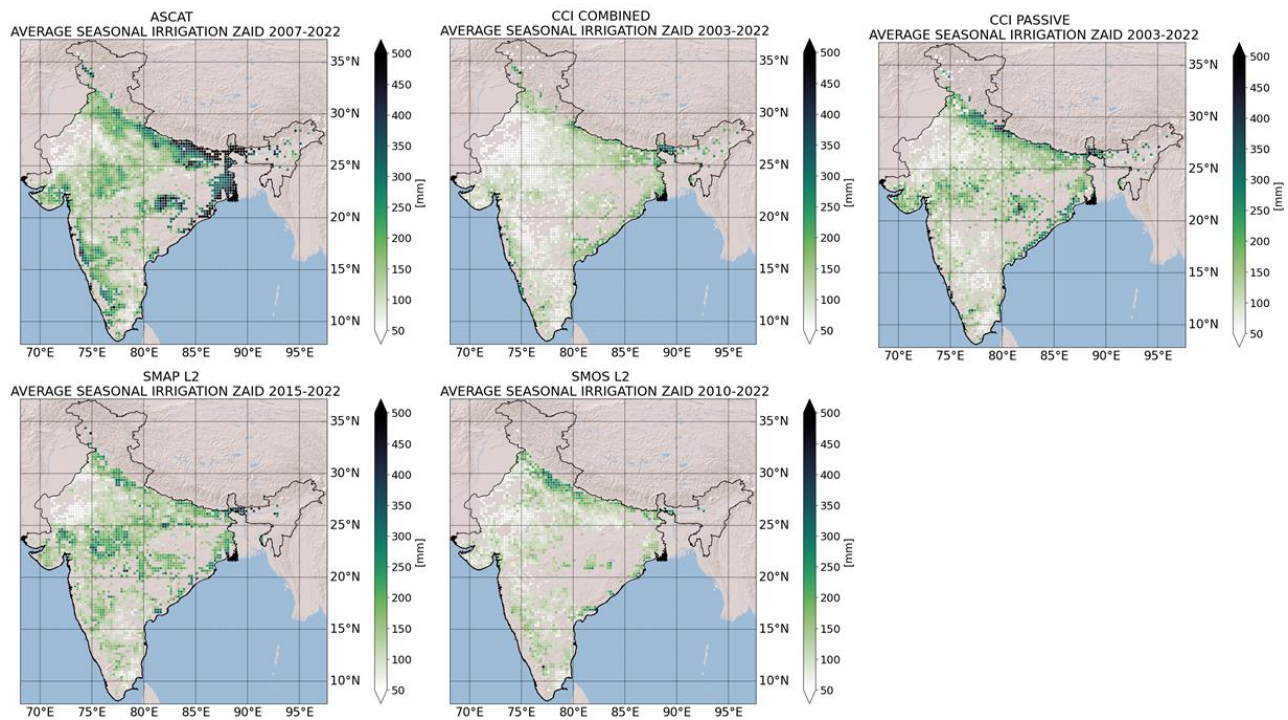


Figure 2.13. Average IWU amounts retrieved over India during the Zaid season.

Reference irrigation amounts over the Sina command area (see Deliverable 2) have been used for validation purposes. It is noteworthy that the district (whose extension is 307.7 km²) is covered by just one pixel of the adopted grid; hence, validation is only possible at the individual pixel level. Moreover, the monthly time series of irrigation water applied over the district is characterised by missing data for whole or partial seasons. Because of all the above uncertainties, we decided to compare annual magnitudes by considering only whole seasons covered by observations. Results are shown in the scatter plots of Figure 2.15. For experiments relying on ASCAT and on the CCI products, the comparison refers to 6 years, decreasing to 4 years for SMOS L2 and to only 2 for SMAP L2. The best result is provided by ASCAT, with a mean relative error equal to -9.6%, widely within the confidence interval of $\pm 30\%$ adopted in previous studies (Dari et al., 2023) and representing the upper limit of the accuracy of satellite-derived irrigation products desired by farmers according to the survey discussed in Massari et al. (2021).

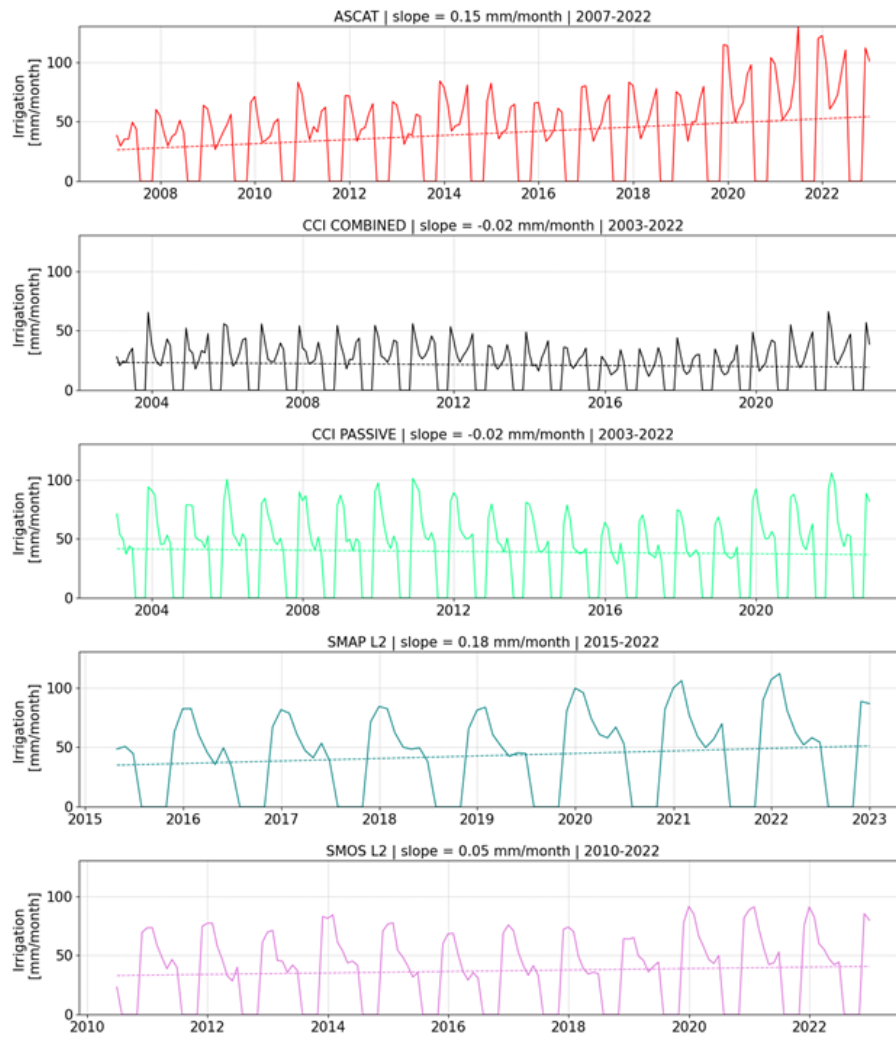


Figure 2.14. Spatially averaged time series of monthly IWU estimated over India according to the different soil moisture products considered.

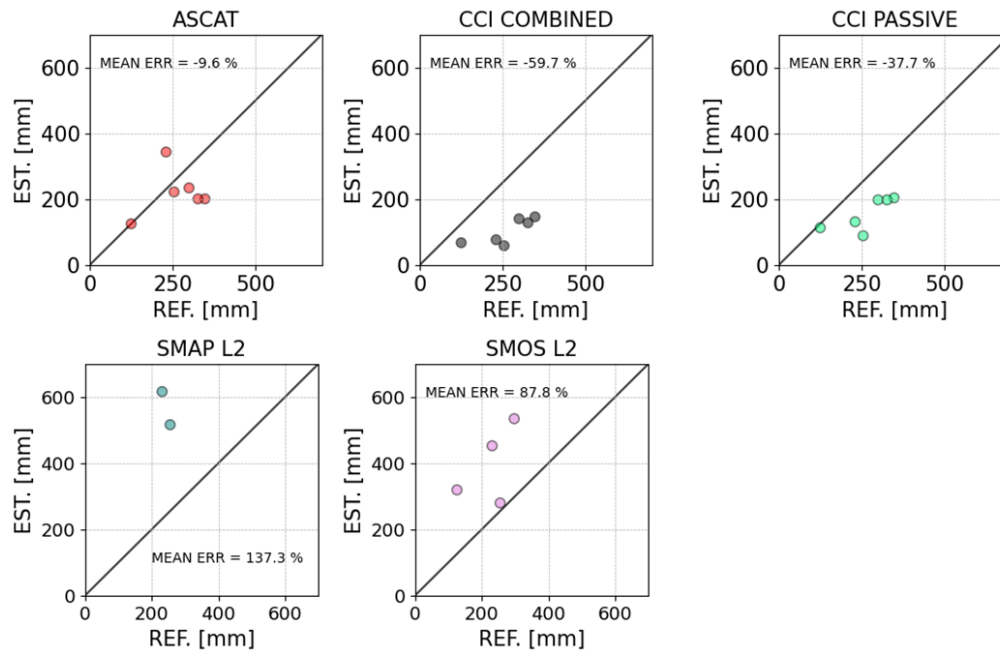


Figure 2.15. Comparison between yearly reference and estimated IWU amounts over the Sina command area (Maharashtra, India).

2.4. Ebro basin (Spain)

Over the Ebro basin, IWU estimates have been produced by considering the period from April to October as the reference irrigation season. The maps in Figure 2.16 show the average seasonal amounts retrieved through the different soil moisture products. The experiment relying on CCI PASSIVE soil moisture is the one providing the highest seasonal IWU rates. It is important to highlight that the Ebro basin is a challenging case study with respect to the CCI-AWU project's aim, as irrigation occurs at a spatial scale much finer than the target resolution of 25 km here adopted. The visual comparison between maps in Figure 2.16 with the one in Figure 2.17 helps in figuring out this issue. Figure 2.17 shows a 1 km resolution map of irrigated (green) and rainfed (brown) agricultural areas recently developed by leveraging Normalised Difference Vegetation Index (NDVI) delivered by the Copernicus Global Land Service (CGLS) (Dari et al., 2024). Irrigation mainly occurs in the basin's central valley (often on narrow portions), so irrigated and non-irrigated areas can be likely mixed together within the 25 km resolution pixels of the target grid. Nevertheless, the reproduction of irrigation patterns is not the main focus of analyses carried out in this precursor project.

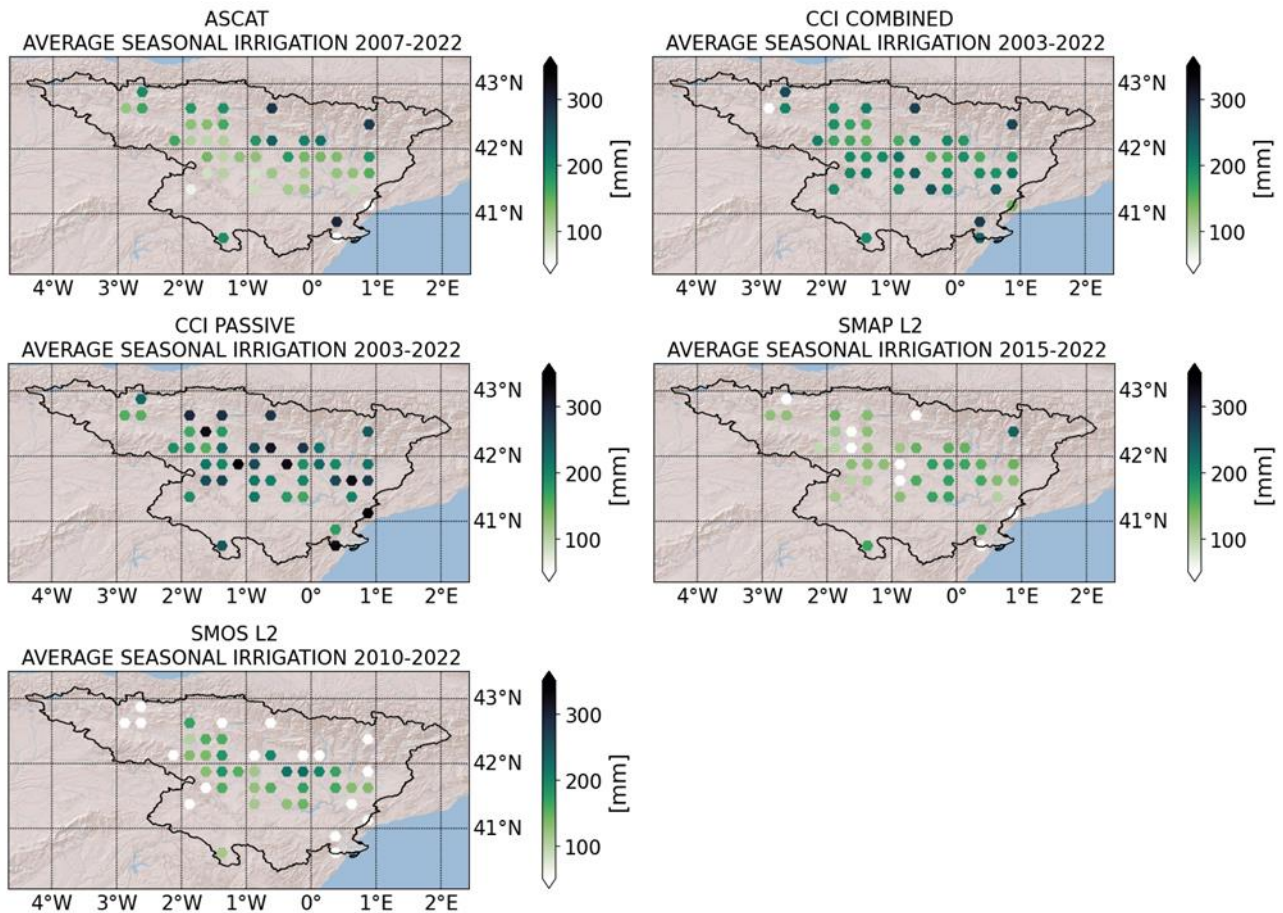


Figure 2.16. Seasonal cumulated IWU amounts over the Ebro basin averaged during the whole period adopted in each experiment.

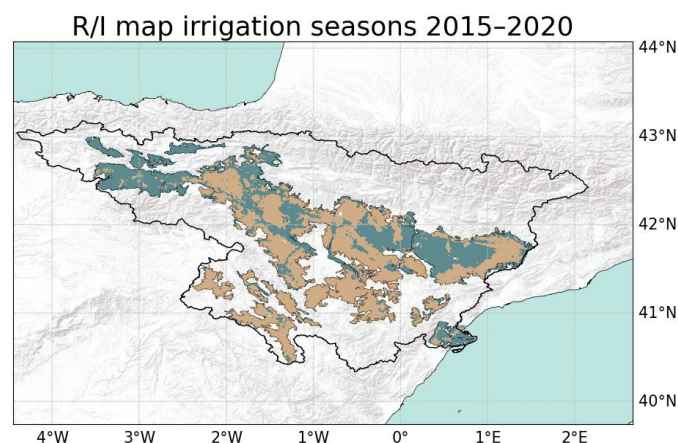


Figure 2.17. 1 km map of rainfed (R, in brown) and irrigated (I, in green) agricultural areas developed by Dari et al. (2024) through NDVI data.

Reference irrigation time series collected over 4 agricultural districts located in the Northeastern portion of the basin have been used for validation purposes. Given that the districts are adjacent to each other and that

their individual extensions (ranging from 70.8 km² to 887.6 km²) are small if compared with the 25 km resolution adopted here, we decided to consider them as a unique irrigated area to be used for the validation. Hence, the time series referring to the different districts have been averaged by adopting weights based on the area of each single district, thus creating a unique time series representing the whole validation domain to be compared with IWU estimates. The comparison at the monthly scale is provided in Figure 2.18; in panel a) the reference values are represented by the light grey shaded area and the satellite-based estimates are indicated in different colours in accordance with the other analyses presented in this report. Performances have been assessed in terms of *RMSE*, *BIAS*, and *r*, which are reported above each plot of panel a). Because of the different temporal coverage of the satellite soil moisture products evaluated, only results referring to ASCAT and to the two CCI products are directly comparable during the whole period of information availability (2007-2022). Performance metrics during the sub-periods covered by the experiments based on SMAP L2 (2015-2022) and on SMOS L2 (2011-2022) data sets are summarised in panels b) and c), respectively. Referring to the period 2007-2022, CCI PASSIVE outperforms ASCAT and CCI COMBINED according to all the metrics taken into account, with *RMSE* equal to 28.39 mm/month, *BIAS* equal to -21.23 mm/month, and *r* = 0.64. The CCI PASSIVE soil moisture proves to be the most suitable data set to retrieve IWU among those evaluated considering also the sub-periods overlapping with SMAP L2 availability (compare metrics in panel b) with those in panel a) referring to the experiment based on SMAP L2 data) and with SMOS L2 availability (compare metrics in panel c) with those in panel a) referring to the experiment based on SMOS L2 data).

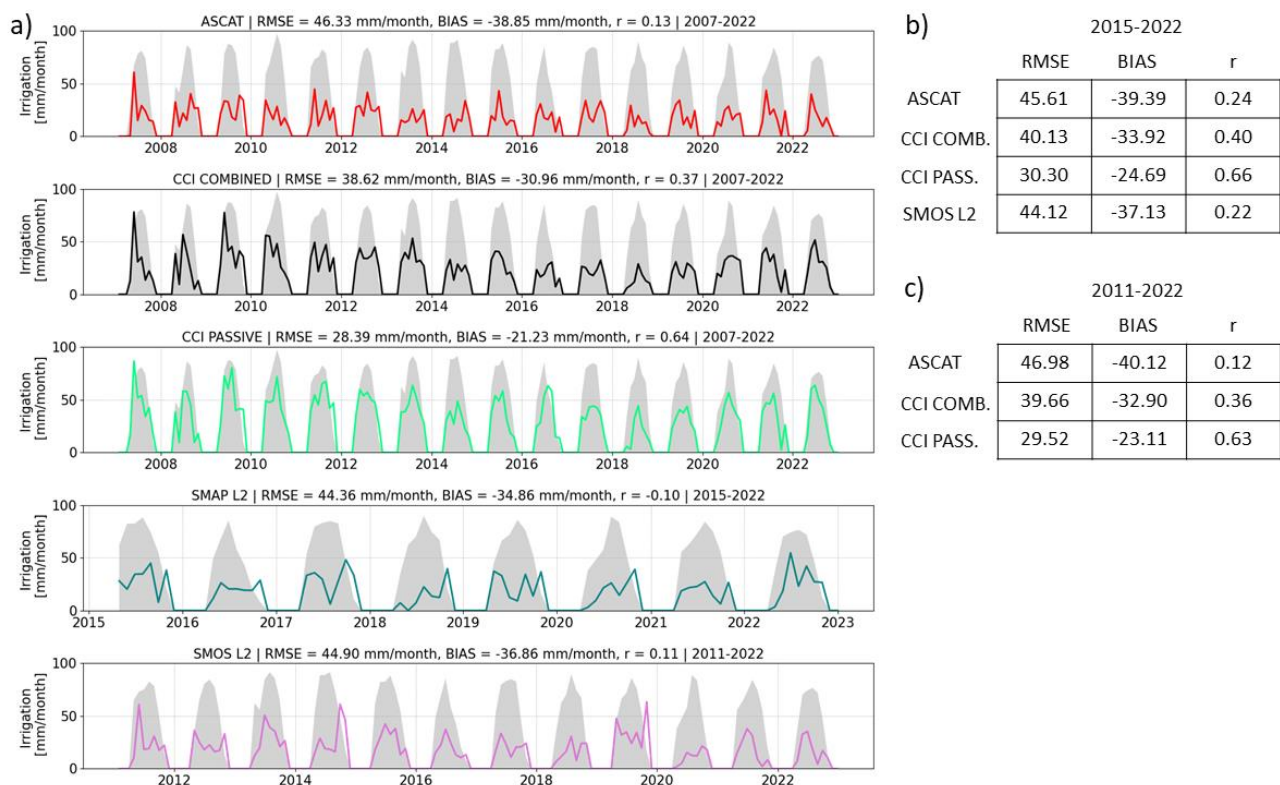


Figure 2.18. Panel a): monthly time series of estimated IWU against reference values over the pilot agricultural districts of the Ebro basin. *RMSE*, *BIAS*, and Pearson correlation, *r*, values are reported above the panels. Panels b) and c) report the same metrics but calculated considering the shorter periods matching with SMAP L2 and SMOS L2 availability, respectively.

Dari et al. (2023) produced regional data sets of satellite-based IWU at 1 km resolution over the Ebro basin by exploiting Sentinel-1 soil moisture retrieved through the first-order Radiative Transfer (RT1) model (Quast et al., 2023). Results obtained in Dari et al. (2023) highlight the added value of high-resolution data in agricultural contexts like the one existing in the Ebro basin; in that study, the authors carried out a validation at the bi-weekly temporal scale, reporting *RMSE* ranging from 10.08 to 14.66 mm/14-day, *BIAS* varying between -8.82 to -2.23 mm/14-day, and *r* spanning from 0.53 to 0.78. The lower limits of such values, if reported on a monthly scale, are comparable to those obtained in the experiment exploiting the CCI PASSIVE product. Nevertheless, results presented in Dari et al. (2023) refer to the entire year and not to the main watering season only; a more in-depth comparison between IWU estimates developed in this project and existing products is among next activities foreseen by the project planning.

3. Validation of the SM-based delta approach

3.1. Introduction

The six monthly irrigation datasets generated with the SM-DELTA approach have been validated across the study areas of India, the Ebro Basin, the Murray-Darling Basin, and CONUS. For the Ebro, Murray-Darling, and CONUS regions, the six datasets (CCI COMBINED & SSEBop, CCI PASSIVE & SSEBop, CCI ACTIVE & SSEBop, CCI COMBINED & FLUXCOM, CCI PASSIVE & FLUXCOM, CCI ACTIVE & FLUXCOM) were validated against in situ irrigation data. In the India region, spatial and temporal patterns were analyzed in relation to climate for three datasets (CCI COMBINED & FLUXCOM, CCI PASSIVE & FLUXCOM, CCI ACTIVE & FLUXCOM). Validation metrics include Root Mean Square Deviation (RMSD), bias, and Pearson's correlation coefficient (R).

3.2. CONUS

We compared the irrigation volumes from the six datasets with state-level annual irrigation volumes for 2013 and 2018, obtained from the United States Department of Agriculture's Irrigation and Water Management Survey. To convert pixel water depths (mm) to state-level volumes (km³), each pixel's water depth was multiplied by its surface area, calculated as follows:

$$\text{Pixel area} = (0.25 \cdot 111.32) \cdot (0.25 \cdot 111.32 \cdot \cos(\text{latitude})) \quad (1)$$

Figure 3.1 presents maps with the average irrigation amounts for the irrigation season (May to September), computed over 2003–2022 for datasets using SSEBop and 2003–2020 for those using FLUXCOM. Visual inspection reveals that all six datasets consistently indicate higher irrigation volumes in the primary irrigated regions of CONUS, particularly in the California Valley, Snake River Valley, and Great Plains. Differences between datasets are primarily driven by the ET product used, with the use of SSEBop generally yielding higher irrigation volumes, especially in the three key irrigated areas mentioned. Soil moisture (SM) products have a smaller impact on seasonal irrigation amounts, with CCI ACTIVE typically yielding lower irrigation volumes compared to CCI COMBINED and CCI PASSIVE.

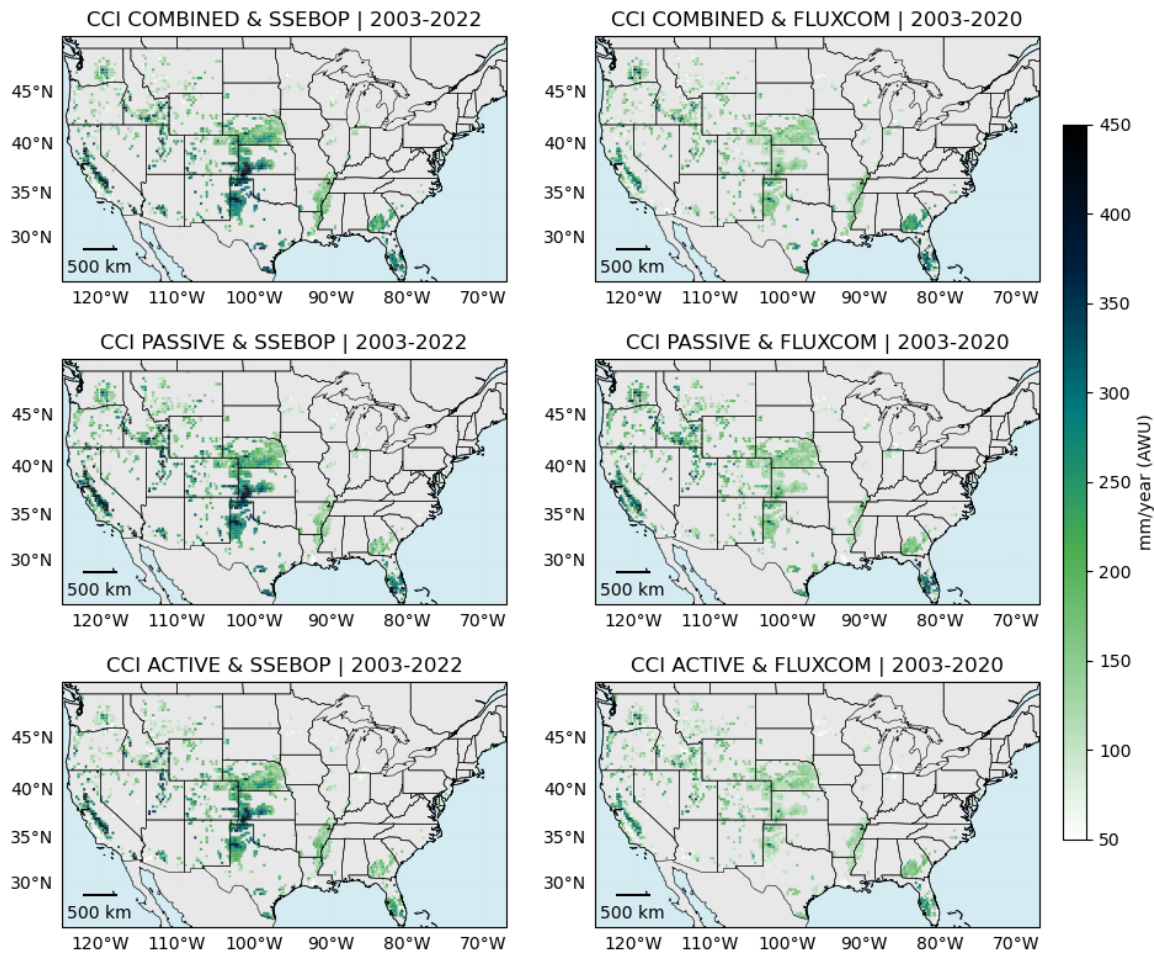


Figure 3.1: Average seasonal irrigation amounts (May–September) across CONUS for the six irrigation datasets generated with the SM-DELTA approach.

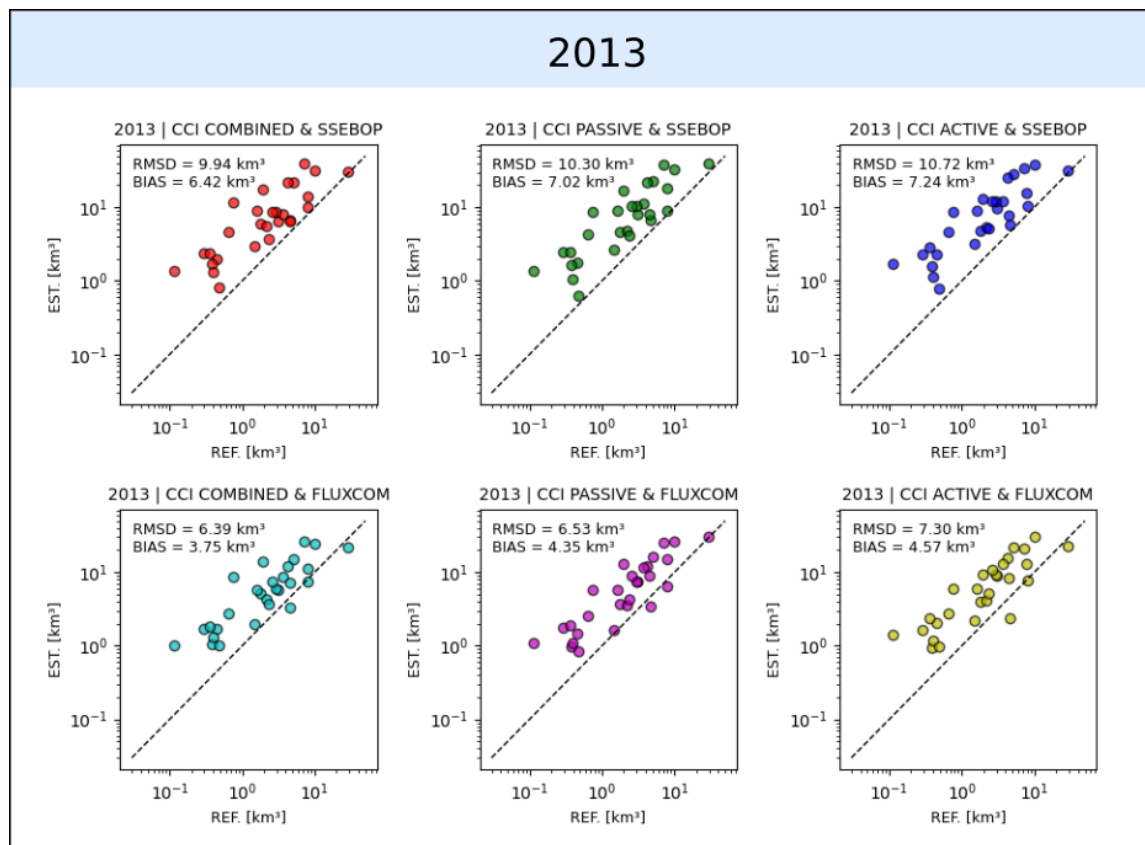
Figure 3.2 shows scatterplots for 2013 and 2018, comparing reported annual irrigation volumes per state (x-axis) with retrieved irrigation volumes (y-axis) for the six datasets, along with RMSD and bias values. The scales are logarithmic, and states with volumes below 0.1 km^3 were excluded. Table 3.1 summarizes the performance of the six SM-DELTA irrigation datasets using RMSD and bias metrics.

Results show an approximately linear relationship across all datasets, though a consistent overestimation of irrigation is observed. The six datasets utilizing the SSEBop ET product show a more pronounced overestimation (mean RMSD of $9.82 \text{ km}^3/\text{year}$, bias of $6.16 \text{ km}^3/\text{year}$) compared to those using the FLUXCOM ET product (mean RMSD of $5.42 \text{ km}^3/\text{year}$, bias of $3.10 \text{ km}^3/\text{year}$). It is worth noting that these metrics primarily reflect states with high irrigation water consumption and provide limited insight into states with minimal irrigation. The CCI COMBINED & FLUXCOM dataset demonstrates the best performance across both 2013 and 2018.

Table 3.1: RMSD and bias metrics obtained for the six SM-DELTA irrigation datasets over CONUS in 2013 and 2018.

	2013		2018	
	RMSD (km^3)	Bias (km^3)	RMSD (km^3)	Bias (km^3)

CCI COMBINED & SSEBOP	9.94	6.42	9.19	5.04
CCI PASSIVE & SSEBOP	10.30	7.02	9.22	5.36
CCI ACTIVE & SSEBOP	10.72	7.24	9.53	5.89
CCI COMBINED & FLUXCOM	6.39	3.75	4.63	1.58
CCI PASSIVE & FLUXCOM	6.53	4.35	4.16	1.90
CCI ACTIVE & FLUXCOM	7.30	4.57	4.51	2.43



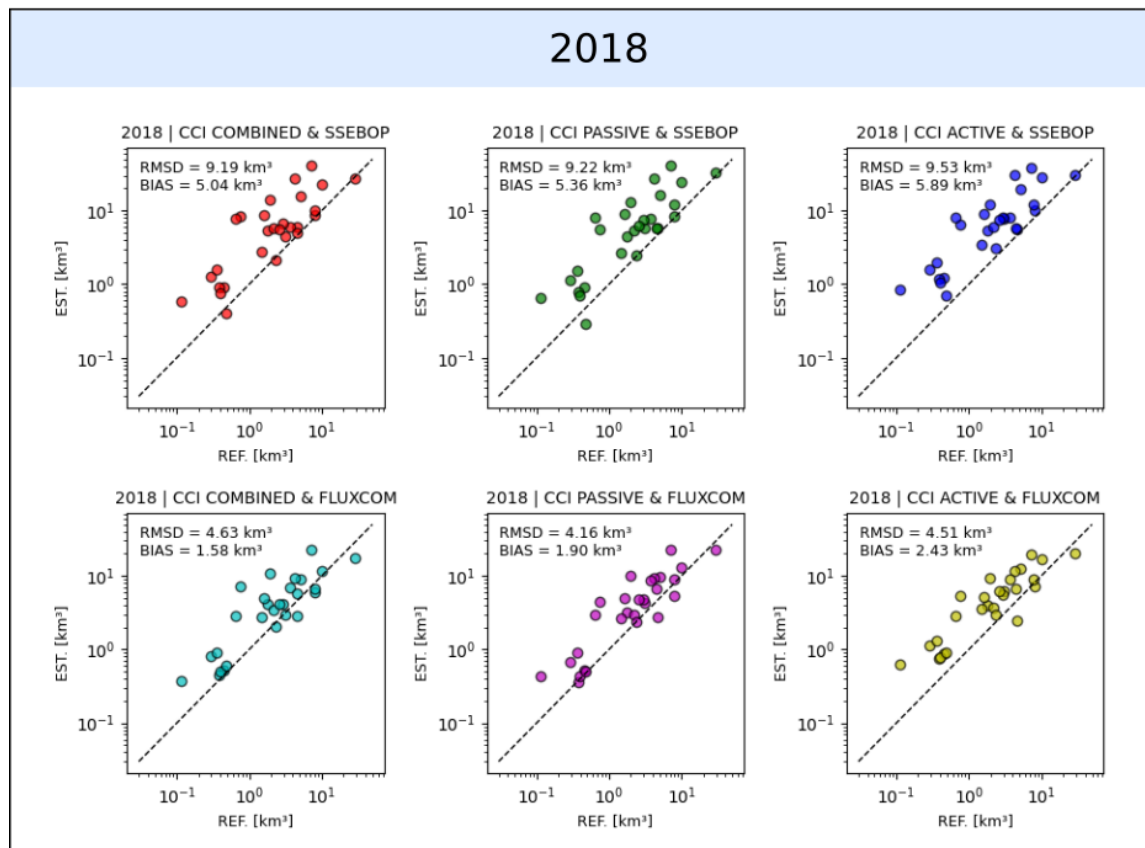


Figure 3.2: Scatterplots of estimated vs. reported irrigation volumes with RMSD and bias for six SM-DELTA datasets over CONUS in 2013 and 2018.

3.3. Ebro basin

We validated the six irrigation datasets using monthly irrigation data collected from five irrigation districts located in the eastern part of the Ebro basin (cf. Figure 3.3). Given the scale mismatch between the pixel size (0.25°) and the size of the irrigation districts, we averaged the in situ irrigation data across the five districts to create a single, larger virtual district. The validation period spans 2007 to 2020, during which RMSD, bias, and R were computed as performance metrics. For validation purposes, only pixels with at least 25% of their area covered by the irrigation district were included.

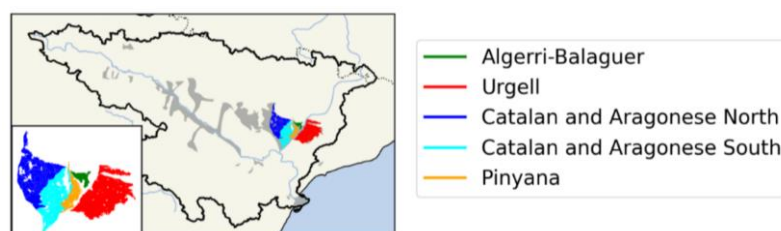


Figure 3.3: Irrigated districts with available in situ data in the Ebro basin.

Figure 3.4 shows maps of the Ebro basin with the average irrigation season (March to October) obtained with the six different irrigation datasets on the Ebro basin.

A visual inspection reveals that:

- In contrast to results from CONUS, the type of SM product has a greater influence on irrigation estimates than the choice of ET product.
- Areas known to be intensively irrigated—such as pixels in the northeast of the district and those in the southeast near the Ebro Delta—correspond to the pixels showing the highest irrigation levels across all six datasets.

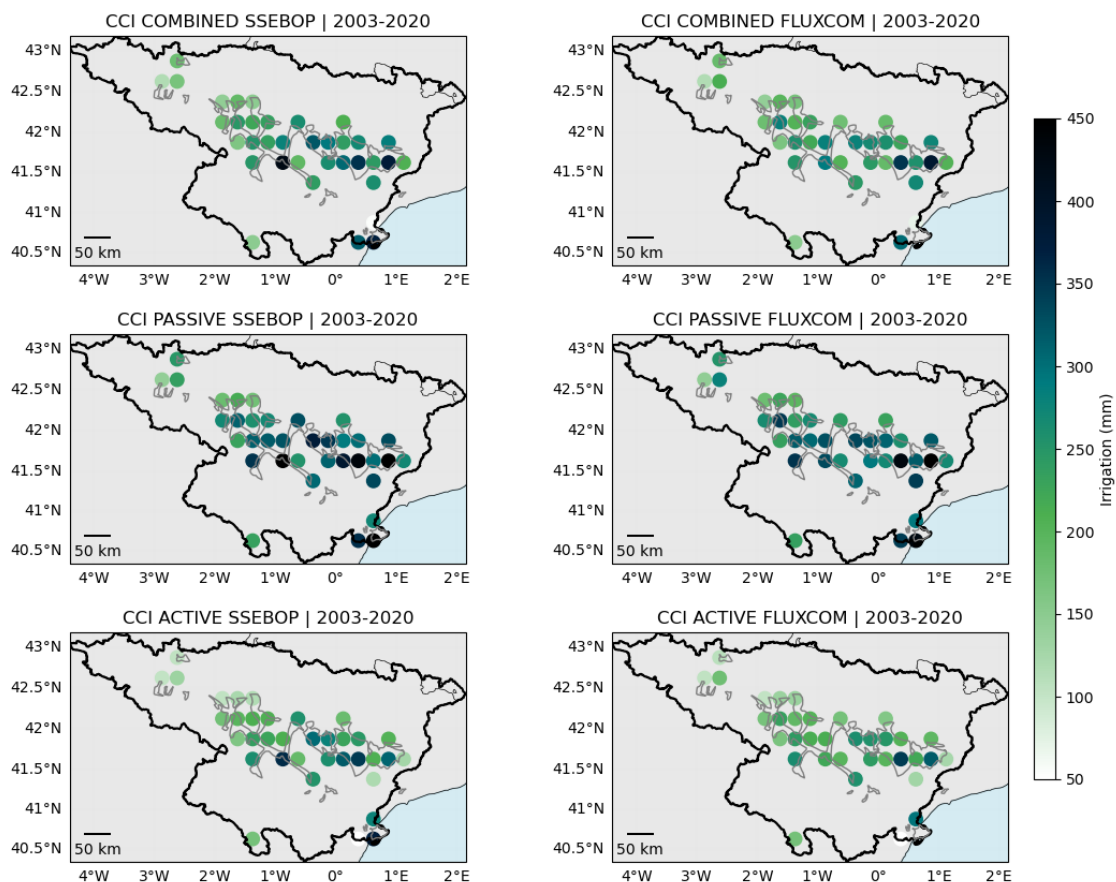


Figure 3.4: Average annual irrigation obtained with the six irrigation datasets retrieved using the SM-DELTA approach over the Ebro Basin.

Figure 3.5 presents time series from 2007 to 2020 of monthly irrigation estimates from the six irrigation datasets (blue line) alongside observed in situ data (shaded area). Table 3.2 summarizes the performance of each dataset over the Ebro irrigation districts in terms of RMSD, bias, and R. Note that these metrics were calculated exclusively for the irrigation season (April to October).

Overall, the irrigation dynamics are reasonably well captured, with an average R of 0.54. The highest correlation ($R = 0.72$) was achieved with the CCI COMBINED & SSEBop dataset, while the lowest ($R = 0.35$)

was observed with CCI ACTIVE & FLUXCOM. All datasets tend to underestimate irrigation, with an average bias of -19.46 mm/month. The smallest bias (-15.71 mm/month) was recorded with CCI PASSIVE & SSEBop, and the largest (-23.28 mm/month) with CCI COMBINED & FLUXCOM. The average RMSD across datasets is 29.96 mm/month, with CCI PASSIVE & SSEBop showing the lowest (26.57 mm/month) and CCI ACTIVE & FLUXCOM the highest (33.12 mm/month). Among the six datasets, CCI PASSIVE & SSEBop demonstrated the best overall performance across the five irrigation districts in the Ebro Basin.

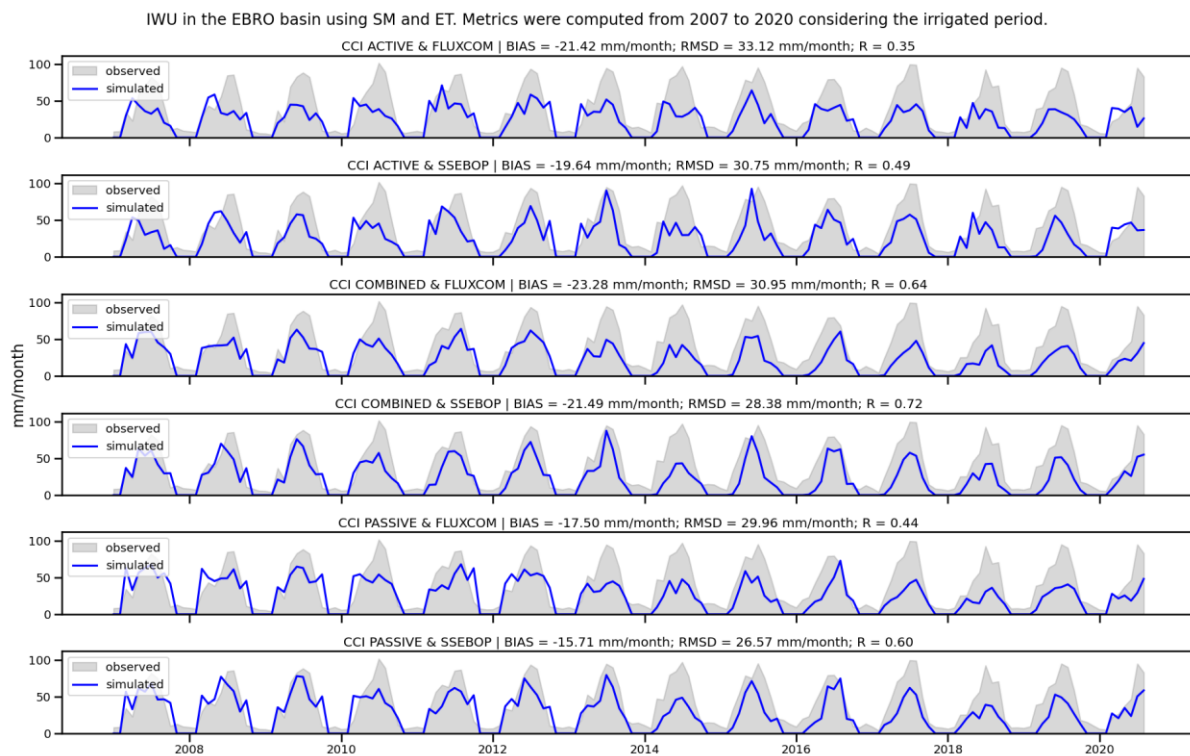


Figure 3.5: Time series of observed (shaded area) and simulated (blue line) monthly irrigation from 2007 to 2020 for the six irrigation datasets retrieved with the SM-DELTA approach over the irrigation districts in the Ebro basin.

Interestingly, the results for the CONUS states show an overestimation of retrieved irrigation compared to in situ data across all six datasets, whereas the Ebro irrigation districts exhibit an underestimation with all six datasets. These discrepancies can be attributed to differences in ET behavior across the study areas. Specifically, when comparing the different $ET_{w/irrig}$ and ET_{w/o_irrig} products across the four study areas, we observed variations in temporal dynamics and quantities during the irrigation season between the regions. Notably, ET products appear to have a greater impact on the retrieved irrigation in CONUS, while ET data seem to have a more limited effect on retrieved irrigation in the Ebro basin.

The differences between CONUS and the Ebro district can also be explained by the fact that the overestimated irrigation volumes observed for CONUS are strongly influenced by the surface area defined by the spatial mask used. The spatial mask is designed to exclude false irrigation signals; however, if it is not sufficiently restrictive, unmasked pixels—where irrigation is simulated despite being very little or not irrigated—may contribute to the overestimation of irrigation.

Table 3.2: Metrics (Bias, RMSD, and R) obtained for the six irrigation datasets retrieved with the SM-DELTA approach over the irrigation districts in the Ebro basin.

	Ebro (all 5 districts)		
	Bias (mm/month)	RMSD (mm/month)	R (-)
CCI ACTIVE & FLUXCOM	-21.42	33.12	0.35
CCI ACTIVE & SSEBOP	-19.64	30.75	0.49
CCI COMBINED & FLUXCOM	-23.28	30.95	0.64
CCI COMBINED & SSEBOP	-21.49	28.38	0.72
CCI PASSIVE & FLUXCOM	-17.50	29.96	0.44
CCI PASSIVE & SSEBOP	-15.71	26.57	0.60

3.4. Murray-Darling basin

We compared the six irrigation datasets with monthly irrigation data collected from four irrigation districts located in the southern Murray-Darling basin (cf. Figure 3.6). The in situ data used for validation covers the period from 2010 to 2019 for the Coleambally, Murray-Wakool, and Murray-Mulwala districts, and from 2014 to 2019 for the Murrumbidgee district. As with the Ebro Basin districts, only pixels with at least 25% of their area covered by the irrigation district were included for comparison.

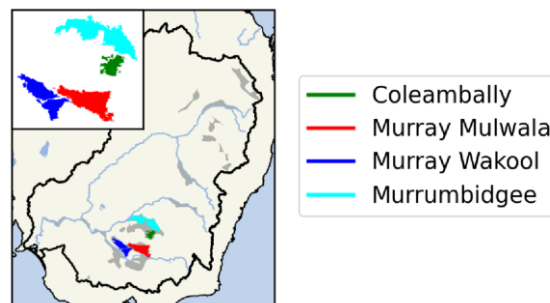


Figure 3.6: Irrigated districts with available in situ data in the Murray-Darling basin

Figure 3.7 presents maps with the average irrigation estimated during the irrigated season (September to April) as estimated by the six different irrigation datasets across the Murray-Darling Basin. A visual inspection reveals that the CCI COMBINED & FLUXCOM, CCI PASSIVE & FLUXCOM, and CCI ACTIVE & FLUXCOM datasets generate higher irrigation estimates on nearly all irrigated pixels compared to the CCI COMBINED & SSEBop, CCI PASSIVE & SSEBop, and CCI ACTIVE & SSEBop products. Similar to the CONUS results, but unlike the Ebro basin, the generated irrigation is more sensitive to the ET product than to the SM product. Interestingly, in contrast to CONUS, the datasets using FLUXCOM produce greater irrigation volumes than those using SSEBop in the Murray-Darling basin.

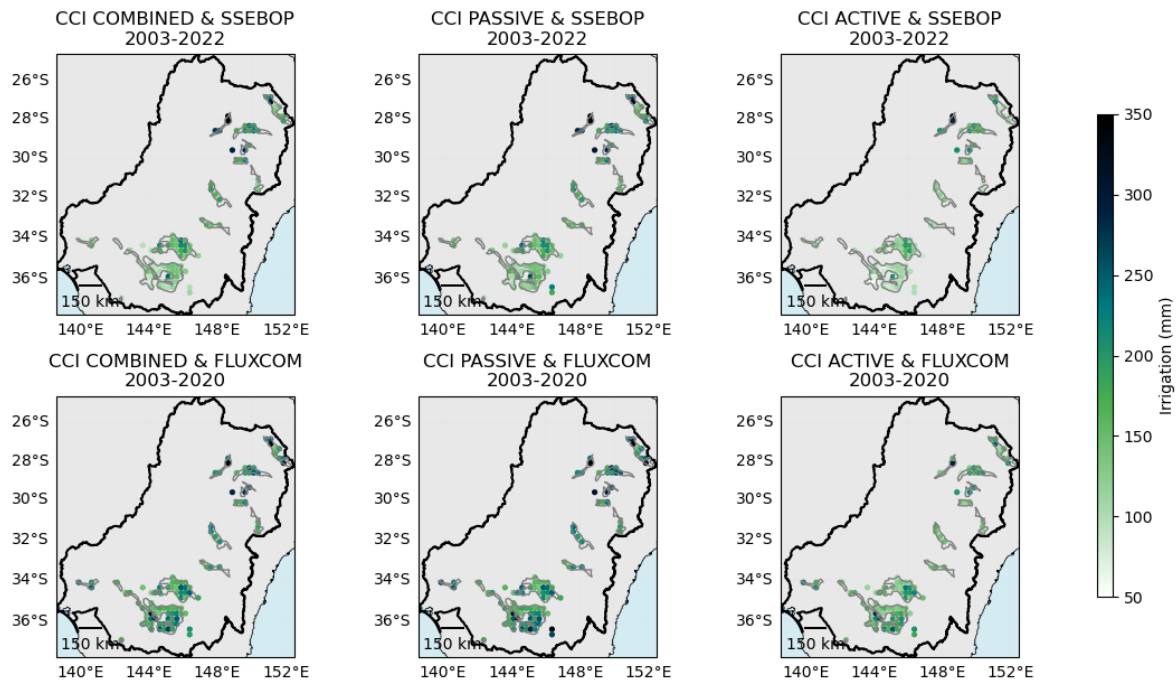


Figure 3.7: Average annual irrigation obtained with the six irrigation datasets retrieved using the SM-DELTA approach over the Murray-Darling Basin.

Figures 3.8 and 3.9 present time series of monthly irrigation from 2010 to 2019 for the six SM-DELTA-derived irrigation datasets (blue lines), compared with the observed in situ data (shaded area) for the Coleambally and Murrumbidgee districts, respectively. The time series of monthly irrigation for the Murray Wakool and Murray Mulwala districts are shown in the Appendix (Figures 3.A1 and 3.A2). Table 3.3 summarizes the performance of the irrigation datasets across the four irrigation districts of the Murray-Darling basin, using the RMSD, bias, and R metrics.

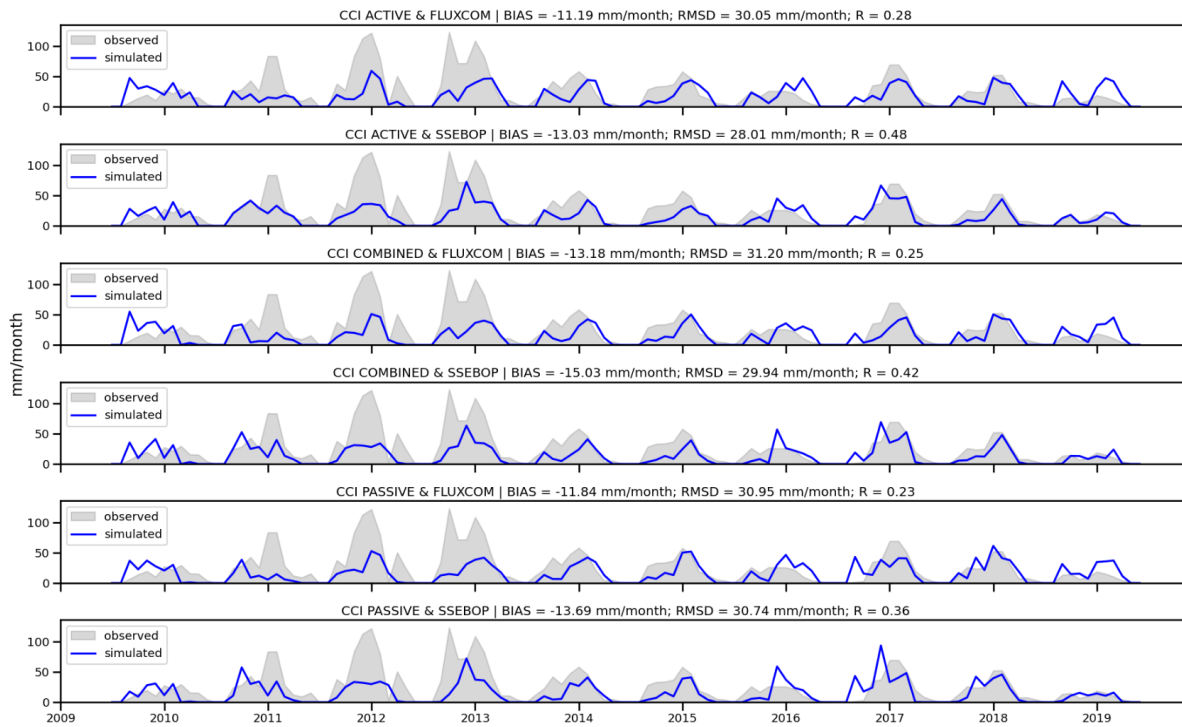


Figure 3.8: Time series of observed (shaded area) and simulated (blue line) monthly irrigation from 2010 to 2020 obtained with the six irrigation datasets retrieved with the SM-DELTA approach over the Coleambally district.

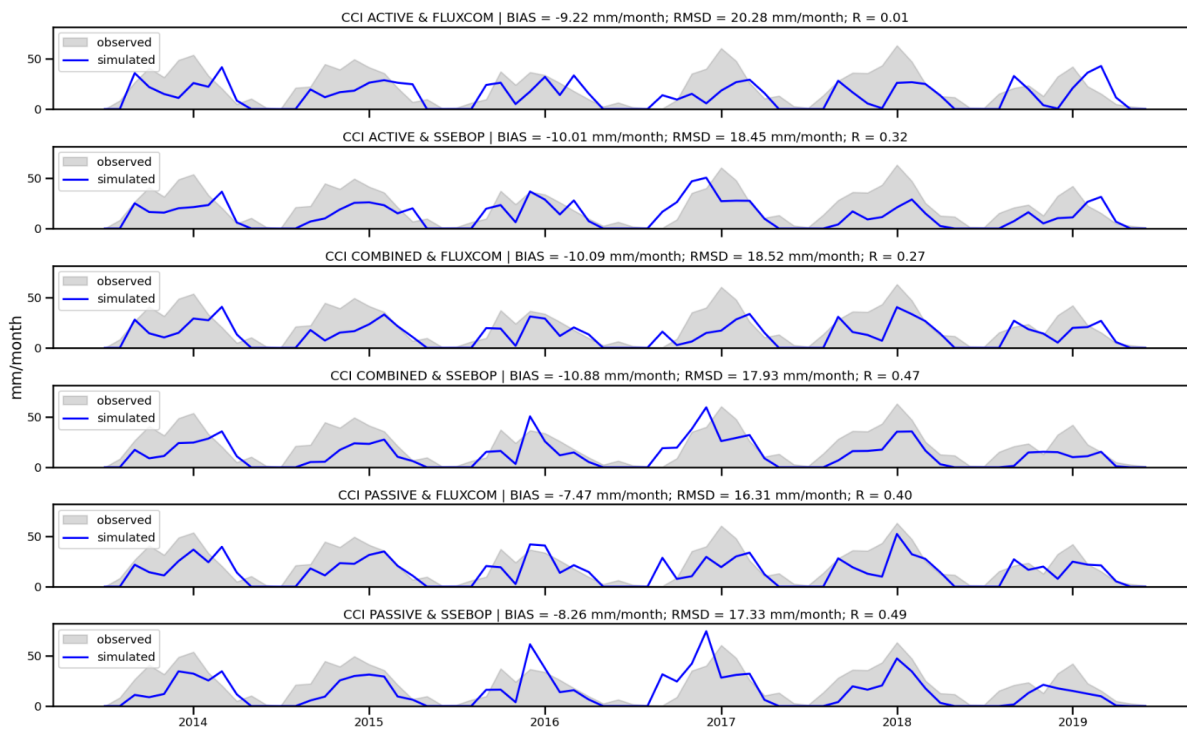


Figure 3.9: Time series of observed (shaded area) and simulated (blue line) monthly irrigation from 2014 to 2019 obtained with the six irrigation datasets over the Murrumbidgee district.

Irrigation dynamics are generally fairly well reproduced, with an average R of 0.34 for Coleambally, 0.22 for Murray-Mulwala, 0.29 Murray-Wakool, and 0.33 Murrumbidgee. All six datasets tend to underestimate the observed irrigation (but to a lesser extent than for the Ebro basin districts), with an average bias of -13.0 mm/month for Coleambally, -7.1 mm/month for Murray-Mulwala, 1.01 mm/month for Murray-Wakool, and -9.3 mm/month for Murrumbidgee. On average, the six datasets provide an RMSD of 30.1 mm/month for Coleambally, 21.4 mm/month for Murray-Mulwala, 14.5 mm/month for Murray-Wakool, and 18.1 mm/month for Murrumbidgee.

The CCI ACTIVE & SSEBOP dataset shows the best performance for the Coleambally and Murray-Mulwala districts, CCI COMBINED & SSEBOP shows the best performance for the Murray-Wakool district, and CCI PASSIVE & SSEBOP shows the best performance for the Murrumbidgee district.

As shown in Figures 9 and 10, the observed irrigation water depth (in mm) is lower during the 2014-2019 period compared to the 2010-2013 period. This trend can primarily be attributed to the expansion of irrigated areas starting in 2014, with the total volume of irrigation remaining comparable to that of the pre-2014 period. As a result, irrigation has been distributed over a larger area, leading to a reduction in the water depth per unit area of irrigation from 2014 onwards.

Table 3.3: Metrics (Bias, RMSD, and R) obtained for the six irrigation datasets retrieved with the SM-DELTA approach over the four irrigation districts in the Murray-Darling basin.

	Coleambally			Murray-Mulwala		
	RMSD (mm/month)	Bias (mm/month)	R (-)	RMSD (mm/month)	Bias (mm/month)	R (-)
CCI ACTIVE & FLUXCOM	30.0	-11.2	0.28	19.9	-5.7	0.26
CCI ACTIVE & SSEBOP	28.0	-13.03	0.48	22.3	-11.6	0.29
CCI COMBINED & FLUXCOM	31.2	-13.2	0.25	20.4	-4.4	0.21
CCI COMBINED & SSEBOP	29.9	-15.0	0.42	22.2	-10.4	0.25
CCI PASSIVE & FLUXCOM	30.9	-11.8	0.23	21.0	-2.2	0.14
CCI PASSIVE & SSEBOP	30.7	-13.7	0.36	22.6	-8.1	0.17
	Murray-Wakool			Murrumbidgee		
	RMSD	Bias	R	RMSD	Bias	R
CCI ACTIVE & FLUXCOM	14.6	3.5	0.20	20.3	-9.2	0.01
CCI ACTIVE & SSEBOP	13.8	-3.5	0.37	18.5	-10.0	0.32
CCI COMBINED & FLUXCOM	15.2	3.9	0.19	18.5	-10.1	0.27
CCI COMBINED & SSEBOP	13.3	-3.1	0.39	17.9	-10.9	0.47
CCI PASSIVE & FLUXCOM	16.2	6.4	0.19	16.3	-7.5	0.40
CCI PASSIVE & SSEBOP	13.7	-0.7	0.37	17.3	-8.3	0.49

3.5. India

Figure 3.10 presents maps of the India region, showing the average annual irrigation derived from three datasets: CCI COMBINED & FLUXCOM, CCI PASSIVE & FLUXCOM, and CCI ACTIVE & FLUXCOM. The irrigation datasets CCI COMBINED & SSEBop, CCI PASSIVE & SSEBop, and CCI ACTIVE & SSEBop were excluded from the analysis due to unrealistically high irrigation values (>1100 mm/year) in the Indo-Gangetic Plain.

Visual inspection of the maps reveals that all three datasets show important irrigation amounts in the Indo-Gangetic Plain, particularly in the Indus Valley, with values reaching up to 600 mm/year. The spatial patterns of irrigation between CCI COMBINED & FLUXCOM and CCI PASSIVE & FLUXCOM are broadly similar, though the latter shows greater irrigation amounts in the southern regions of India. In contrast, CCI ACTIVE & FLUXCOM generally exhibits lower irrigation volumes across the southern regions.

The significant irrigation quantities retrieved in the northwest, particularly within the Indus Basin, align with the region's intensive agricultural activities and arid to semi-arid climate, where crop water demands are high due to limited rainfall. For instance, crops such as rice, which requires 900–2500 mm per growing cycle, and wheat, which demands 450–650 mm per cycle (Allen et al., 1998), are widely cultivated here.

Similarly, substantial irrigation retrieved in southern India, particularly in Tamil Nadu and Karnataka, can be attributed to the semi-arid climate. While these areas receive moderate monsoonal rainfall, extensive irrigation is often needed during the dry seasons to sustain crops such as rice, sugarcane, and cotton, which require 700–1200 mm per growing cycle (Allen et al., 1998). Overall, the spatial distribution of the retrieved irrigation aligns quite well with regional climatic conditions and agricultural water requirements.

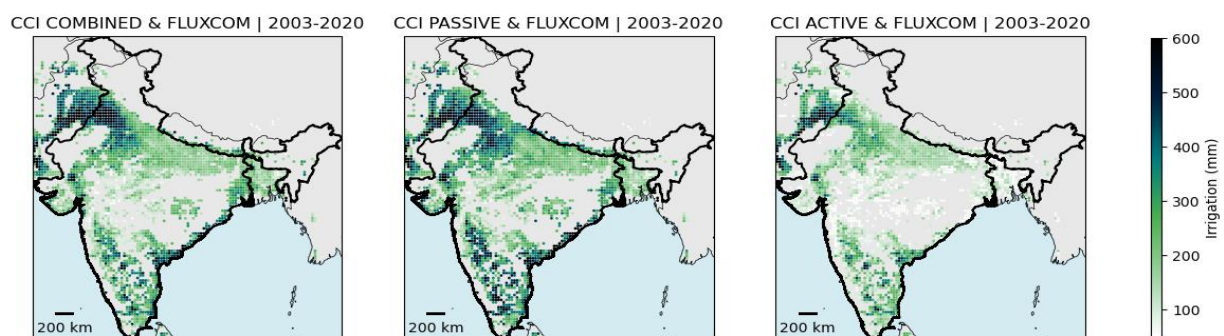


Figure 3.10: Average annual irrigation obtained with the CCI COMBINED & FLUXCOM (left), CCI PASSIVE & FLUXCOM (center), and CCI ACTIVE & FLUXCOM (right) irrigation datasets using the SM-DELTA approach over the India region (2003–2020).

To further investigate the spatio-temporal dynamics of irrigation in the India region, time series of irrigation data derived from the three datasets were analyzed across three distinct climatic zones within the highly irrigated Indo-Gangetic Plain (see the three climatic areas in Figure 3.11). These regions include the Indus region (Köppen climate classification BWh, hot desert), Ganges West (BSh, hot semi-arid), and Ganges East (Cwa, humid subtropical). The Ganges East region receives substantial monsoonal rainfall, resulting in lower irrigation requirements compared to the Ganges West and Indus regions.

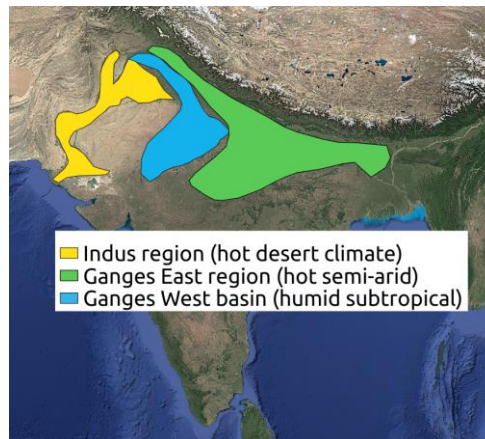


Figure 3.11: Areas with different climates in the Indo-Gangetic plain used for irrigation datasets analysis, categorized by Köppen climate classifications.

Figure 3.12 illustrates the seasonal irrigation cycles (average for the period 2003–2020) derived from the datasets CCI COMBINED & FLUXCOM, CCI PASSIVE & FLUXCOM, and CCI ACTIVE & FLUXCOM. The plots indicate the primary agricultural seasons in India: Rabi (dry season, November to March), Zaid (intermediate season, April to May), and Kharif (monsoon season, June to October). For each season, the average monthly irrigation amounts (based on the three datasets) are also shown.

Overall, the irrigation dynamics are broadly similar across the three datasets, with CCI ACTIVE & FLUXCOM consistently reporting lower irrigation volumes than the other two datasets, while CCI COMBINED & FLUXCOM and CCI PASSIVE & FLUXCOM report comparable quantities.

The irrigation patterns observed align well with the climatic characteristics of each region. The Indus region (hot desert climate) exhibits the highest irrigation volumes, with a noticeable decrease during the Zaid season. This is consistent with the lower agricultural demand in Zaid, as it is an intermediate season with fewer crops requiring irrigation. The Ganges West region (hot semi-arid climate) shows lower irrigation volumes than the Indus region, particularly during the Kharif season, reflecting the higher humidity (and thus less need for irrigation) during the monsoon. Finally, the Ganges East region (humid subtropical climate) exhibits the lowest irrigation quantities throughout the year, with particularly low irrigation during the Rabi and Kharif periods, consistent with the region's more humid climate.

The observed monthly irrigation values (averaging 27.5 mm/month for Rabi, 27.7 mm/month for Zaid, and 27.3 mm/month for Kharif) are in line with the findings of Kragh et al. (2023), who estimated irrigation volumes based on the differences between modeled ET (without irrigation) and three ET products (with irrigation) across three areas of the Indo-Gangetic Plain similar to the ones we investigate.

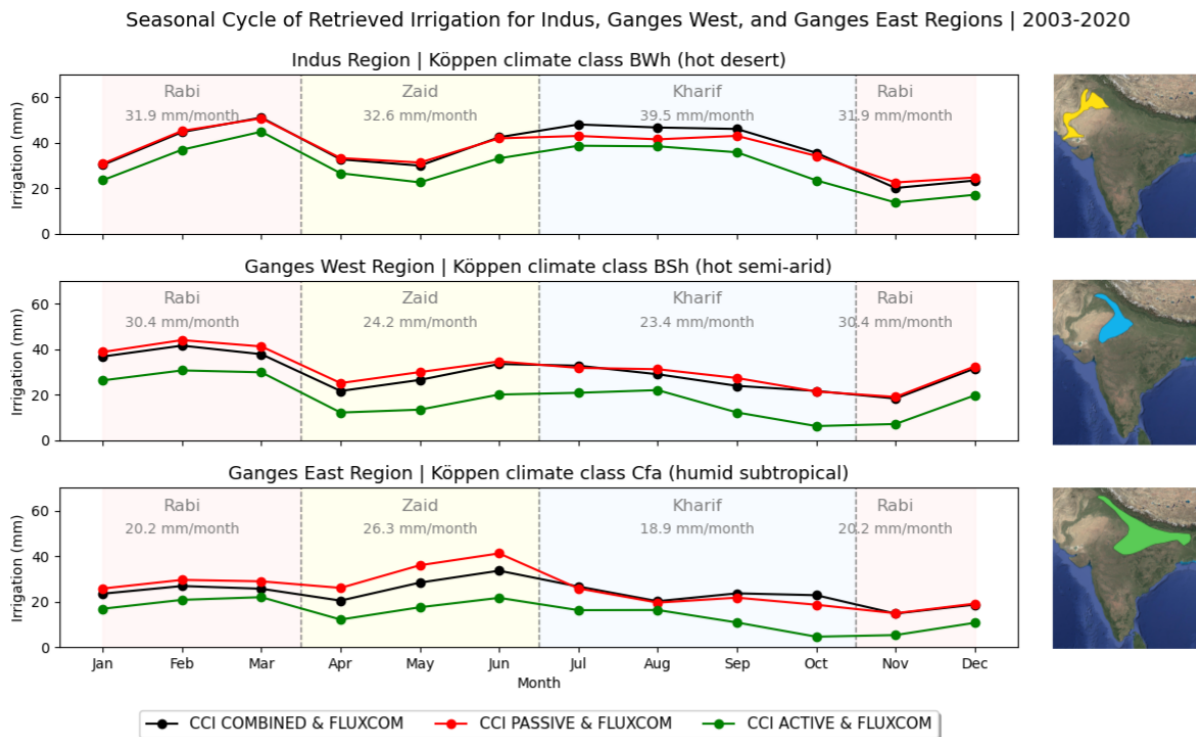


Figure 3.12: Average monthly irrigation in the Indus, Ganges West, and Ganges East Regions obtained with the CCI COMBINED & FLUXCOM (black line), CCI PASSIVE & FLUXCOM (red line), and CCI ACTIVE & FLUXCOM (green line) datasets. The Rabi, Zaid, and Kharif seasons are indicated in color, along with the corresponding mean monthly irrigation.

3.6. Summary and conclusion

Irrigation estimates generated with the SM-DELTA algorithm, utilizing different sources of SM and ET data, were validated against in situ irrigation data for the CONUS, Ebro basin, and Murray-Darling regions. Additionally, the spatio-temporal patterns of irrigation across various climatic zones in the India region were analyzed.

In the CONUS region, a linear relationship was observed between the estimated and observed annual irrigation volumes at the state level for the six SM-DELTA-derived irrigation datasets, for the years 2013 and 2018. However, all datasets showed an overestimation of irrigation volumes, especially those using SSEBop data. The CCI COMBINED & FLUXCOM dataset exhibited the best performance for the two evaluation years (2013 and 2018).

For the Ebro basin, irrigation dynamics measured in the irrigation districts were reasonably well reproduced by the SM-DELTA algorithm, although all six datasets consistently underestimated irrigation volumes. The CCI PASSIVE & SSEBOP dataset demonstrated the best performance over the irrigation districts.

In the Murray-Darling basin, irrigation dynamics were similarly well reproduced across four irrigation districts, with a general underestimation in irrigation volumes across all six datasets. This underestimation was, however, less pronounced than in the Ebro basin. The CCI ACTIVE & SSEBOP dataset performed best overall across the four irrigation districts in Murray-Darling.

In the India region, the spatial patterns from the CCI COMBINED & FLUXCOM and CCI PASSIVE & FLUXCOM datasets aligned well with agricultural practices and climate conditions, showing more irrigation in the Indo-

Gangetic plain (especially in the Indus basin) and in the semi-arid southern regions. Analysis by climate zone further confirmed consistency between irrigation volumes, dynamics, and crop water requirements.

3.7. Appendix

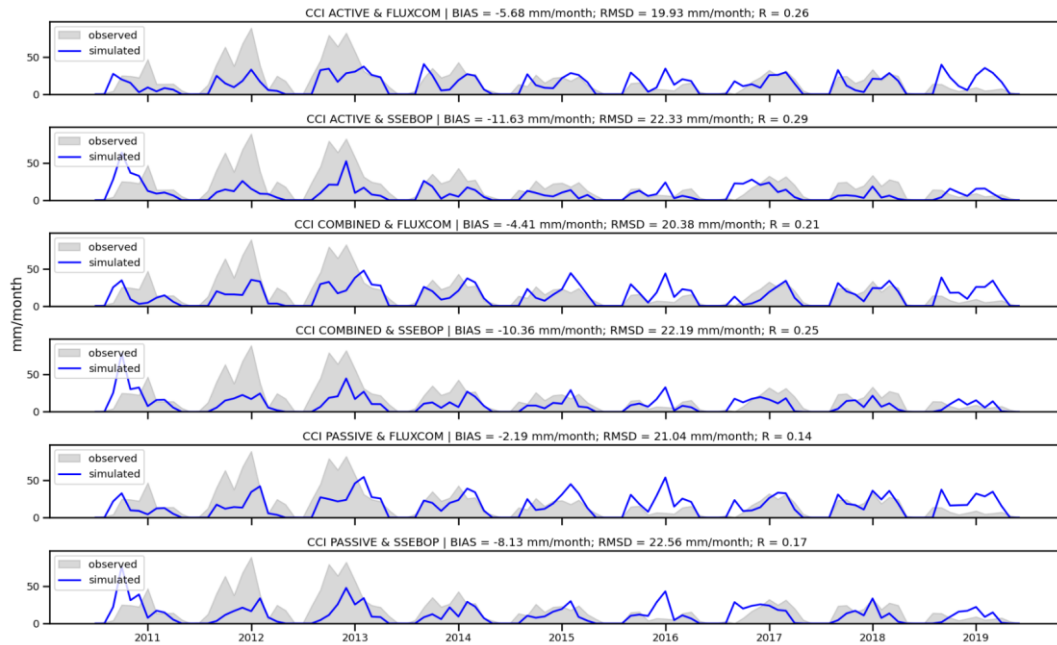


Figure 3.A1: Time series of observed (shaded area) and simulated (blue line) monthly irrigation from 2011 to 2019 obtained with the six irrigation datasets over the Murray-Mulwala district.

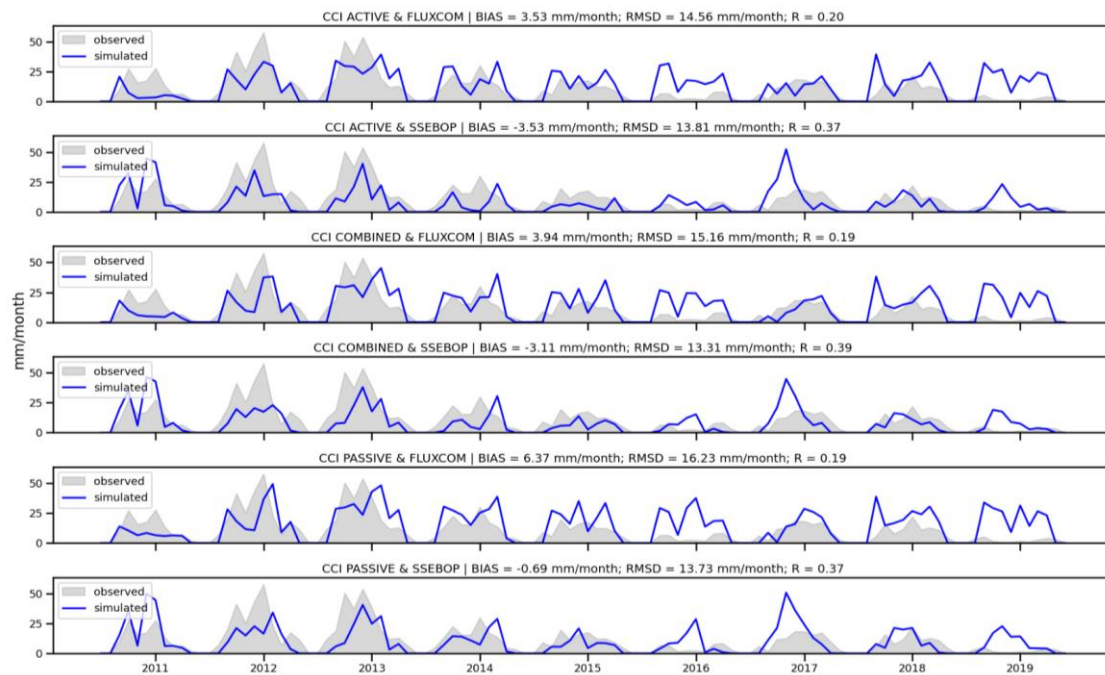


Figure 3.A2: Time series of observed (shaded area) and simulated (blue line) monthly irrigation from 2011 to 2019 obtained with the six irrigation datasets over the Murray Wakool district.

4. Validation of the Flux-based approach

4.1. Introduction

Irrigation datasets have been created using the FLUX-BASED approach. Irrigation derived from the FLUX-BASED algorithm ($I_{\text{FLUX-BASED}}$) corresponds to the difference between $ET_{\text{FLUX-BASED}}$ ($ET_{\text{FLUX-BASED}} = \text{Precipitation} - \text{Total Water Storage} - \text{Discharge}$) and ET_{w/o_irrig} (from NOAA-MP and ERA5-Land, theoretically containing no irrigation signal). This method has been newly developed as part of the ESA CCI AWU project, and its performance and suitability as a reasonable candidate for developing a new ECV are tested here.

The irrigation datasets analyzed are those obtained for the four main irrigated regions of the CONUS (California Valley, Snake River Plain, Great Plains, and Mississippi Floodplains), and one rainfed region in eastern CONUS (referred to as the Rainfed region) (see map Figure 4.1). The regions vary in the percentage of area equipped for irrigation. Table 4.1 presents the average percentage of surface area equipped for irrigation, based on data from the Global Map of Irrigation Areas (GMIA; Siebert et al., 2015) for each of the five regions.

The validation analysis consists of a spatial and temporal comparison between $I_{\text{FLUX-BASED}}$ and $I_{\text{SM-DELTA}}$. $I_{\text{SM-DELTA}}$ is the irrigation dataset obtained with the SM-DELTA approach (WP320) using CCI COMBINED soil moisture and FLUXCOM evapotranspiration data. The latter is used here as benchmark irrigation data, as it showed good correlation with observed annual irrigation by CONUS state, and satisfactory RMSD ($5.51 \text{ km}^3/\text{year}$ on average) and average bias ($2.66 \text{ km}^3/\text{year}$ on average) values.

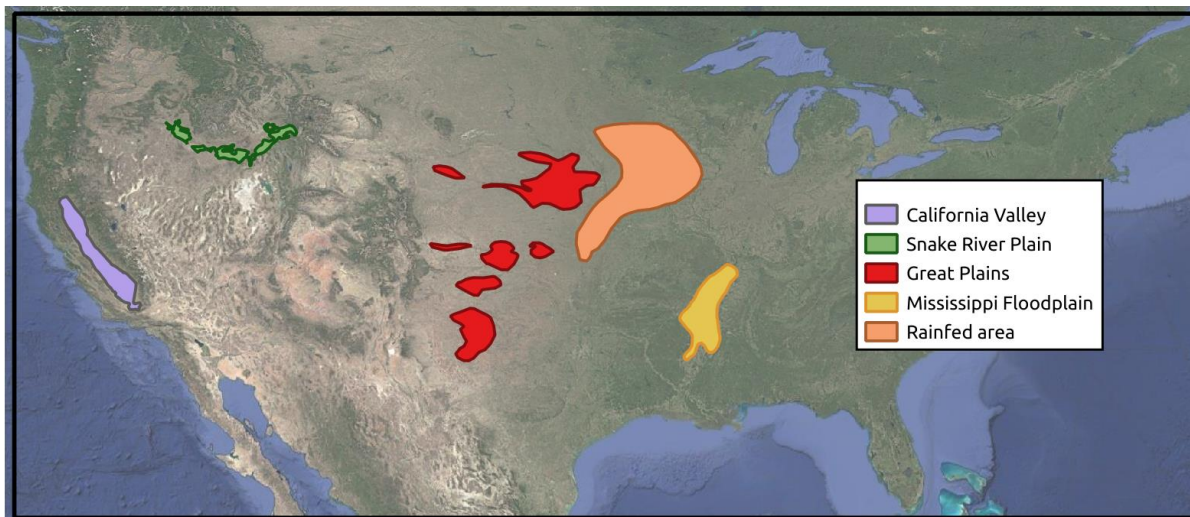


Figure 4.1: Map of CONUS with the five regions analyzed.

Table 4.1: Average % of area equipped for irrigation (GMIA, Siebert et al., 2005).

Area	Average % of area equipped for irrigation
California	58 %
Snake River Plain	45 %

Great Plains	33 %
Mississippi Floodplain	47 %
Rainfed	0 %

4.2. IFLUX-BASED analysis across the five selected regions

4.2.1. California Valley

Figure 4.2 shows the California Valley region with average monthly irrigation (computed over the period May–September) obtained with the FLUX-BASED approach ($I_{\text{FLUX-BASED}}$; on the left and at watershed scale), and with the SM-DELTA approach ($I_{\text{SM-DELTA}}$; on the right and at pixel scale). The figure shows that $I_{\text{SM-DELTA}}$ generates more irrigation (>50 mm/month on the most irrigated pixels) than $I_{\text{FLUX-BASED}}$ (with values ranging from 5 to around 20 mm/month).

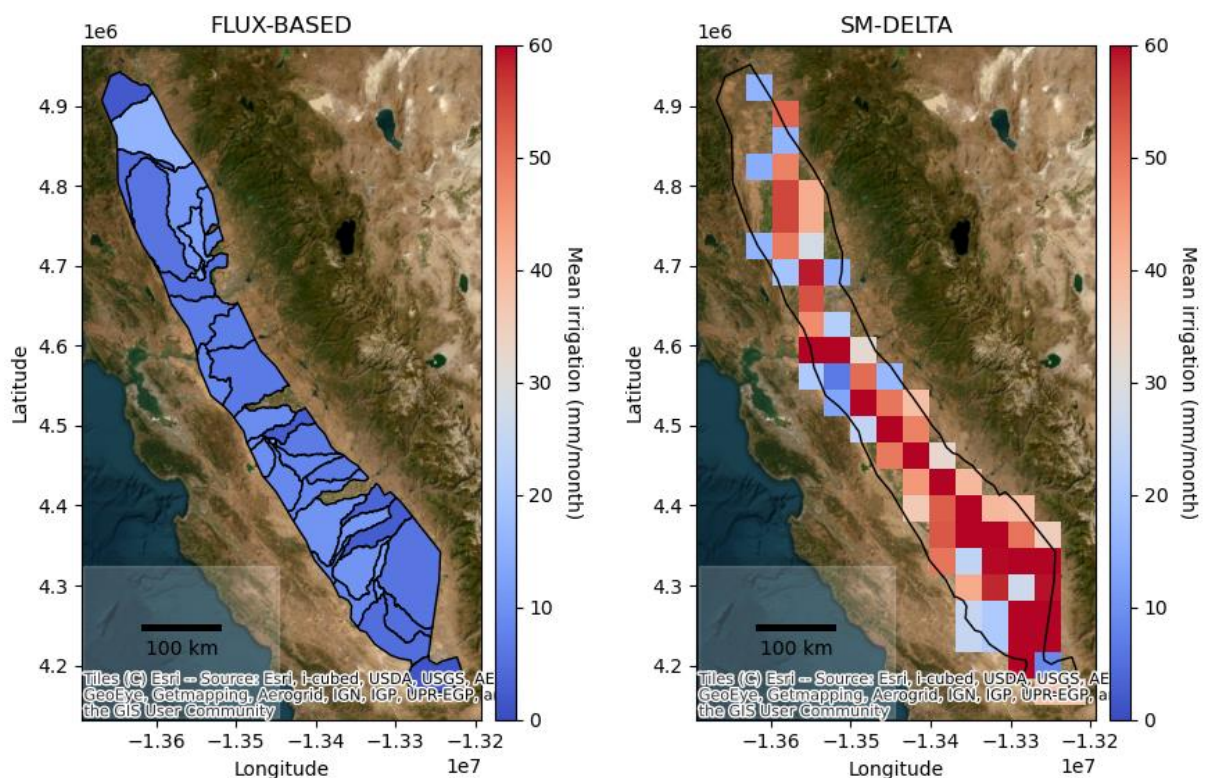


Figure 4.2: Map of irrigation retrieved with the FLUX-BASED approach (left) and with the SM-DELTA approach (right) over the California Valley region.

Figure 4.3 shows the seasonal cycle of $ET_{\text{FLUX-BASED}}$ and $ET_{\text{w/o_irrig}}$ ($I_{\text{FLUX-BASED}}$ is calculated as the difference between the two). $ET_{\text{FLUX-BASED}}$ is larger than $ET_{\text{w/o_irrig}}$ from July to September, suggesting the potential of $ET_{\text{FLUX-BASED}}$ to detect irrigation during the irrigated season. Note that the seasonal cycle represents an average of ET and therefore does not reflect the variability of $ET_{\text{FLUX-BASED}}$.

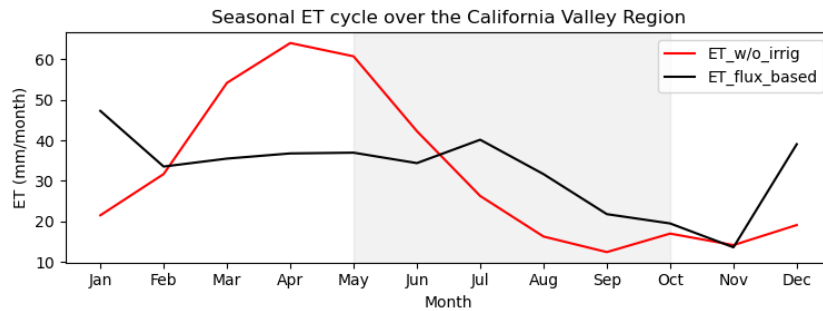


Figure 4.3: Seasonal cycle of $ET_{FLUX-BASED}$ (black line) and ET_{w/o_irrig} (red line) computed over the period 2001-2020 for the California Valley region.

Figure 4.4 shows the monthly $I_{FLUX-BASED}$ (green line) and $I_{SM-DELTA}$ (orange line) averaged over the California Valley region for the period 2004 to 2020. Note that the months not coinciding with the irrigation season (May to September) are masked. We can see a significant difference in the amount of irrigation retrieved with the two algorithms: $I_{FLUX-BASED}$ shows an average irrigation of 38 mm/season (standard deviation of 21 mm/season) and $I_{SM-DELTA}$ and average of 217 mm/season (standard deviation of 26 mm/season). Furthermore, $I_{FLUX-BASED}$ shows greater variability (e.g. 2006 shows very little irrigation, while 2019 shows substantially more) than $I_{SM-DELTA}$ (showing irrigation at its peak systematically in July, in line with the fact that crop water requirements are highest during this month).

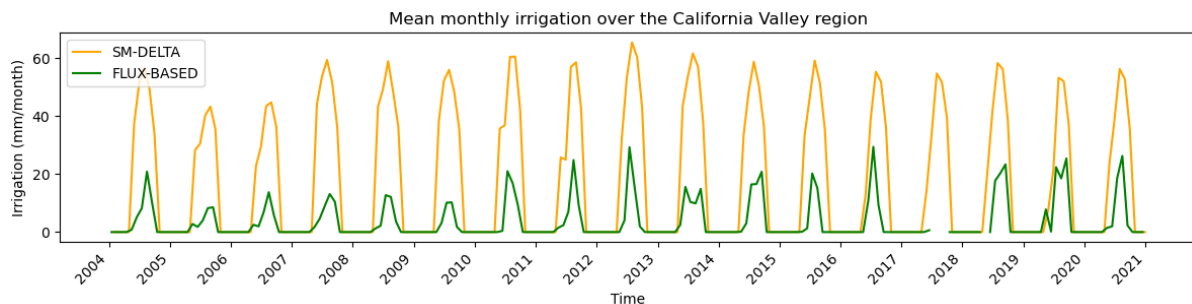


Figure 4.4: Monthly irrigation retrieved for the California Valley region using the FLUX-BASED approach (green line) and the SM-DELTA approach (yellow line).

4.2.2. Snake River Plain

Figure 4.5 shows the Snake River Plain region with $I_{FLUX-BASED}$ (left), and $I_{SM-DELTA}$ (right). As with the California Valley region, $I_{SM-DELTA}$ generates more irrigation quantities than $I_{FLUX-BASED}$ on the irrigated pixels. The seasonal cycle (Figure 4.6) shows $ET_{FLUX-BASED}$ being slightly larger than ET_{w/o_irrig} during the peak irrigation period from July to September.

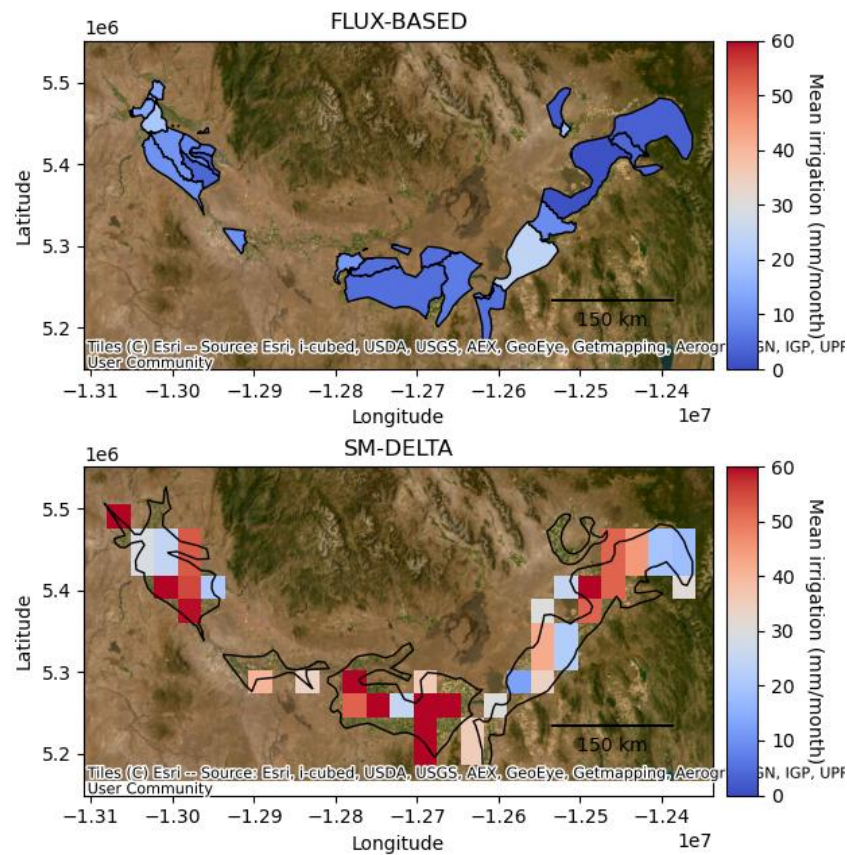


Figure 4.5: Map of irrigation retrieved with the FLUX-BASED approach (top) and with the SM-DELTA approach (bottom) over the Snake River Plain region.

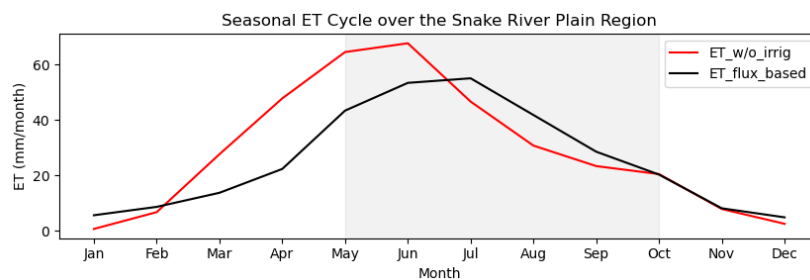


Figure 4.6: Seasonal cycle of $ET_{\text{FLUX-BASED}}$ (black line) and $ET_{\text{w/o_irrig}}$ (red line) computed over the period 2001-2020 for the Snake River Plain region.

Figure 4.7 shows the monthly $I_{\text{FLUX-BASED}}$ and $I_{\text{SM-DELTA}}$ obtained for the Snake River Plain region for the period 2004-2020. As for the California Valley region, $I_{\text{SM-DELTA}}$ shows more irrigation (217 mm/season and standard deviation of 41 mm/season) than $I_{\text{FLUX-BASED}}$ (39 mm/season and standard deviation of 19 mm/season), and is more consistent from one year to the next.

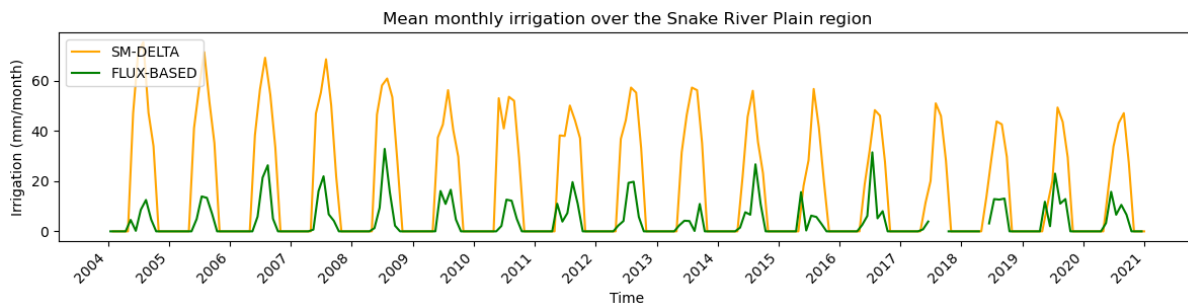


Figure 4.7: Monthly irrigation retrieved for the Snake River region using the FLUX-BASED approach (green line) and the SM-DELTA approach (yellow line).

4.2.3. Great Plains

Figure 4.8 shows the Great Plains region with $ET_{FLUX-BASED}$ (left) and $I_{SM-DELTA}$ (right). This region is more humid, has less irrigated surface area, and shows lower $I_{FLUX-BASED}$ and $I_{SM-DELTA}$ values than California Valley and Snake River Plain. Moreover, $I_{SM-DELTA}$ generates larger quantities of irrigation than $I_{FLUX-BASED}$, with values above 40 mm/month for the pixels with high percentage of area equipped for irrigation, while $I_{FLUX-BASED}$ is more homogeneous with values between 3 and 20 mm/month.

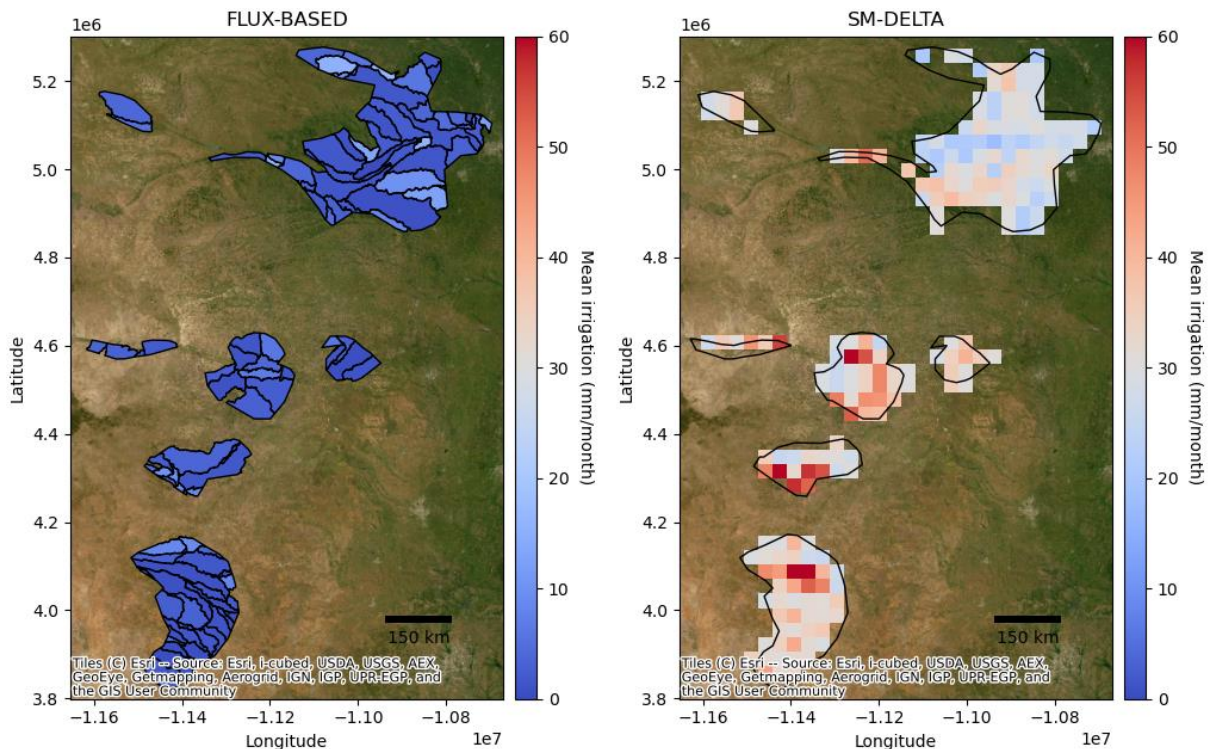


Figure 4.8: Map of irrigation retrieved with the FLUX-BASED approach (left) and with the SM-DELTA approach (right) over the Great Plains region.

The seasonal cycle (Figure 4.9) shows that $ET_{FLUX-BASED}$ is generally lower than ET_{w/o_irrig} . This suggests a difficulty for $ET_{FLUX-BASED}$ to detect the irrigation signal in this region. $I_{FLUX-BASED}$ is generated only in certain months when $ET_{FLUX-BASED}$ is very high and punctually exceeds ET_{w/o_irrig} .

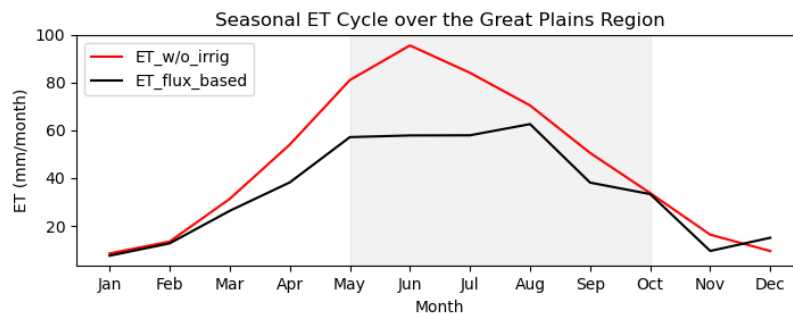


Figure 4.9: Seasonal cycle of $ET_{FLUX-BASED}$ (black line) and ET_{w/o_irrig} (red line) computed over the period 2001-2020 for the Great Plains region.

Figure 4.10 shows monthly $I_{FLUX-BASED}$ and $I_{SM-DELTA}$ retrieved over the Great Plains region. $I_{FLUX-BASED}$ is particularly low, with seasonal mean values of 16 mm/season (standard deviation of 12 mm/season). $I_{SM-DELTA}$ is also lower than in the other irrigated regions with seasonal mean values of 163 mm/season (standard deviation 34 mm/season).

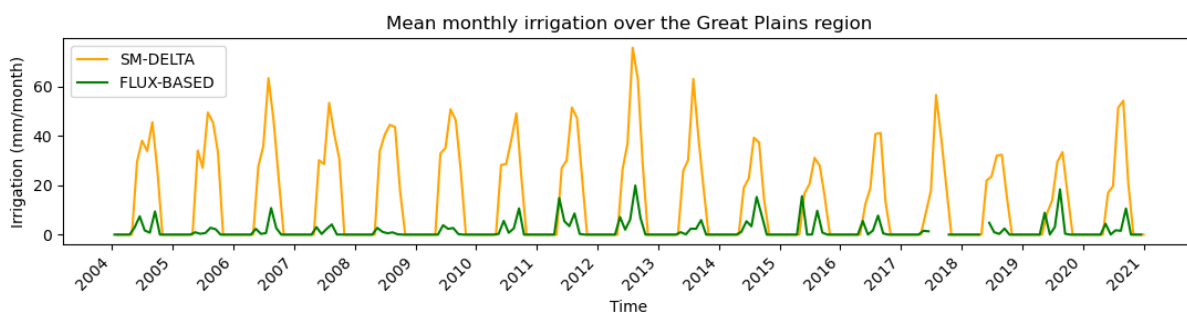


Figure 4.10: Monthly irrigation retrieved for the Great Plains region using the FLUX-BASED approach (green line) and the SM-DELTA approach (yellow line).

4.2.4. Mississippi floodplain

Figure 4.11 shows the Mississippi Floodplain region with $I_{FLUX-BASED}$ (left), and $I_{SM-DELTA}$ (right). This region is more humid than California Valley and Snake River Plain and has more irrigated surface than the Great Plains region (see Table 4.1).

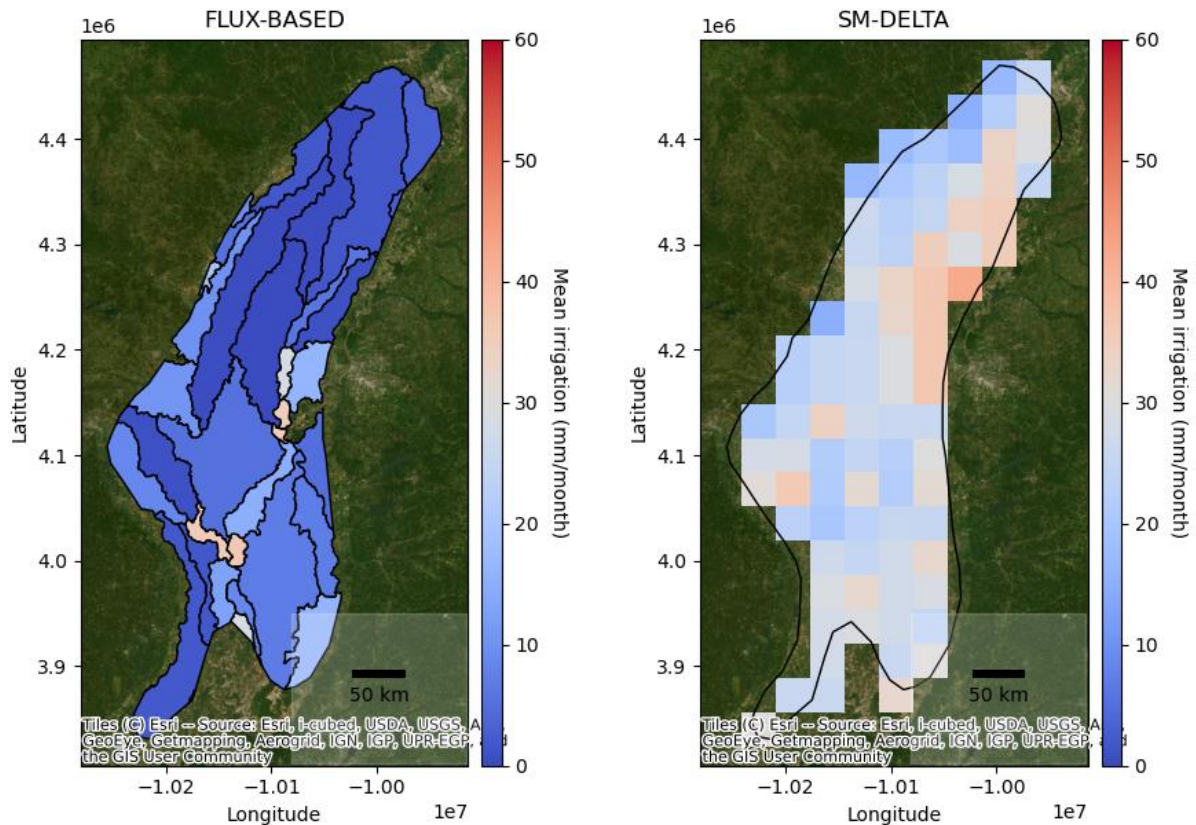


Figure 4.11: Map of irrigation retrieved with the FLUX-BASED approach (left) and with the SM-DELTA approach (right) over the Mississippi Floodplain region.

As for the California Valley, Snake River Plain, and Great Plains regions, $I_{SM-DELTA}$ generates larger irrigation quantities than $I_{FLUX-BASED}$, with values above 40 mm/month for pixels with higher percentage of area equipped for irrigation, while $I_{FLUX-BASED}$ is more homogeneous ranging from 3 to 20 mm/month.

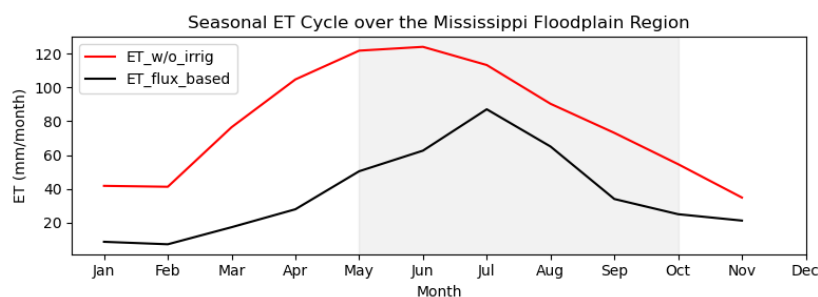


Figure 4.12: Seasonal cycle of $ET_{FLUX-BASED}$ (black line) and ET_{w/o_irrig} (red line) computed over the period 2001-2020 for the Mississippi Floodplain region.

Figure 4.13 shows monthly $I_{FLUX-BASED}$ and $I_{SM-DELTA}$ obtained for the Mississippi Floodplain region. $I_{FLUX-BASED}$ is particularly variable, with some years showing very little irrigation (e.g. 2005 to 2008) and others showing values relatively close to $I_{SM-DELTA}$ (e.g. 2009 or 2016). Over the Mississippi Floodplain region, $I_{FLUX-BASED}$ has

seasonal mean values of 28 mm/season (standard deviation 26 mm/season), and $I_{SM-DELTA}$ 134 mm/season (standard deviation 51 mm/season).

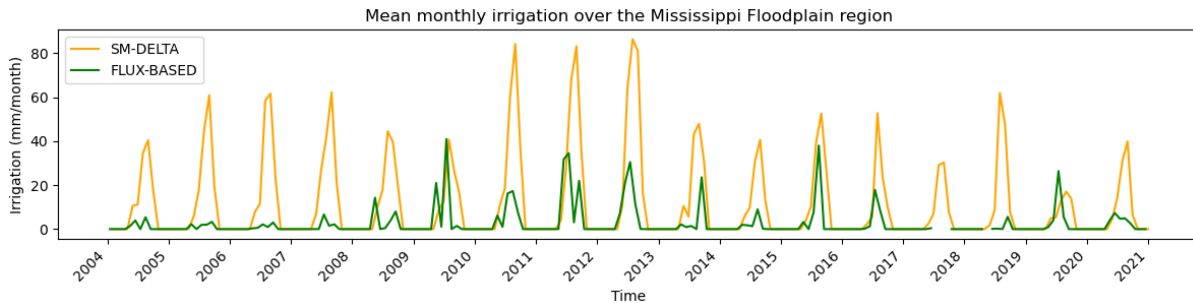


Figure 4.13: Monthly irrigation retrieved for the Mississippi Floodplain region using the FLUX-BASED (green line) and the SM-DELTA approach (yellow line).

4.2.5. Rainfed region

Figure 4.14 shows the rainfed region and the irrigation retrieved with the FLUX-BASED (left) and with SM-DELTA (right) approaches. It is interesting to observe that, on this humid and non-irrigated region, $I_{FLUX-BASED}$ and $I_{SM-DELTA}$ are in the same order of magnitude and show both low irrigation values and high homogeneity, in contrast to all four irrigated zones analyzed above. $I_{SM-DELTA}$ shows irrigation values around 15-20 mm/month and $I_{FLUX-BASED}$ shows irrigation values around 5 and 20 mm/month.

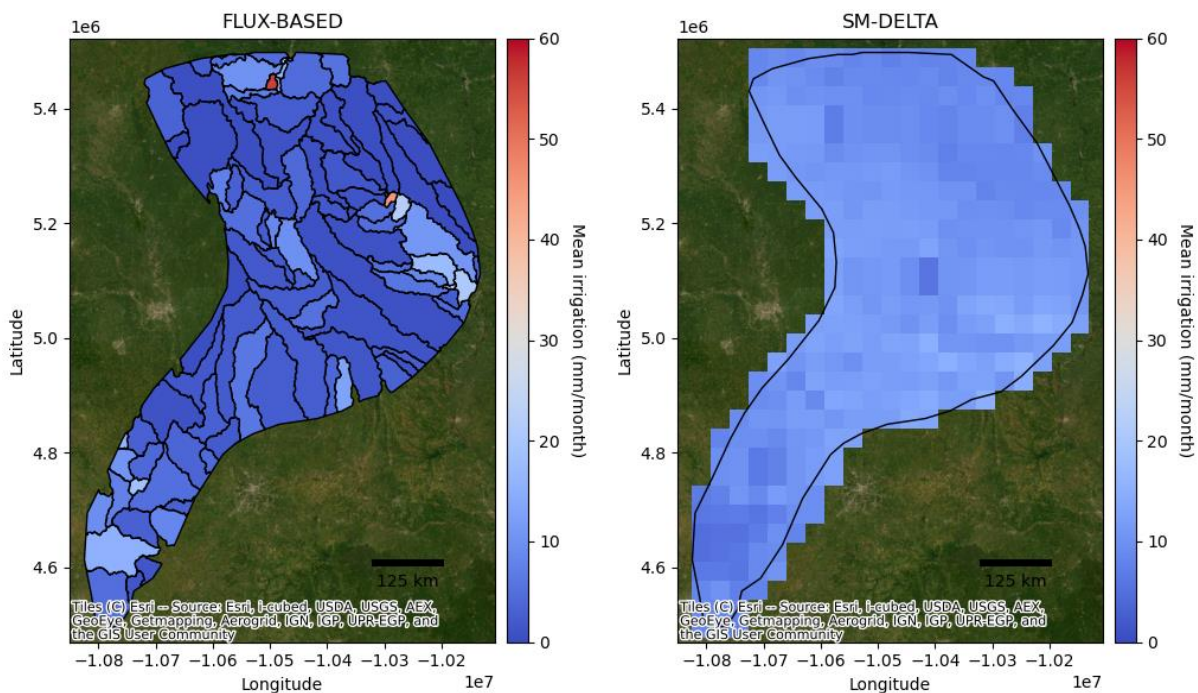


Figure 4.14: Map of irrigation retrieved with the FLUX-BASED approach (left) and with the SM-DELTA approach (right) over the Rainfed region.

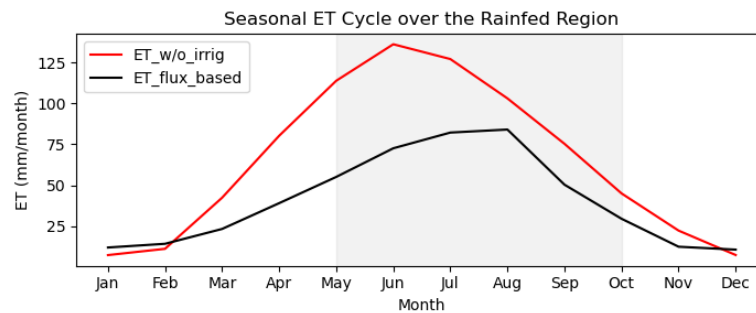


Figure 4.15: Seasonal cycle of $ET_{FLUX-BASED}$ (black line) and ET_{w/o_irrig} (red line) computed over the period 2001-2020 for the Rainfed region.

Figure 4.16 shows monthly $I_{FLUX-BASED}$ and $I_{SM-DELTA}$ obtained for the rainfed region. It is very interesting to note that the dynamics and quantities of irrigations are close between $I_{FLUX-BASED}$ and $I_{SM-DELTA}$, with for example both having low irrigations for the period 2005 to 2011 and higher irrigations for the years 2013 and 2014.

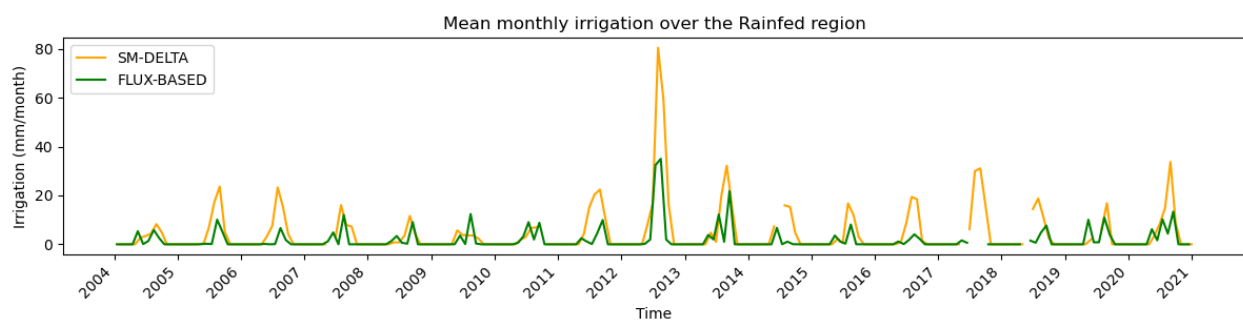


Figure 4.16: Monthly irrigation retrieved for the rainfed region using the FLUX-BASED approach (green line) and the SM-DELTA approach (yellow line)

4.3. Discussion

Figure 4.17 shows boxplots with annual irrigation quantities (between 2004 and 2020) for each of the five regions analyzed, obtained with the FLUX-BASED approach (blue boxplots) and the SM-DELTA approach (orange boxplots). As seen in Section 2, the SM-DELTA approach provides much higher irrigation quantities than the FLUX-BASED approach for the four irrigated regions. On the rainfed region, the annual retrieved irrigation is close between the two approaches.

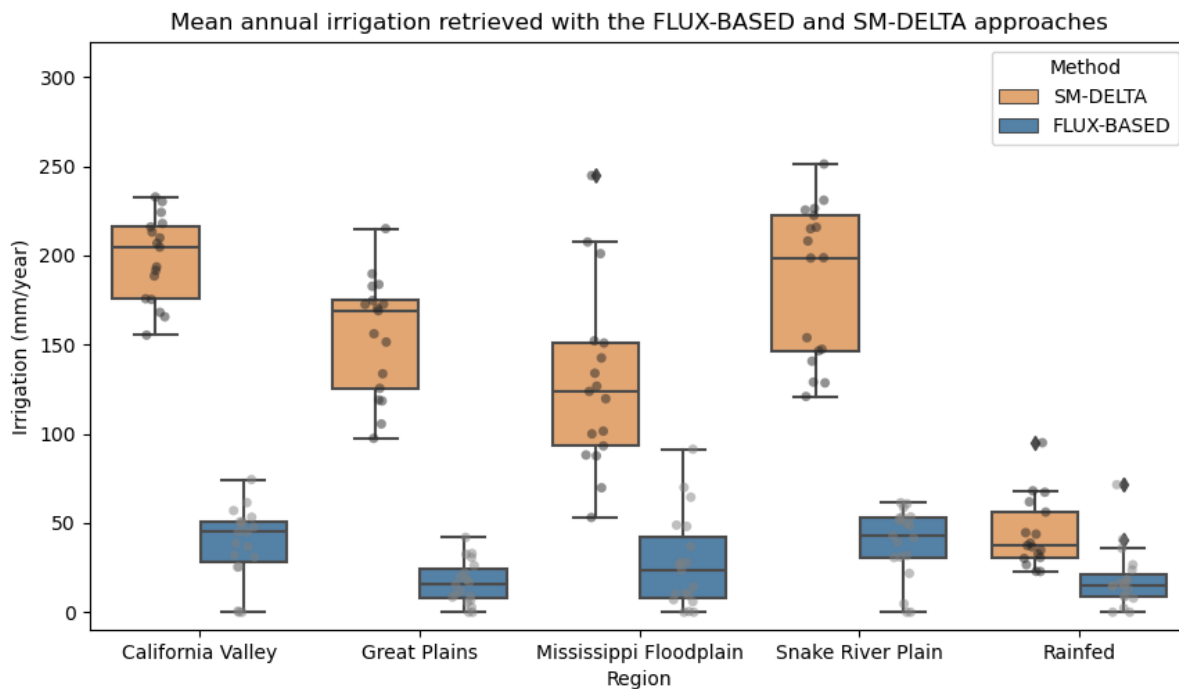


Figure 4.17: Boxplots showing the annual irrigation retrieved with the FLUX-BASED (blue boxplots) and the SM-DELTA approach (orange boxplots) for the period 2004-2020.

Two important elements arise from this analysis:

Firstly, the irrigation quantities retrieved with the FLUX-BASED approach are too low to realistically meet the water requirements of the crops grown in the four irrigated regions, considering the known irrigation practices, as opposed to the irrigation retrieved with the SM-DELTA approach. For example, in the California Valley region, the main crops are almonds, tomatoes, and grapes, which have water requirements of around 600–1200 mm per season (Allen et al., 1998), while annual rainfall is approximately 150–600 mm (California Department of Water Resources, 2013). An irrigation level of 50 mm/year, as retrieved with the FLUX-BASED approach, is too low to be consistent with known farmers' water needs. This also applies to the semi-arid Snake River Plain region, where potatoes, wheat, and sugar beets are predominant (Kelley and Olson et al., 2022) and where FLUX-BASED irrigation averages less than 50 mm/year and, for some years, is close to 0 mm/year. The same issue extends to the Great Plains and Mississippi Floodplain regions. Additionally, FLUX-BASED shows many months with values close to zero across the four irrigated regions, which is unrealistic.

Secondly, $I_{\text{FLUX-BASED}}$ is capable of detecting irrigation (albeit in insufficient quantities). On average, $I_{\text{FLUX-BASED}}$ shows more annual irrigation in the California Valley and Snake River Plain regions - the most intensively irrigated and with a semi-arid climate - than in the Great Plains and Mississippi Floodplain regions. More irrigation is also retrieved in the Mississippi Floodplain region than in the Great Plains region, which is consistent with the average percentage of surface area equipped for irrigation being higher for the Mississippi Floodplain region than in the Great Plains region (cf. Table 4.1). Furthermore, the annual irrigation values retrieved using the FLUX-BASED approach for the rainfed region are the lowest of the five regions.

4.4. Recommendations and conclusion

The analysis of the irrigation retrieved with the FLUX-BASED approach on the five CONUS regions (California Valley, Snake River Plain, Mississippi Floodplain, Great Plains, and Rainfed), and the comparison with the irrigation obtained with the SM-DELTA approach, allows us to draw the following conclusions:

1. The FLUX-BASED approach can detect irrigation, and retrieve larger quantities over the most irrigated regions (California Valley and Snake River Plain) than in the less irrigated ones (Great Plains and Mississippi Floodplain).
2. It fails to retrieve sufficient irrigation quantities in comparison with the SM-DELTA approach and the climate and crop water requirements of different regions. We hypothesize that this is due to the very coarse spatial resolution of the Total Water Storage data, the only variable including irrigation used in the FLUX-BASED approach. Even if the FLUX-BASED approach is able to detect irrigation, the irrigation signal is “diluted” in pixels much larger than the scale at which irrigation occurs.

Based on these conclusions, we recommend that the FLUX-BASED approach should not be considered as a candidate contributing to the development of a CCI AWU ECV.

5. Validation of the model-observation integration approach

5.1. Introduction

AWU plays a critical role in the terrestrial water cycle, accounting for 84-90% of the global freshwater consumption (McDermid et al., 2023). Despite this importance, this human influence on land water distribution is often poorly parameterized in regional and large-scale land surface models (LSM). One challenge is that the capability to simulate irrigation relies on input irrigated area maps, which are frequently outdated or static. An example is given by the Global Rainfed Irrigated and Paddy Croplands dataset which refers to the year 2005 (GRIPC; Salmon et al., 2015) and that was used in recent studies to derive irrigation estimates through LSM (Modanesi et al., 2022; Busschaert et al., 2023; De Lannoy et al., 2024). Another issue is that irrigation parameterization often depends on spatially uniform, user-defined parameters, limiting the model's ability to estimate reliable irrigation quantities.

In the proposal stage, a coarse-scale data assimilation framework was proposed where first observation-based forcings (ERA5 reanalysis) are used to steer long-term hindcasts, and next SM retrievals would be assimilated without or with minimal bias correction. However, an analysis of the differences between model- and satellite-based SSM (Section 5.2) revealed a complexity in the bias patterns that prevented a good prospect for a traditional DA application. It is important to note that, given the current limitations of using DA filters to update soil moisture as described in Busschaert et al. (2024), the observations are not directly assimilated but contrasted to the model to detect irrigation instead, and provide irrigation maps. The latter could constrain modeled irrigation estimates in future work.

In this context, the PVASR report discusses: (1) the results and validation analysis of irrigation detection algorithms applied to coarse-resolution satellite soil moisture products to create maps of irrigation fraction used as input into LSMs; (2) validation of long-term irrigation datasets derived from an irrigation module within a LSM, using various deterministic runs to test different parameterizations; and (3) visualisation of results from ensemble perturbation LSM runs aimed at estimating irrigation uncertainty. Section 5.2 - Irrigation Detection - addresses item (1), while Section 5.3 - Irrigation Quantification - covers items (2) and (3).

5.2. Irrigation detection

Two independent approaches were explored to detect irrigation by comparing SMOS surface soil moisture (SSM) satellite retrievals with Noah-MP estimated SSM over CONUS between January 2010 and March 2023. The estimated irrigated fraction is evaluated with the Landsat-derived irrigated fraction map (Teluguntla et al., 2023; Figure 5.1) for both approaches below (Sections 5.2.1 and 5.2.2). The two approaches are compared in Section 5.2.3.

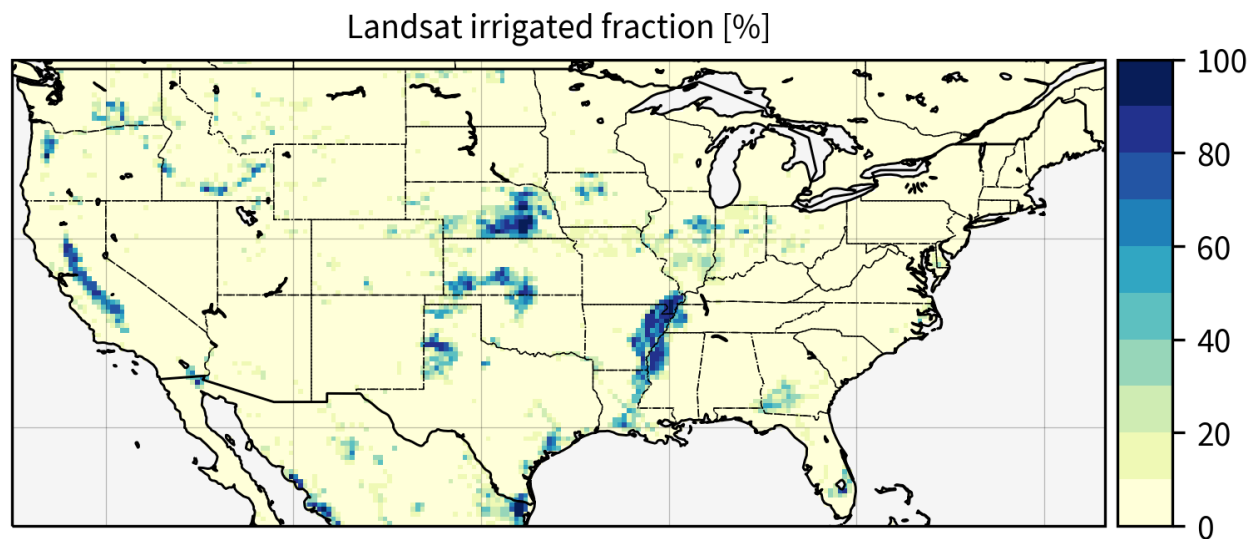


Figure 5.1: Landsat-derived irrigated fraction, to be used as reference in the evaluation.

5.2.1. Approach 1: relative bias

Table 5.1 shows the confusion matrix comparing the estimates of the irrigated fraction (rows) and the reference Landsat-derived irrigated fraction (columns) over the study domain, each divided into three categories: little or no irrigation (irrigated fraction < 20%), some irrigation (20% < irrigated fraction < 80%) and heavily irrigated (irrigated fraction > 80%). The cells show the number of grid cells in each category: for those in the diagonal, our estimates correspond to the reference, while estimates are poorer as they are further away from the diagonal. The grid cells corresponding to the different categories are visualised in the map of Figure 5.2, where we simplified the stratification as binary classification by defining “irrigated” as an irrigation fraction larger than 20%, and “non-irrigated” as an irrigation fraction smaller than 20%. A true positive (TP) then corresponds to an irrigated grid cell which is correctly classified by our estimation approach as such; a true negative (TN) is a non-irrigated grid cell which is correctly classified. A false positive (FP) is a grid cell which is not irrigated but classified as irrigated, while a false negative (FN) is an irrigated grid cell which was classified non-irrigated.

		Landsat-derived irrigated fraction (reference)			sum
		irri < 20%	20% < irri < 80%	irri > 80%	
Irrigated fraction estimates	irri < 20%	4361	445	27	4833
	20% < irri < 80%	259	274	20	553
	irri > 80%	14	50	42	106
sum		4634	769	89	5492

Table 5.1. Confusion matrix comparing the estimates of irrigated fraction with the Landsat-derived irrigated fraction. Only grid cells with nonzero cropland fraction and with coverage of the SMOS retrievals are considered. The colours indicate

the true negatives (TN; light blue), true positives (TP; dark blue), false negatives (FN; dark red) and false positives (FP; light red).

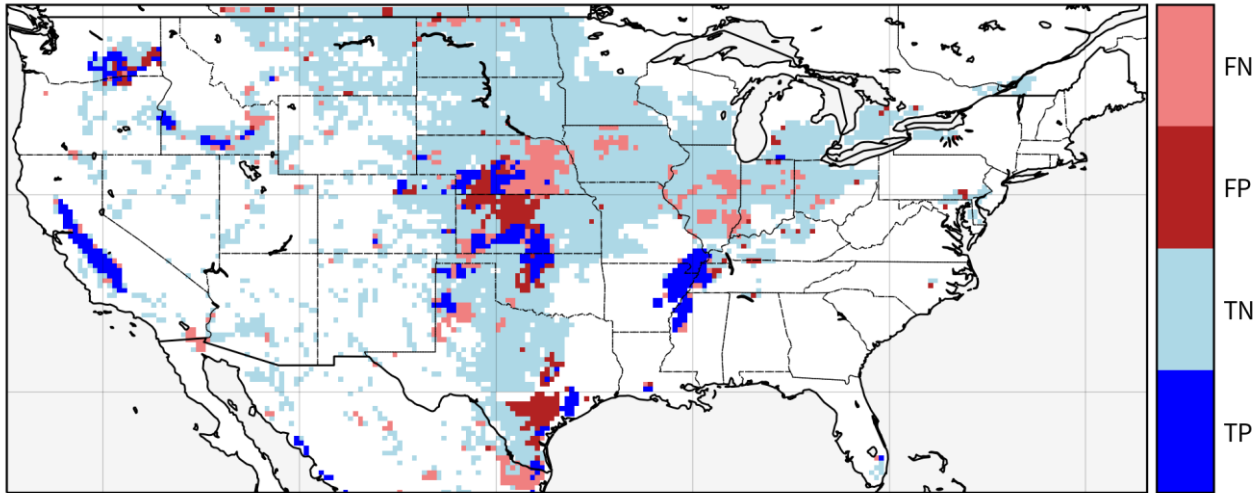


Figure 5.2: Evaluation of the relative bias approach in terms of true positives (TP), true negatives (TN), false positives (FP), and false negatives (FN), as defined in the main text.

The map shows croplands in the higher latitudes are correctly classified as non-irrigated, while our approach is shown to detect irrigation in croplands of, for example, California and the Mississippi basin accurately. Irrigation in the east of Nebraska proved difficult to estimate with the relative bias approach, illustrated by the many false negatives there. Northern Nebraska and southern Texas are the main regions with false positives, i.e., estimated irrigation by our approach over grid cells that are not irrigated according to the Landsat-based reference. We discuss the quantitative evaluation of the domain as a whole below.

The true positive rate TPR measures the proportion of actual positives that are correctly identified (larger is better):

$$TPR = TP / (TP + FN) = 45.0\%.$$

The false positive rate FPR measures the proportion of actual negatives that are incorrectly classified as positive (smaller is better):

$$FPR = FP / (FP + TN) = 5.9\%.$$

For imbalanced classes such as is the case here (“non-irrigated” is the dominant class), the Matthews Correlation Coefficient:

$$MCC = \frac{TP \times TN - FP \times FN}{\sqrt{(TP + FP)(TP + FN)(TN + FP)(TN + FN)}}$$

is an appropriate metric to assess the performance. It takes values from -1 to 1, with values larger than 0 indicating a classification that performs better than random (and 1 a perfect classification). Its value is 0.44 for our approach.

Finally, we can also look at the values on the diagonal in the confusion matrix Table 5.1: 4677 grid cells are on the diagonal, which is 85.2% of the total. Only 41 grid cells are in the top right and bottom left corner,

indicating an estimated strong irrigation over non-irrigated grid cells (or vice versa); this is only 0.7% of the total.

5.2.2. Approach 2: multiresolution analysis to detect irrigation and comparison with bias approach

The application of the wavelet analysis requires full time series for both Noah-MP and SMOS time series. While we interpolated data to fill gaps up to 5 days given the significant masking of SMOS over high latitudes and complex terrain not all pixels could be processed. We set the limit pixels where SMOS was characterised by at least 70% of valid data to avoid alterations of the spectrum due to interpolation. Furthermore the wavelet approach was applied only to pixels characterised by 100% crop and did not consider pixels with mixed land cover. This brought to a different number of pixels with the method based on relative bias.

The classification of the synthetic data produced excellent results, with an AUC of 0.84. The optimal number of predictors (Nest) was 1000, and the maximum number of features (max_features) was set to 2. The classifier applied to the SMOS time series produced the confusion matrix shown in Figure 5.3, with a True Positive Rate (TPR) of 48.2%, a False Positive Rate (FPR) of 9.85%, and a Matthews Correlation Coefficient (MCC) of 0.4250. Since a single threshold was used for classification, the ROC curve collapses to a single point (TPR = 48.2%, FPR = 9.8%), yielding an AUC of approximately 0.692, which suggests moderate to good detection performance.

While the classification presented here uses fewer pixels compared to the approach in Section 5.2.1 (i.e., the relative bias approach), direct comparisons between the two are not entirely appropriate. Nevertheless, the MCC values are similar. The wavelet-based approach, although applied to a smaller sample size over non-irrigated areas, appears slightly penalized in terms of detection performance for non-irrigated pixels. However, given the broader coverage of non-irrigated pixels across the central U.S. (CONUS), the similarity in true negative detection suggests comparable performance in identifying areas of no irrigation.

The distribution of true positives (TP), true negatives (TN), false positives (FP), and false negatives (FN) is shown in Figure 5.4, which mirrors the pattern seen in Figure 5.3, albeit with a smaller number of pixels. Both approaches correctly identified the most intensively irrigated areas but equally failed to detect irrigation in eastern Nebraska. Approach 1 (relative bias) is more conservative, yielding a lower TPR than Approach 2 (multiresolution analysis), but also a lower FPR. The MCCs for both approaches are positive, indicating that both methods perform better than random classification.

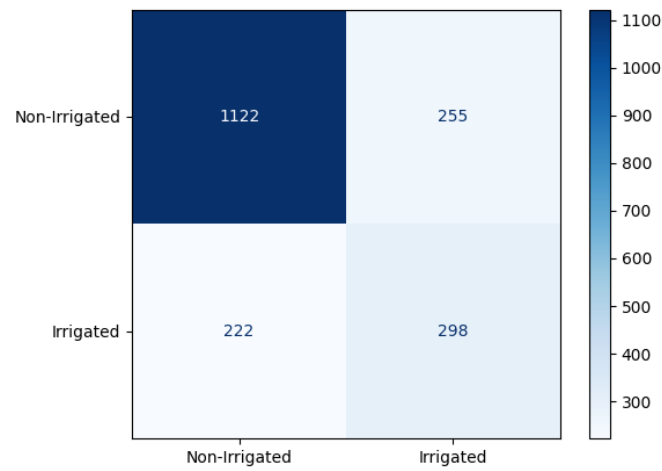
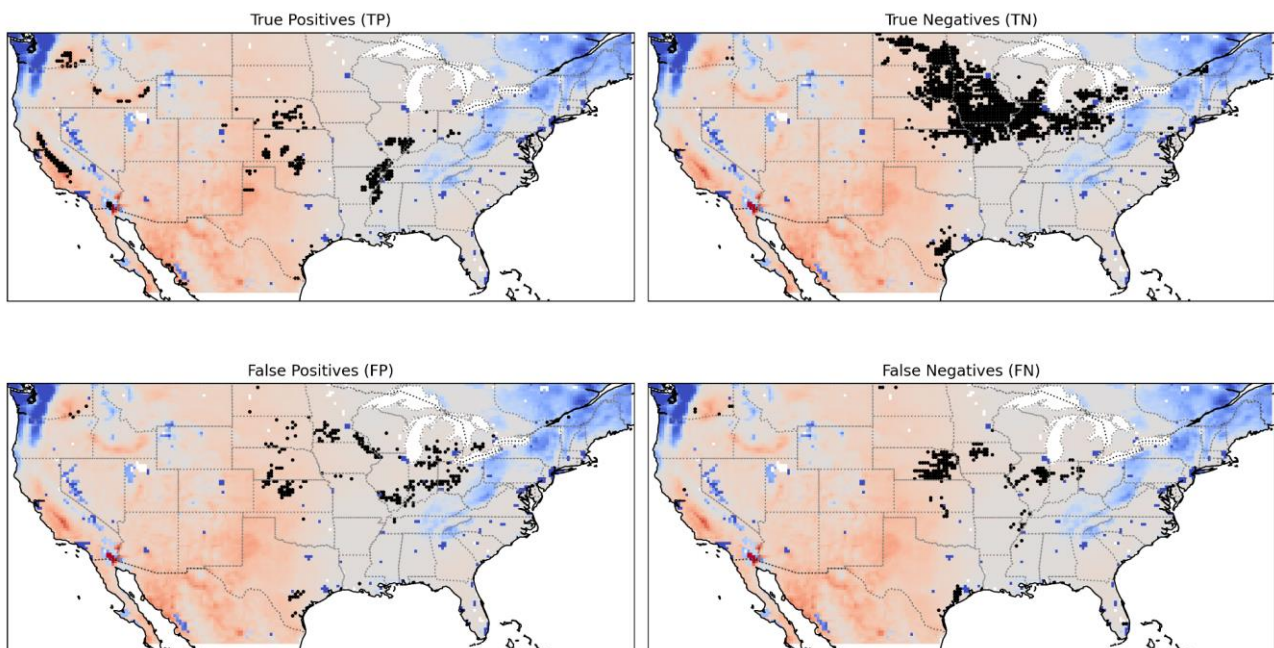
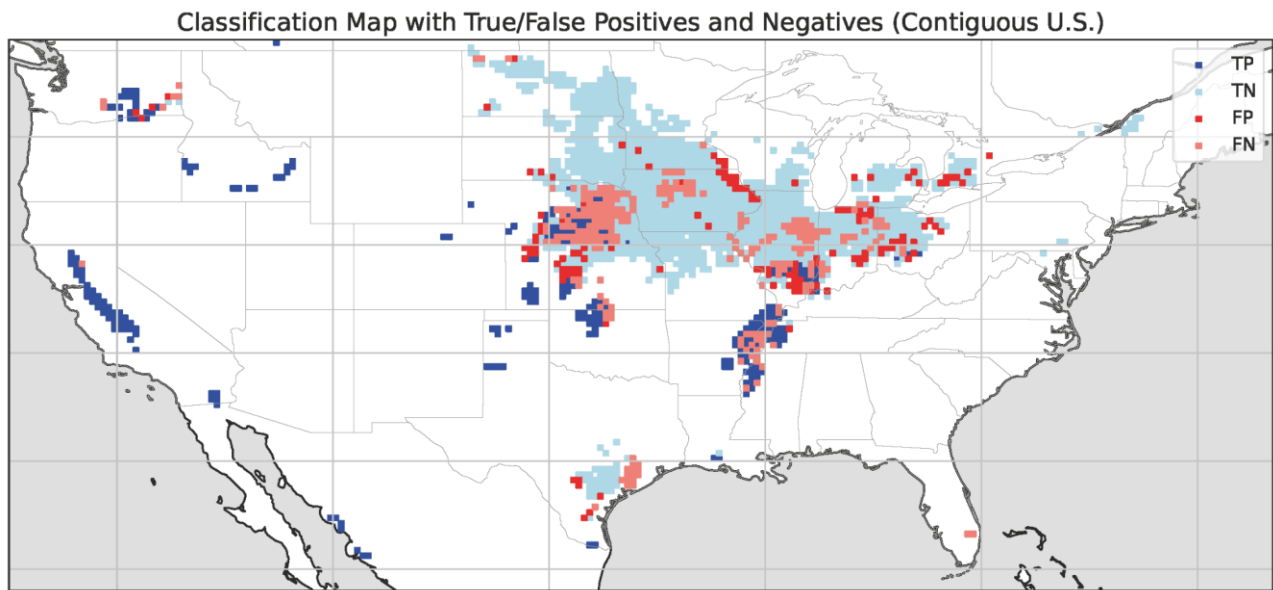


Figure 5.3: Confusion matrix obtained via the Random forest classifier, applying the classification to Noah-MP and SMOS time series. The evaluation in terms of true positives (TP), true negatives (TN), false positives (FP), and false negatives (FN), as defined in the main text for the relative bias approach.



(a)



(b)

Figure 5.4: (a) Distribution true positives (TP), true negatives (TN), false positives (FP), and false negatives (FN) over CONUS using SMOS soil moisture and wavelet analysis. (b) same as (a) but with color consistency with the relative bias method.

Figure 5.5 reports the final classification map with underlying aridity index showing a distribution of irrigated areas very similar to the data reported in literature thus identifying irrigation in California, north western and Central CONUS.

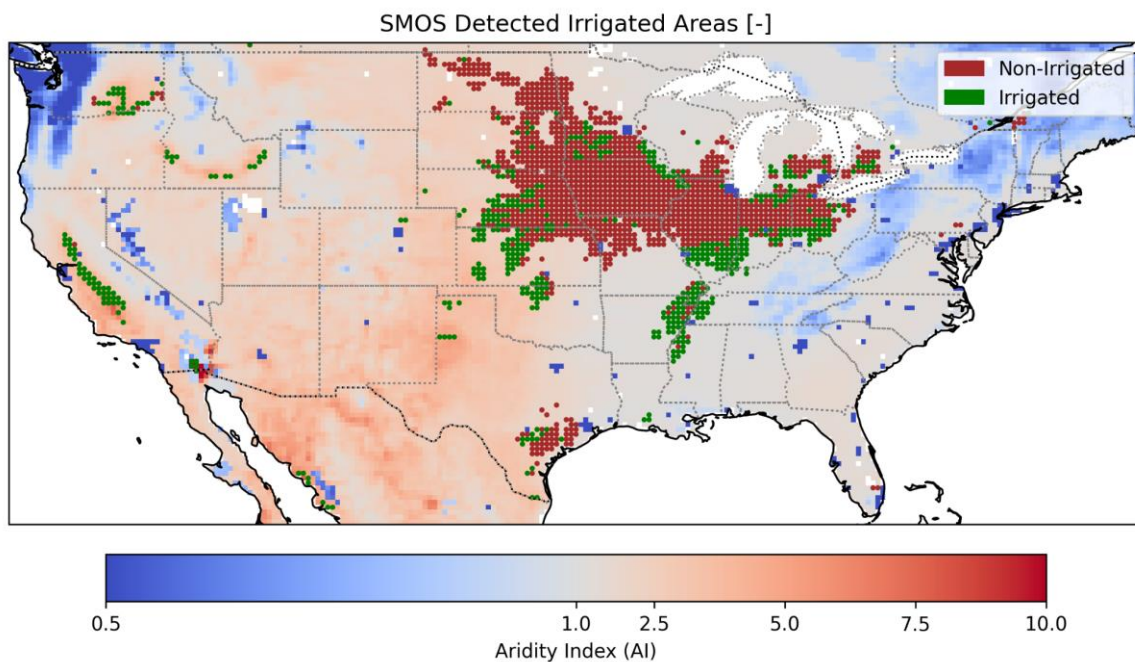


Figure 5.5: Classification of irrigated vs non irrigated pixels over CONUS using SMOS soil moisture and wavelet analysis.

In summary both approaches provide similar results with the relative bias approach yielding a bit better scores in the current configuration. Given the number of uncertainties in the satellite soil moisture

observations and the simulations, the outcome of this analysis can be considered satisfactory. Future works shall focus on the identification of irrigation in time. A paper is currently in preparation for the approaches used here.

5.3. Irrigation quantification

5.3.1. Deterministic runs

Deterministic experiments were conducted using the Noah-MP LSM version 4.0.1, coupled with a sprinkler irrigation scheme (Ozdogan et al., 2010), and running within the Land Information System Framework (LIS; Kumar et al., 2006; Peters-Lidard et al., 2007). The model was set up across the Contiguous United States (CONUS) in order to estimate long-term agricultural water use (AWU) for a period ranging from January 2010 to March 2023. Table 1 provides an overview of the various experiments carried out (detailed in Deliverable 3 - ATBD), which used different parameterizations by varying the growing season (when irrigation is allowed) and the irrigation threshold parameter (Th_{irr}) applied to root zone soil moisture availability (MA), as defined in the ATBD.

For the growing season parameterization, we tested the following approaches:

- A climatological Greenness Vegetation Fraction (GVF) approach;
- Year-round irrigation (YR);
- A dynamic vegetation approach (DYNVEG), which applies a threshold to the Leaf Area Index (LAI) simulated by the model (irrigation is allowed when $LAI > 1$; Modanesi et al., 2022).

A TILING land cover option was also tested. The TILING approach incorporates multiple land cover types within a single 25 km spatial resolution grid cell, scaling irrigation based on the percentage of cropland in a single grid cell and on the pixel-based irrigation fraction map.

Table 5.2. The table provides an overview of all deterministic runs conducted, detailing general information on the LSM and forcings as well as the various growing season options, Th_{irr} values, and the activation or not of a tiling option.

EXPERIMENTS (Time span 2010-2022)					
LSM	IRRIGATION SCHEME	FORCING	GROWING SEASON	TILING	Th_{irr}
Noah-MPv.4.0.1 (Niu et al., 2011)	Sprinkler Irrigation scheme (Ozdogan et al., 2010)	ERA 5 (Hersbach et al., 2020)	GVF	not applied	0.35
				not applied	0.45
				not applied	0.55
				not applied	0.65
				applied	0.45

			YR	not applied	0.45
				not applied	0.65
			DYNVEG	not applied	0.45

Data used for the evaluation are derived by the 2013 and 2018 Farm and Ranch Irrigation Survey (FRIS) produced by the National Agricultural Statistics Service (NASS) of the United States Department of Agriculture (USDA). The reader can refer to Deliverable 2 for more detailed information. The database consists of country-aggregated information about irrigation water applications in km^3/year , which were compared to the results obtained from the model simulations. Figure 5.6 shows an example map of the benchmark irrigation data in km^3/year over CONUS.

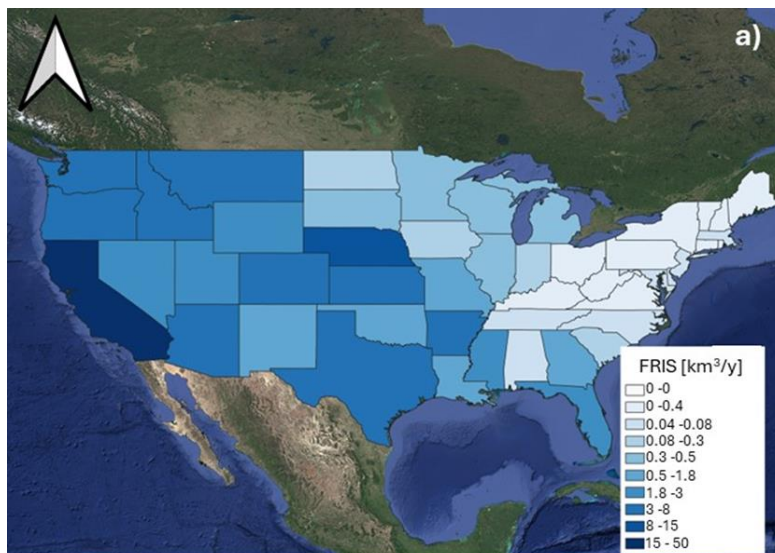


Figure 5.6: benchmark irrigation water volume aggregated at country-level and obtained from the FRIS dataset. Irrigation data is provided in km^3/year .

The irrigation masks used for evaluation differ between the NO-TILING and TILING runs. Both options are based on the LANDSAT-derived map of irrigated areas (Teluguntla et al., 2023). However, irrigation is applied under specific conditions: 1) in the NO-TILING option, irrigation is only possible where the land cover is classified as cropland and the irrigation fraction is greater than 0; 2) in the TILING option, which enables the classification of pixels with multiple land cover types, irrigation can be applied when the cropland percentage is greater than 0 and the irrigation fraction is also greater than 0. Figure 5.7c presents the LANDSAT-based irrigation fraction map (Figure 5.7c), along with the irrigation mask for the NO-TILING (Figure 5.7a) and the TILING option (Figure 5.7b). Consequently, in the NO-TILING option, only 35 out of 48 states are irrigated and included in the evaluation, whereas in the TILING option, irrigation is validated across all 48 states.

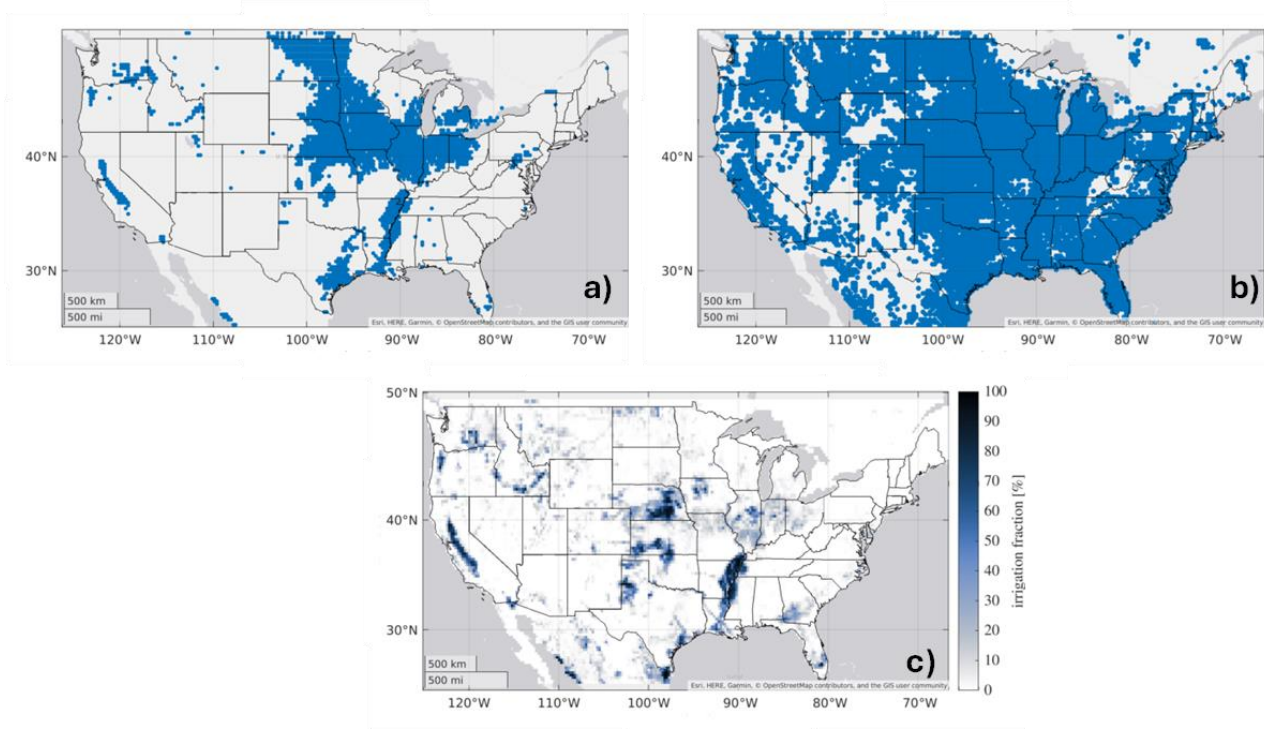


Figure 5.7: Maps of: a) irrigated areas mask used for the evaluation in NO-TILING mode; b) irrigated areas mask used for the evaluation in TILING MODE; c) the LANDSAT-based irrigation fraction provided as model input.

A first set of experiments was conducted for the NO-TILING option using the GVF growing season and varying the Th_{irr} parameter with values of 0.35, 0.45, 0.55, and 0.65. The maps in Figure 5.8 show pixel-level information on annual cumulative irrigation quantities obtained for each threshold. Mean irrigation over the entire CONUS ranges from 73.3 mm/year with $Th_{irr} = 0.35$, to 131 mm/year with $Th_{irr} = 0.45$, 194 mm/year with $Th_{irr} = 0.55$, and up to 269 mm/year with $Th_{irr} = 0.65$. Notably, irrigation seems to increase more with higher thresholds. Th_{irr} is applied to moisture availability and if Th_{irr} increases, irrigation is applied even at higher latitudes, which generally have wetter moisture conditions.

To evaluate these experiments, irrigation was converted from mm/year at the pixel scale to km^3/year at the state level, considering only pixels within the irrigation mask. Figure 5.9 presents the results as scatterplots (each point representing a state), comparing benchmark irrigation (x-axis) to simulated irrigation (y-axis). The rows correspond to the two reference years, 2013 and 2018, respectively, while the columns represent different Th_{irr} values, starting from 0.35 (Figures 5.9a and 5.9e) up to 0.65 (Figures 5.9d and 5.9h). Scores used for evaluation include Bias, a normalised root mean squared difference (RMNSD; normalised based on the mean observed irrigation), which provides a measure of the relative error, and spatial Pearson correlation (R). Statistical scores are shown in the boxes within each scatterplot. The number of states with non-zero irrigation (N_p) is indicated in each plot title, along with the total number of states used for evaluation (35) shown in parentheses. Results highlight that lower Th_{irr} yield better performance scores. For example, in 2013, a Th_{irr} value of 0.35 (Figure 5.9a) achieves a spatial correlation (R) of 0.62 and an RMNSD of 1.51. In contrast, the highest threshold, $Th_{irr} = 0.65$ (Figure 5.9d), shows weaker performance, with a spatial R value of 0.57 and a higher RMNSD of 4.87. The substantial overestimation is further reflected by a bias of 8.02 km^3/year . This finding aligns with the 2013 irrigation maps (Figure 5.8), where the $Th_{irr} = 0.65$ threshold results in significantly higher irrigation values (269 mm/year) compared to $Th_{irr} = 0.35$ (73.3 mm/year).

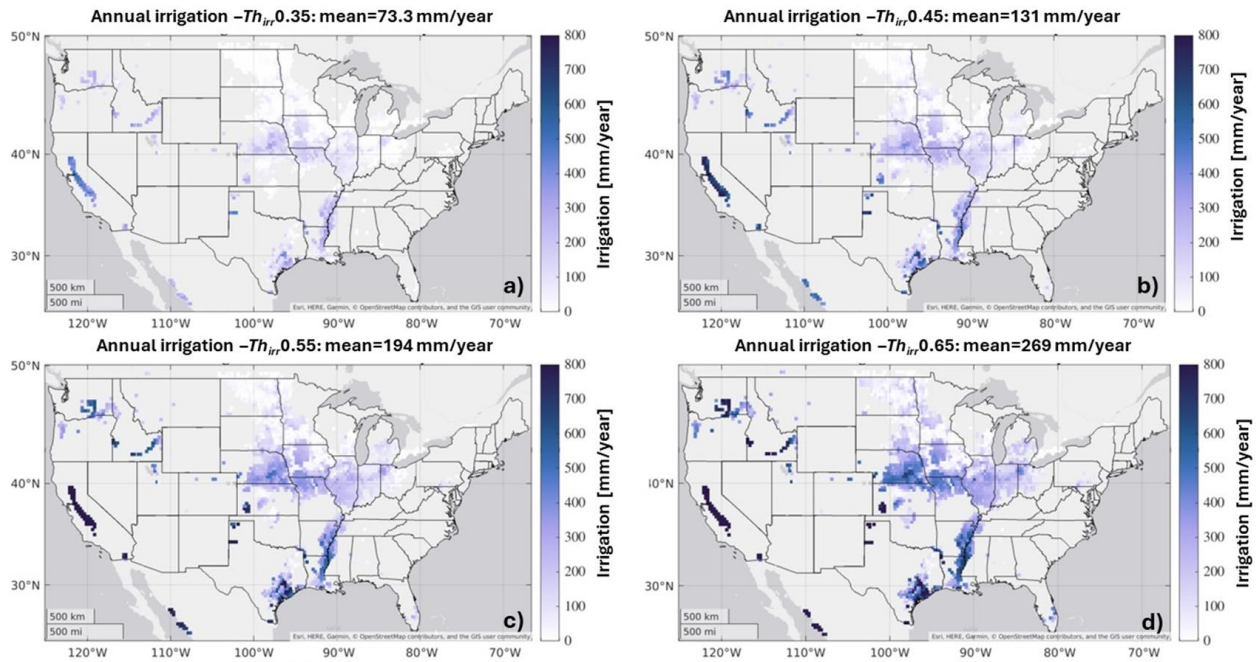


Figure 5.8: Annual irrigation maps in mm/year obtained using the NO-TILING option, the GVF growing season and Th_{irr} values equal to : a) 0.35; b) 0.45; c) 0.55; and d) 0.65. Mean spatial values of irrigation for each option are reported in the titles. The maps refer to the year 2013.

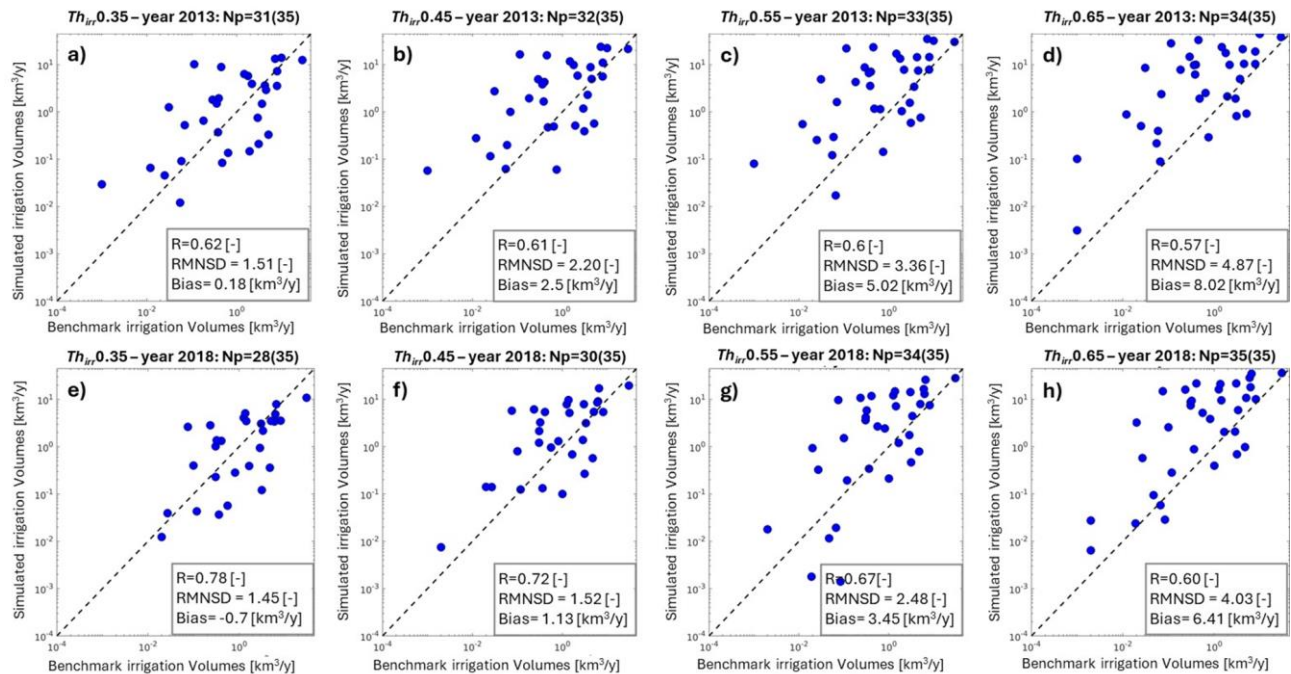


Figure 5.9: Scatterplots comparing benchmark irrigation volumes (km^3/year) with simulated volumes at the state level (each point represents a state). Plots (a) through (d) display results for 2013, with varying Th_{irr} values: (a) 0.35, (b) 0.45, (c) 0.55, and (d) 0.65. Similarly, plots (e) through (h) show results for 2018, with Th_{irr} values of (e) 0.35, (f) 0.45, (g) 0.55, and (h) 0.65. The value “Np” in each title represents the number of states with non-zero irrigation, while the value in parentheses indicates the total number of states used in the evaluation. Statistical scores (R, RMNSD, and bias) are presented in each plot's box. Note that the scatterplots are displayed on a logarithmic scale to improve visualisation.

The results demonstrate a higher performance for 2018, with an R value of 0.78 and a bias of -0.7 km³/year when using a Th_{irr} of 0.35. However, this threshold limits irrigation to only 28 of the 35 states when compared to the benchmark, which raises concerns about its applicability. While the $Th_{irr} = 0.35$ threshold yields better scores than other thresholds, it excludes a substantial number of states from the irrigation simulations. This analysis suggests that a Th_{irr} of 0.45 may offer a more balanced approach, optimizing statistical performance while minimizing possible underestimation in benchmark irrigation data.

With Th_{irr} set to 0.45, two additional experiments were conducted within the NO-TILING option using the YR and the DYNVEG growing season, in order to identify the most performing parameterization. Figure 5.10 presents maps of annual cumulative irrigation quantities for 2013, obtained using $Th_{irr} = 0.45$ for the YR growing season (Figure 5.10a) and for the DYNVEG growing season (Figure 5.10b). As anticipated, when comparing Figure 5.10a to the equivalent maps from the GVF growing season option (Figure 5.8b), the total annual irrigation amount increases. This increase is due to the fact that irrigation is permitted year-round, and in drier regions (e.g., California), moisture availability frequently drops below the Th_{irr} threshold even during winter, resulting in greater irrigation needs.

Notably, the DYNVEG option yields the highest irrigation quantities, reaching a spatial average of 151 mm/year (Figure 5.10b). This outcome is driven by two key factors: 1) in specific regions, such as California and Mississippi, the climatology of the simulated LAI consistently remains above 1, allowing for year-round irrigation; 2) the irrigation amounts are further influenced by the GVF through the following equation:

$$RZ = RZ_{max} * GVF \quad (1)$$

where RZ_{max} is the maximum rooting depth. In the GVF growing season option GVF is set as the GVF_{max} derived by the climatological GVF maps while in the DYNVEG option the GVF is computed based on the dynamic LAI and using the methodology outlined in Fang et al. (2018). Varying the root zone depth also varies the amount of water applied; the reader can refer to Deliverable 3 for additional details. This difference in the GVF justifies the different amount of water between DYNVEG and the other options.

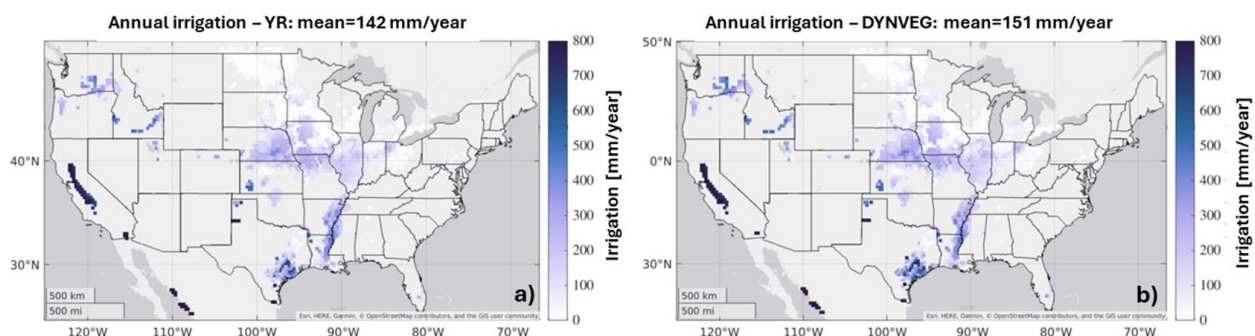


Figure 5.10: Annual irrigation maps in mm/year obtained using the NO-TILING option and Th_{irr} value equal to 0.45 considering: a) the YR growing season option; and b) the DYNVEG growing season option. Averaged spatial values of irrigation are reported in the titles. The maps refer to the year 2013.

Figure 5.3.6 presents an evaluation of the simulation results, similar to Figure 5.3.4, by comparing scatterplots of benchmark irrigation against simulated irrigation volumes (in km³/year). The comparison includes the GVF growing season option (Figures 5.11a and 5.11d for 2013 and 2018, respectively), the YR option (Figures 5.11b and 5.11e for 2013 and 2018, respectively), and the DYNVEG option (Figures 5.11c and 5.11f for 2013 and 2018, respectively), with Th_{irr} held constant at 0.45.

In terms of spatial R, the YR option yields the best results, achieving values of 0.65 versus 0.61 for GVF in 2013, and 0.75 versus 0.72 for GVF in 2018. However, for both 2013 and 2018, the GVF growing season option provides the highest scores in terms of RMNSD and Bias. Notably, in 2018, the Bias is minimized to 1.13 km³/year with GVF, whereas it reaches 1.7 km³/year with the DYNVEG option. Overall, the differences between GVF and YR performance are relatively minor, whereas the DYNVEG option exhibits a tendency toward higher overestimation.

Based on the results obtained for the NO-TILING experiments, we proceeded with the GVF growing season option and a Th_{irr} of 0.45 in the subsequent TILING experiment. Figure 5.12 displays the results as annual irrigation maps (mm/year), showing an increase in the number of irrigated pixels compared to Figures 5.10 and 5.8. These maps capture irrigation activity across a broader range of states, including Arizona, Wyoming, Nevada, and Massachusetts, along with many others across the CONUS. The lower spatial averaged annual irrigation can be attributed to the larger number of zero-irrigation pixels and the division of each pixel into multiple land cover types, reducing the percentage of cropland at the 25 km pixel-scale. In terms of irrigated pixels, also referring to the LANDSAT-based irrigation fraction map (Figure 5.7c) the TILING irrigation amounts map is more reliable as compared to the NO-TILING option. When compared to the LANDSAT-based irrigation fraction map (Figure 5.7c), the TILING map provides a more accurate representation of the irrigated pixels than the NO-TILING option. Lower irrigation amounts in states like Nevada, Arizona, and New Mexico—despite the presence of the TILING—reflect the lower irrigation fraction in these areas, as indicated by the LANDSAT dataset, compared to high-irrigation states like California, Mississippi, Arkansas, and Louisiana.

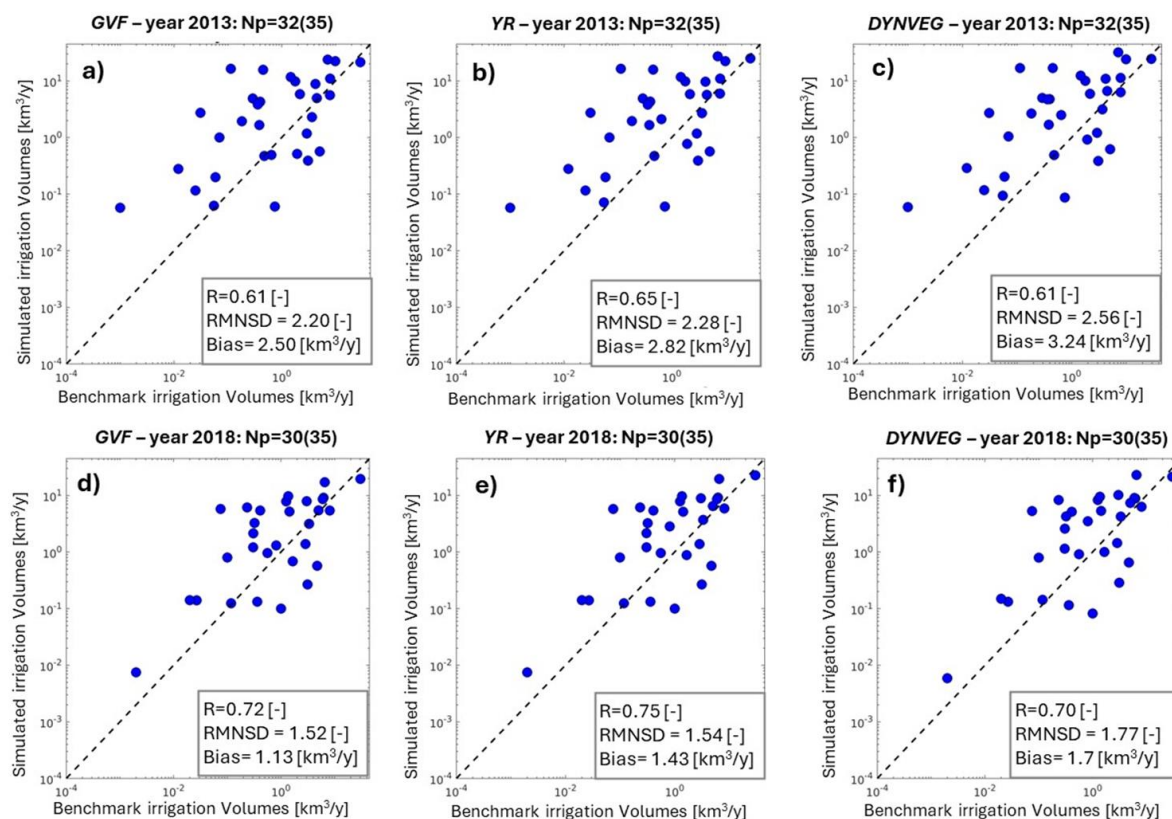


Figure 5.11: Scatterplots comparing benchmark irrigation volumes (km³/year) with simulated volumes at the state level (each point represents a state). Plots a) through c) display results for 2013, with varying growing season options: a) GVF; b) YR; c) DYNVEG. Plots d) through f) display results for 2018, with varying growing season options: d) GVF; e) YR; f) DYNVEG. The value “Np” in each title represents the number of states with non-zero irrigation, while the value

in parentheses indicates the total number of states used in the evaluation. Statistical scores (R, RMNSD, and bias) are presented in each plot's box. Note that the scatterplots are displayed on a logarithmic scale to improve visualization.

The Th_{irr} is kept constant to a value of 0.45.

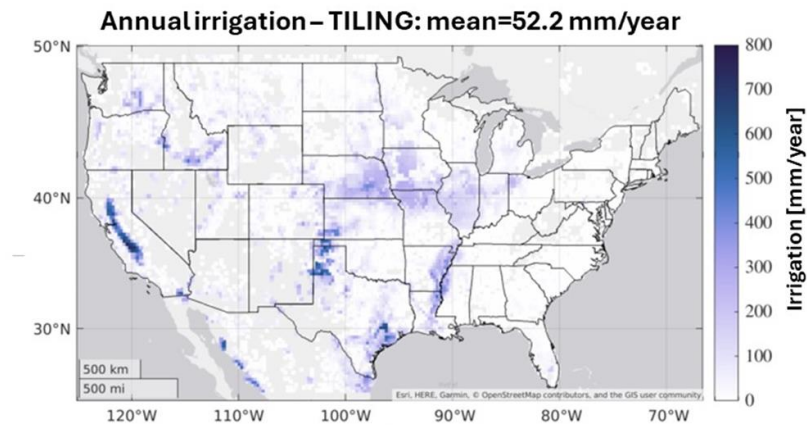


Figure 5.12: Annual irrigation map in mm/year obtained using the TILING option and a Th_{irr} value equal to 0.45. Mean spatial value of irrigation is reported in the title. The map refers to the year 2013.

The irrigation simulations were further validated against FRIS data. Figure 5.12 compares the GVF NO-TILING run (Figures 5.12a and 5.12c for 2013 and 2018, respectively) with the GVF TILING run (Figures 5.12b and 5.12d for 2013 and 2018, respectively), both using a Th_{irr} of 0.45. The two runs reveal significant differences, particularly in the number of states evaluated and those with non-zero values relative to the benchmark data (see the N_p values in each scatterplot title). As anticipated, the TILING option shows a higher overestimation, with Bias values of 3.36 and 2.51 km^3/year for 2013 and 2018, respectively, compared to 2.50 and 1.13 km^3/year for the NO-TILING option. Spatial R values are similar in 2013, though the TILING option shows a decline in 2018, dropping from 0.72 (NO-TILING) to 0.61 (TILING). RMNSD is also higher for the TILING run (3.43 vs. 2.20 in 2013), indicating a relatively larger error for this option. However, the TILING approach may still offer a more realistic outcome by providing comprehensive coverage across all 48 CONUS states.

Figure 5.3.9 provides a visual comparison between FRIS data (Figure 5.13a), the NO-TILING run (Figure 5.13b), and the TILING run (Figure 5.13c) for 2013, showing annual irrigation volumes (km^3/year) with a blue colormap representing irrigation amounts. Both model runs exhibit overestimation, particularly in Texas, Nebraska, Iowa, and Illinois. However, the TILING option improves coverage by including lower-irrigation states, offering broader geographic detail across all states.

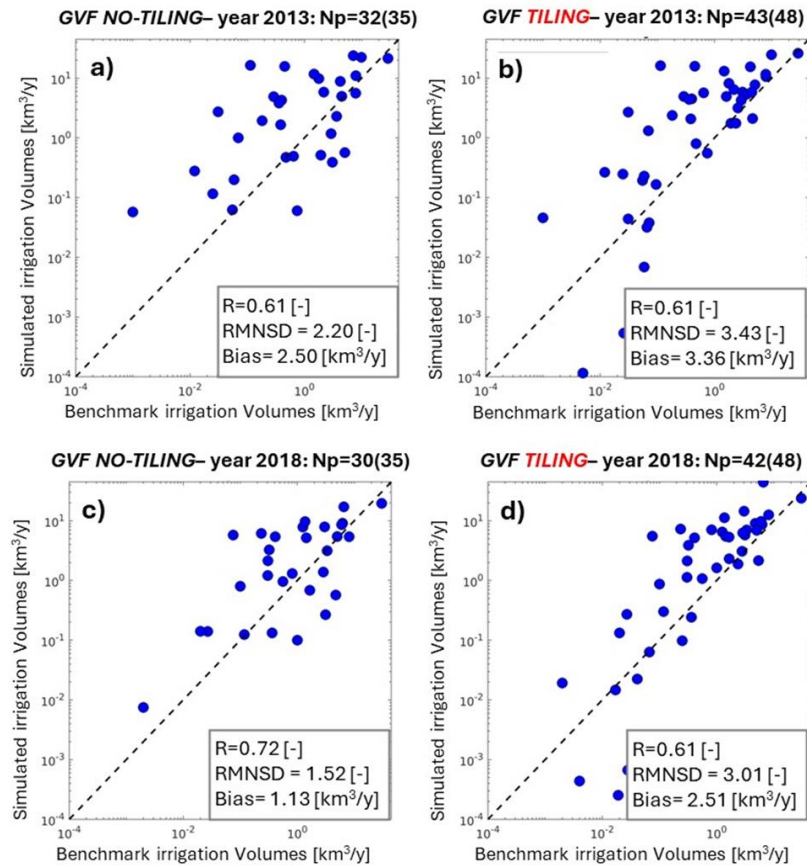


Figure 5.13: Scatterplot comparing benchmark irrigation volumes (km³/year) against simulated volumes at state level (i.e., each point represents one state). Plots a) to b) show the results for the year 2013, for the following runs: a) GVF NO-TILING; and b) GVF TILING. Plots c) to d) show the results for the year 2018, for the following runs: c) GVF NO-TILING; and d) GVF TILING. Np, in the title, indicates the number of states with non-zero irrigation while the number in the parenthesis shows the total number of states used for evaluation. Statistical scores (R, RMNSD, bias) are shown in the boxes included in each plot. The Th_{irr} is kept constant to a value of 0.45. Note that the scatterplots are represented in logarithmic scale in order to enhance visualisation.

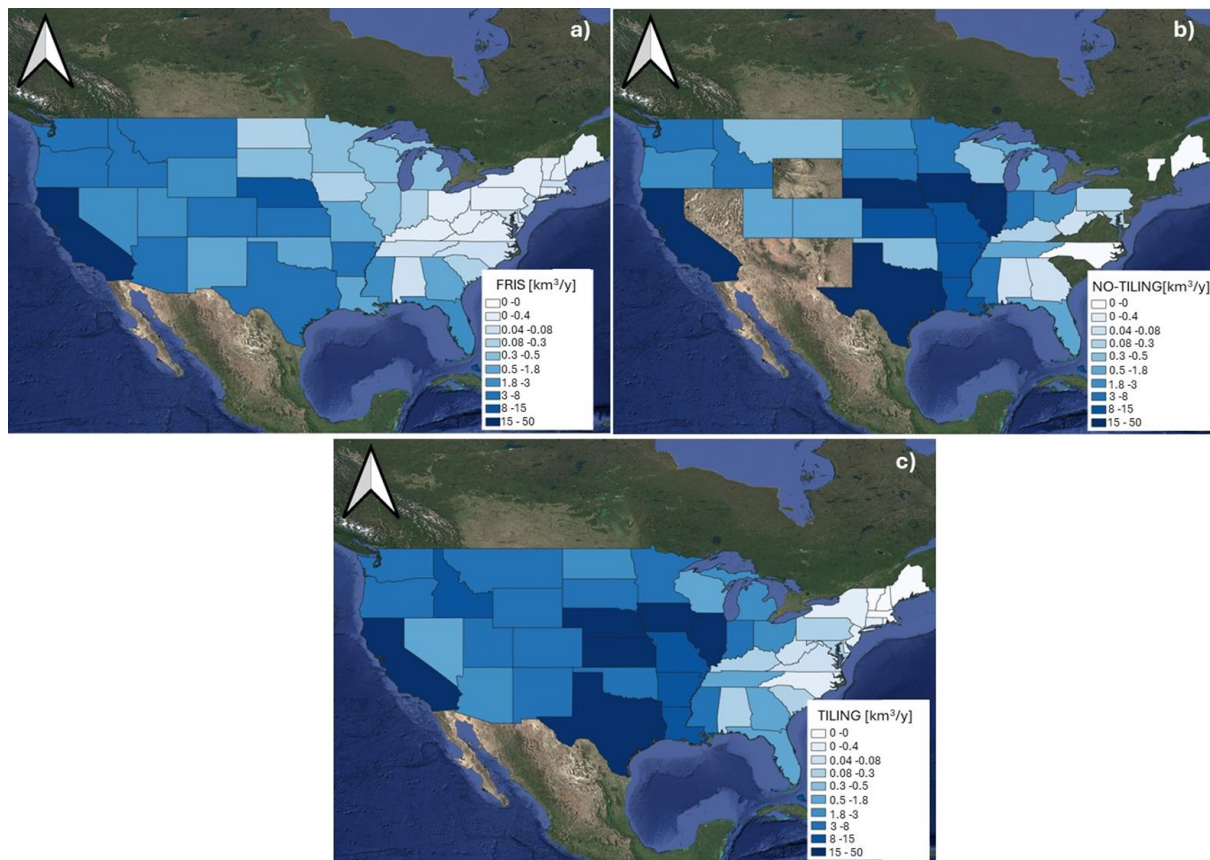


Figure 5.14: Annual irrigation volumes in km³/year for: a) the benchmark FRIS data; b) the GVF NO-TILING simulation run; c) the GVF TILING simulation run. The Th_{irr} is left constant to a value of 0.45 for the simulation runs. The uncolored states in the NO-TILING option represent areas outside the irrigation mask, which have been intentionally left without colour.

Model outputs (GVF TILING and GVF NO-TILING with a Th_{irr} of 0.45) were additionally evaluated in terms of surface soil moisture (SSM). This evaluation used 15-day averaged SSM data derived from both the model and SMAP Level 2 SSM version 8 (details on this product are available in Deliverable 2). Calculations of both the Pearson correlation (R) and the unbiased Root Mean Squared Difference (ubRMSD) were included to account for long-term bias between the satellite data and model outputs. The results are presented in Figure 5.15, comparing the NO-TILING (Figures 5.15a and 5.15b) and TILING (Figures 5.15c and 5.15d) configurations. Although the evaluations involved different numbers of pixels (due to the distinct irrigation masks used in each run), both configurations showed comparable RRR and ubRMSD values for shared pixels. The spatially averaged RRR ranged from 0.72 for the NO-TILING configuration to 0.75 for the TILING configuration, while ubRMSD values ranged from 0.033 to 0.030—both meeting the target accuracy for SMAP data. A time series analysis focused on higher-latitude pixels (e.g., in Minnesota) revealed a notable bias between the model outputs and satellite observations; however, the agreement across most evaluated grids was strong.

Based on these evaluation results, deterministic simulations for both TILING and NO-TILING GVF configurations (Th_{irr} =0.45) will be included in the CRDP, covering the period from January 2010 to March 2023 at a monthly resolution. For example, Figure 5.16 illustrates monthly aggregated irrigation time series for both model configurations over two sample pixels: one in California and one in Arkansas. Interestingly, the NO-TILING simulation consistently shows higher irrigation levels at the pixel scale. This discrepancy arises

because, in the NO-TILING run, each pixel is classified entirely as cropland, while in the TILING configuration, only 60% of the California pixel and 66% of the Arkansas pixel are classified as cropland. At a regional scale (CONUS), however, the TILING simulation estimates greater total irrigation, as it includes 9295 irrigated pixels compared to 2397 in the NO-TILING simulation.

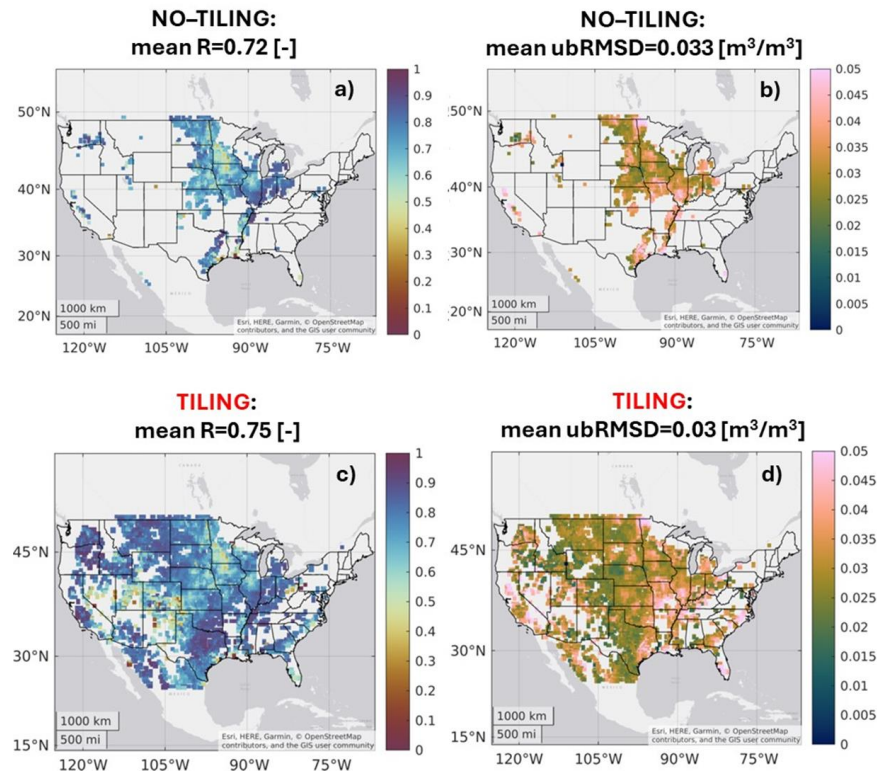


Figure 5.15: Maps of Pearson-R between SMAP Level-2 SSM and: a) the NO-TILING SSM; c) the TILING SSM. Maps of ubRMSD between SMAP Level-2 SSM and: b) the NO-TILING SSM; d) the TILING SSM. The scores are obtained averaging the soil moisture data at bi-weekly time scale.

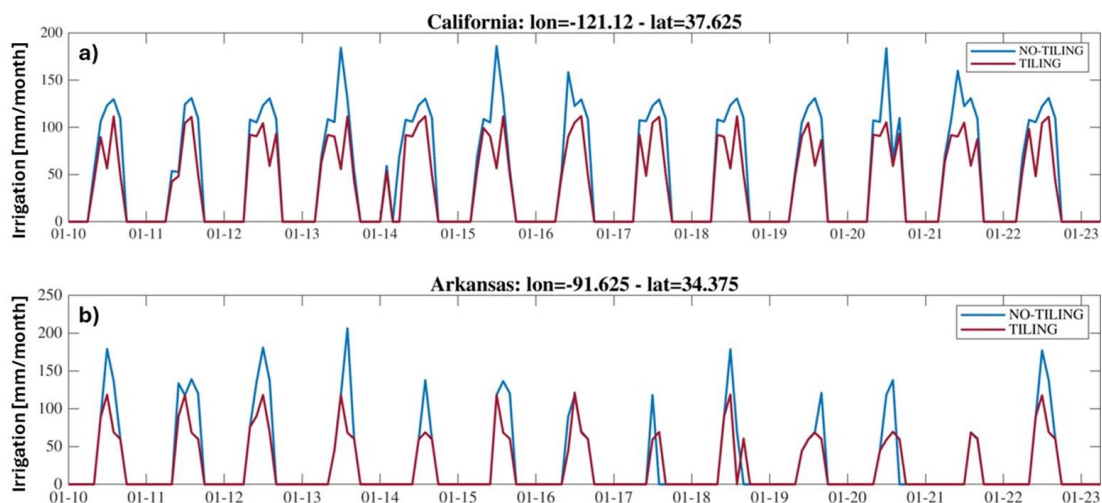


Figure 5.16: Timeseries for an irrigated pixel in: a) California; and b) Arkansas. Data are accumulated at monthly timescale and both the NO-TILING (blue) and TILING (red) runs are shown.

5.3.2. Ensemble runs

Following a similar setup as described in section 5.3.1, the Noah-MPv4.0.1 model was run in ensemble mode with the NO-TILING option. The ensemble of land model trajectories is composed of 24 ensemble members for which selected meteorological input forcings are perturbed. The ensemble runs provide an estimation of the irrigation uncertainty, where the ensemble standard deviation (or ensemble spread [mm/day]) is calculated for each day. Running an ensemble allows to estimate the uncertainty of the irrigation amounts.

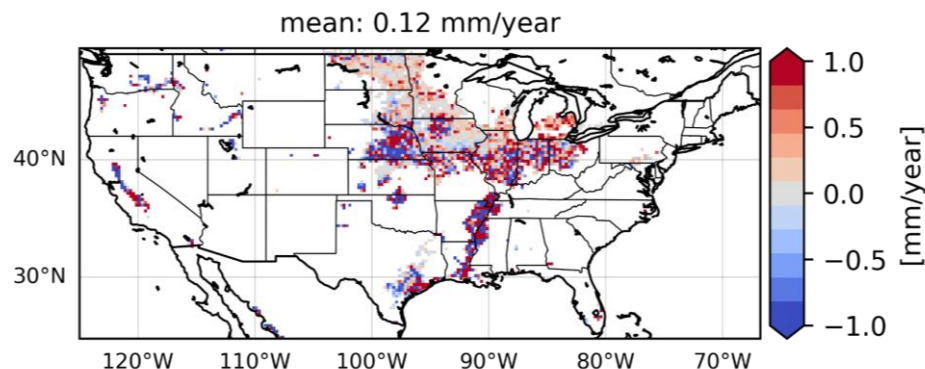


Figure 5.17: Difference between the ensemble mean irrigation and the deterministic irrigation (annual average for the period 2010-2023).

Annual averages of the deterministic irrigation run and the ensemble mean irrigation are similar with on average 0.12 mm/year additional irrigation for the ensemble mean compared to the deterministic irrigation. A map of the difference between the ensemble mean and the deterministic irrigation is shown in Figure 5.17. The absolute largest difference is 13.47 mm/year.

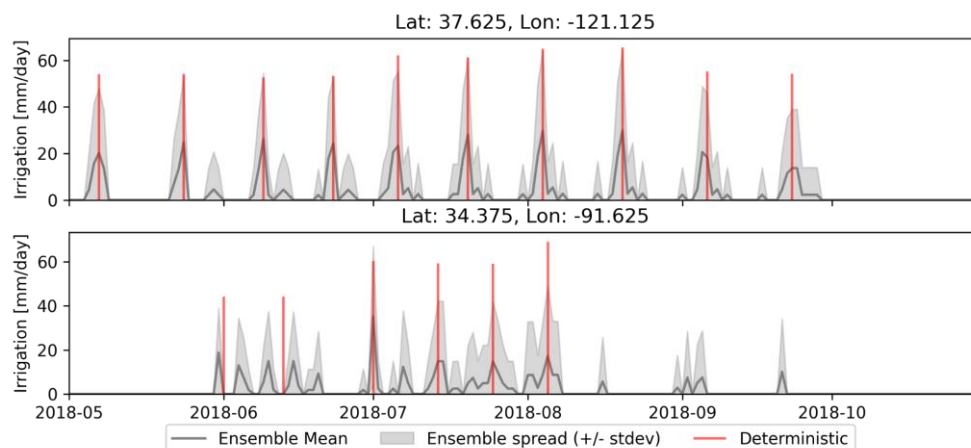


Figure 5.18: Timeseries of deterministic irrigation, ensemble mean irrigation and ensemble spread (ensemble mean \pm 1 stdev) for an irrigated pixel in: a) California; and b) Arkansas.

Figure 5.18 shows two example time series of the ensemble mean irrigation with the ensemble spread, along with the results from the deterministic run from section 5.3.1. The timeseries show more temporarily distributed irrigation amounts when running in ensemble mode, also showing the variation of the ensemble spread through time.

Spatial patterns in the uncertainty can be evaluated via the coefficient of variation (CV [-]) by taking the temporally averaged ensemble spread divided by the average irrigation rate, both computed on the irrigation days only.

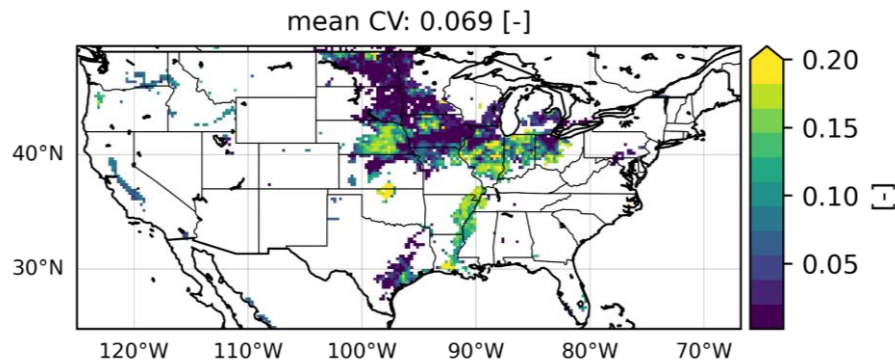


Figure 5.19: Map of the coefficient of variation (CV [-]) shown for irrigated pixels only for 2010 through 2023.

Figure 5.19 shows a higher CV around the Mississippi river and in the center of the study domain. In California, the CV is relatively low because of a lower average ensemble spread and large average annual irrigation amounts.

The uncertainty was computed per region (State) and added to the evaluation of the simulations against the FRIS data for 2013 and 2018. The results are summarized in Table 5.3. The uncertainties are expressed as standard deviations and are large given the non-normal distribution of the irrigation.

Table 5.3. Benchmark and simulated (\pm uncertainty) [km^3/year] for all states where irrigation is simulated. Note that no irrigation was simulated in Maryland and Pennsylvania in 2018.

	2013		2018	
State	Benchmark	Simulated (\pm uncertainty)	Benchmark	Simulated (\pm uncertainty)
ALABAMA	0.06	0.06 (\pm 0.07)	0.12	0.12 (\pm 0.10)
ARKANSAS	7.96	11.02 (\pm 26.89)	6.26	9.08 (\pm 22.92)
CALIFORNIA	28.97	21.48 (\pm 29.52)	30.21	19.51 (\pm 28.05)
COLORADO	5.10	0.57 (\pm 3.30)	4.74	0.57 (\pm 3.31)
FLORIDA	1.94	0.51 (\pm 3.40)	1.67	0.68 (\pm 3.40)
GEORGIA	0.75	0.06 (\pm 1.43)	1.01	0.10 (\pm 2.11)
IDAHO	7.92	5.60 (\pm 14.41)	8.16	5.41 (\pm 13.96)
ILLINOIS	0.45	15.74 (\pm 18.48)	0.41	5.41 (\pm 13.62)
INDIANA	0.29	4.89 (\pm 9.60)	0.31	1.22 (\pm 5.64)
IOWA	0.11	16.43 (\pm 15.05)	0.08	5.75 (\pm 6.91)

KANSAS	4.23	8.86 (\pm 11.93)	3.03	7.93 (\pm 12.42)
KENTUCKY	0.03	0.12 (\pm 1.96)	0.03	0.14 (\pm 2.21)
LOUISIANA	1.79	9.80 (\pm 20.05)	1.26	7.84 (\pm 17.81)
MARYLAND	0.06	0.20 (\pm 0.18)	0.08	0.00 (/)
MICHIGAN	0.38	1.66 (\pm 2.58)	0.56	0.96 (\pm 1.96)
MINNESOTA	0.40	4.31 (\pm 3.38)	0.31	2.14 (\pm 1.59)
MISSISSIPPI	2.18	5.86 (\pm 19.52)	1.44	5.18 (\pm 17.83)
MISSOURI	1.47	11.69 (\pm 14.23)	1.37	9.73 (\pm 14.28)
MONTANA	3.09	0.39 (\pm 3.29)	3.14	0.27 (\pm 2.80)
NEBRASKA	9.95	22.30 (\pm 31.55)	5.99	8.59 (\pm 20.84)
NORTH DAKOTA	0.18	1.95 (\pm 1.87)	0.23	6.12 (\pm 5.43)
OHIO	0.03	2.75 (\pm 5.42)	0.02	0.14 (\pm 0.98)
OKLAHOMA	0.64	0.49 (\pm 3.13)	0.82	1.31 (\pm 6.65)
OREGON	3.66	2.30 (\pm 9.40)	3.35	3.15 (\pm 11.13)
PENNSYLVANIA	0.01	0.28 (\pm 0.36)	0.05	0.00 (/)
SOUTH DAKOTA	0.36	3.82 (\pm 3.52)	0.32	3.25 (\pm 1.96)
TENNESSEE	0.07	1.00 (\pm 7.66)	0.10	0.80 (\pm 6.89)
TEXAS	7.15	23.85 (\pm 19.95)	6.59	17.08 (\pm 16.01)
UTAH	2.93	1.18 (\pm 3.88)	2.87	1.39 (\pm 4.20)
WASHINGTON	4.52	4.97 (\pm 10.70)	5.02	5.47 (\pm 11.25)
WISCONSIN	0.48	0.47 (\pm 0.83)	0.36	0.13 (\pm 0.67)

References

- Allen, R., Pereira, L., Smith, M., 1998. Crop evapotranspiration-Guidelines for computing crop water requirements-FAO Irrigation and drainage paper 56.
- Bretreger, D., Yeo, I.-Y., Hancock, G., and Willgoose, G. (2020). Monitoring irrigation using landsat observations and climate data over regional scales in the Murray-Darling Basin, *J. Hydrol.*, 590, 125356, <https://doi.org/10.1016/j.jhydrol.2020.125356>.
- California Department of Water Resources, 2013. Accessed November 15, 2024. Available at: https://water.ca.gov/-/media/DWR-Website/Web-Pages/Programs/Groundwater-Management/Bulletin-118/Files/Statewide-Reports/GWU2013_Ch12_ColoradoRiver_Final.pdf
- Dangar, S., Asoka, A., and Mishra, V. (2021). Causes and implications of groundwater depletion in India: A review. *J. Hydrol.*, 596, 126103, <https://doi.org/10.1016/j.jhydrol.2021.126103>.
- Dari, J., Brocca, L., Modanesi, S., Massari, C., Tarpanelli, A., Barbetta, S., Quast, R., Vreugdenhil, M., Freeman, V., BarellaOrtiz, A., Quintana-Seguí, P., Bretreger, D., and Volden, E. (2023). Regional data sets of high-resolution (1 and 6 km) irrigation estimates from space. *Earth Syst. Sci. Data*, 15, 1555–1575, <https://doi.org/10.5194/essd-15-1555-2023>.
- Dari, J., Morbidelli, R., Quintana-Seguí, P., and Brocca, L. (2024). The Temporal-Stability-Based Irrigation MAPping (TSIMAP) Method: A Virtuous Trade-Off between Accuracy, Flexibility, and Facility for End-Users. *Water*, 16 (5), 644, <https://doi.org/10.3390/w16050644>.
- Dorigo, W., Dietrich, S., Aires, F., Brocca, L., Carter, S., Cretaux, J. F., ... & Aich, V. (2021). Closing the water cycle from observations across scales: where do we stand? *Bulletin of the American Meteorological Society*, 102(10), E1897-E1935, doi:10.1175/BAMS-D-19-0316.1.
- Fang, L., Zhan, X., Hain, C.R., and Liu, J. (2018). Impact of using near real-time green vegetation fraction in Noah land surface model of NOAA NCEP on numerical weather predictions. *Advances in Meteorology*, <https://doi.org/10.1155/2018/9256396>.
- Hersbach, H., and Coauthors, 2020: The ERA5 global reanalysis. *Quart. J. Roy. Meteor. Soc.*, 146, 1999–2049, <https://doi.org/10.1002/qj.3803>.
- Kelley, J., Olson, B., 2022. Interannual variability of water productivity on the Eastern Snake Plain in Idaho, United States. *Agricultural Water Management* 265, 107532. <https://doi.org/10.1016/j.agwat.2022.107532>
- Kragh, S.J., Fensholt, R., Stisen, S., Koch, J., 2023. The precision of satellite-based net irrigation quantification in the Indus and Ganges basins. *Hydrology and Earth System Sciences* 27, 2463–2478. <https://doi.org/10.5194/hess-27-2463-2023>
- Kumar, S. V., Peters-Lidard, C., Tian, Y., Houser, P., Geiger, J., Olden, S., Lighty, L., Eastman, J., Doty, B., and Dirmeyer, P. (2006): Land information system: An interoperable framework for high resolution land surface

modeling. Environmental Modelling & Software 21, 1402–1415.
<https://doi.org/10.1016/j.envsoft.2005.07.004>.

Massari, C., Modanesi, S., Dari, J., Gruber, A., De Lannoy, G. J. M., Girotto, M., Quintana-Seguí, P., Le Page, M., Jarlan, L., Zribi, M., Ouadi, N., Vreugdenhil, M., Zappa, L., Dorigo, W., Wagner, W., Brombacher, J., Pelgrum, H., Jaquot, P., Freeman, V., Volden, E., Fernandez Prieto, D., Tarpanelli, A., Barbetta, S., and Brocca, L. (2021). A review of irrigation information retrievals from space and their utility for users, *Remote Sens.-Basel*, 13, 4112, <https://doi.org/10.3390/rs13204112>.

Mehta, P., Siebert, S., Kumm, M., Deng, Q., Ali, T., Marston, L., Xie, W., and Davis, K. (2022). Global Area Equipped for Irrigation Dataset 1900–2015 v3.0, Zenodo [data set], <https://doi.org/10.5281/zenodo.6886564>.

Mehta, P., Siebert, S., Kumm, M., Deng, Q., Ali, T., Marston, L., Xie, W., and Davis, K. (2024). Half of twenty-first century global irrigation expansion has been in water-stressed regions. *Nature Water*, 2, 254–261, <https://doi.org/10.1038/s44221-024-00206-9>.

McDermid, S., Nocco, M., Lawston-Parker, P., ..., Brocca, L., ..., 40 authors (2023). Irrigation in the Earth system. *Nature Reviews Earth & Environment*, 4, 435–453, doi:10.1038/s43017-023-00438-5.

Modanesi, S., Massari, C., Bechtold, M., Lievens, H., Tarpanelli, A., Brocca, L., Zappa, L., De Lannoy, G.J.M (2022). Challenges and benefits of quantifying irrigation through the assimilation of Sentinel-1 backscatter observations into Noah-MP. *Hydrol. Earth Syst. Sci.*, 26, 4685–4706. <https://doi.org/10.5194/hess-26-4685-2022>.

Niu, G. Y., Yang, Z. L., Mitchell, K. E., Chen, F., Ek, M. B., Barlage, M., Kumar, A., Manning, K., Niyogi, D., Rosero, E., Tewari, M., and Xia, Y. (2011). The community Noah land surface model with multiparameterization options (Noah-MP): 1. Model description and evaluation with local-scale measurements, *J. Geophys. Res.-Atmos.*, 116, 1–19, <https://doi.org/10.1029/2010JD015139>.

Ozdogan, M., Rodell, M., Beaudoin, H. K., and Toll, D. L. (2010). Simulating the effects of irrigation over the United States in a land surface model based on satellite derived agricultural data, *J. Hydrometeorol.*, 11, 171–184, <https://doi.org/10.1175/2009JHM1116.1>.

Portmann, F., Siebert, S., Bauer, C., and Döll, P. (2008). Global data set of monthly growing areas of 26 irrigated crops, Version 1.0, Frankfurt Hydrol. Pap. 06, Inst. of Phys. Geogr., Univ. of Frankfurt, Frankfurt, Germany, 179–180 pp.

Quast, R., Wagner, W., Bauer-Marschallinger, B., and Vreugdenhil, M. (2023). Soil moisture retrieval from Sentinel-1 using a first-order radiative transfer model - a case-study over the Po-Valley. *Remote Sensing of Environment*, 295, 113651, <https://doi.org/10.1016/j.rse.2023.113651>.

Rodell, M., Beaudoin, H.K., L'Ecuyer, T.S., Olson, W.S., Famiglietti, J.S., Houser, P.R., Adler, R., Bosilovich, M.G., Clayson, C.A., Chambers, D., Clark, E., Fetzer, E.J., Gao, X., Gu, G., Hilburn, K., Huffman, G.J., Lettenmaier, D.P., Liu, W.T., Robertson, F.R., Schlosser, C.A., Sheffield, J., Wood, E.F., (2015). The Observed State of the Water Cycle in the Early Twenty-First Century. *J. Clim.* 28, 8289–8318.

Siebert, S., Kummu, M., Porkka, M., Döll, P., Ramankutty, N., Scanlon, B.R., 2015. A global data set of the extent of irrigated land from 1900 to 2005. *Hydrology and Earth System Sciences* 19, 1521–1545. <https://doi.org/10.5194/hess-19-1521-2015>

Teluguntla, P., Thenkabail, P., Oliphant, A., Gumma, M., Anece, I., Foley, D. and McCormick, R. (2023). Landsat-derived Global Rainfed and Irrigated-Cropland Product @ 30-m (LGRIP30) of the World (GFSADLGRIP30WORLD). The Land Processes Distributed Active Archive Center (LP DAAC) of NASA and USGS. Pp. 103. IP-148728. DOI: <https://doi.org/10.5067/Community/LGRIP/LGRIP30.001>

Zaussinger, F., Dorigo, W., Gruber, A., Tarpanelli, A., Filippucci, P., and Brocca, L. (2019). Estimating irrigation water use over the contiguous United States by combining satellite and reanalysis soil moisture data, *Hydrol. Earth Syst. Sci.*, 23, 897–923, <https://doi.org/10.5194/hess-23-897-2019>.